ADVANCED MASTERS IN STRUCTURAL ANALYSIS
OF MONUMENTS AND HISTORICAL CONSTRUCTIONS

Master's Thesis

Myronas Drygiannakis

Investigation on the strength of spandrels in masonry façades

UNIVERSITAT POLITÈCNICA DE CATALUNYA

Education and Culture

Erasmus Mundus

Spain | 2017

DECLARATION

Name: Myronas Drygiannakis

Email: myronasdr@gmail.com

Title of the Msc Dissertation: Investigation on the strength of spandrels in masonry façades

Supervisor(s): Pere Roca Fabregat & Jorge Segura Domingo

Year: 2017

I hereby declare that all information in this document has been obtained and presented in accordance with academic rules and ethical conduct. I also declare that, as required by these rules and conduct, I have fully cited and referenced all material and results that are not original to this work.

I hereby declare that the MSc Consortium responsible for the Advanced Masters in Structural Analysis of Monuments and Historical Constructions is allowed to store and make available electronically the present MSc Dissertation.

University: Universidad Politécnica de Cataluña

Date: 14/07/2017

Signature:

_____

This page is left blank on purpose.

To my family

This page is left blank on purpose.

ACKNOWLEDGEMENTS

My sincere gratitude to Professor Pere Roca for his excellent assistance. His inspiring guidance and enthusiasm to discuss every single idea were essential in each step of this work.

I would like to thank Jorge Segura, for his shared knowledge, his patience and his willingness to help me at any moment for every small or serious issue that appeared during the thesis period.

I would also like to thank all my SAHC professors from the universities of Barcelona, Padova, Minho and Prague for all the knowledge they shared with me.

I want to express my gratitude to all my classmates and friends from the SAHC Master. Their support and assistance during every task I encountered as well as the solidarity between us, made this challenging and difficult period of my life, much easier and pleasant.

My sincere thanks to the SAHC Consortium for granting me with a scholarship, which made my involvement to this Master program possible.

I would like to express my highest gratitude to my Professor from the Aristotle University of Thessaloniki, Ioanna Papayianni for introducing me to the topic of restoration of historical constructions, informing me about the SAHC Master and helping me to be accepted as SAHC student.

Finally I want to express my gratitude to my family for everything they have done for me since now and everything they continue to do every day.

This page is left blank on purpose.

ABSTRACT

The study of the lateral strength of masonry façades and general walls with openings is of utmost importance for the verification of the seismic capacity of masonry buildings. Significant research effort has been recently devoted to the characterization of the seismic performance of this type of structures by means of both experimental and numerical techniques. A critical aspect which, to large extent, determines the lateral capacity of masonry façades and walls with openings is found in the shear capacity of the structural members involved and, in specific, that of the spandrel walls situated over or below openings and between the masonry piers.

The shear capacity of masonry spandrels has been analyzed according to different approaches. Different researchers have proposed analytical equations and simple failure criteria for the estimation of their shear capacity. The seismic performance of spandrels has been analyzed also by means of numerical methods encompassing different levels of complexity, such as micro-models, macro-models and the equivalent frame method.

This thesis contains a detailed investigation of the state of the art regarding the seismic performance of masonry façades concentrated in the in plane behavior of spandrels. This investigation is including the observations from past earthquakes and experimental cases, as well as numerical and simplified analytical approaches which aim to characterize the behavior of the spandrel component subjected to lateral loads.

Based on the conclusions from the state of the art review, an appropriate numerical model is developed based on the Finite Element macromodelling approach. The adopted model is calibrated using a previous experimental campaign as a benchmark problem. A detailed parametric study is executed in order to investigate the influence of several parameters such as the masonry mechanical properties and the interaction between timber lintel and masonry. Once the model is calibrated it is applied to a new test to estimate its expected behavior.

In addition, a simplified micromodel is adopted in the process of obtaining a more explicit solution. A limited parametric analysis is revealing the influence of properties that are difficult to be defined experimentally such as the interface parameters between unit and mortar.

The results from the numerical approaches are revealing the possibilities and drawbacks of the Finite Element method to the simulation and assessment of unreinforced masonry façades subjected to in plane lateral loads. Finally the conclusions derived from the results of this thesis are discussed and ideas for further work are proposed.

This page is left blank on purpose.

RESUMEN

INVESTIGACIÓN SOBRE LA CAPACIDAD ESTRUCTURAL DE LOS DINTELES EN FACHADAS DE OBRA DE FÁBRICA

El estudio de la resistencia lateral de fachadas de obra de fábrica y, en general, de muros con aperturas, es de vital importancia para la verificación de estructuras de mampostería frente a acciones sísmicas. Se han efectuado esfuerzos significativos en la investigación acerca de la caracterización del comportamiento sísmico de este tipo de estructuras, tanto con técnicas experimentales como numéricas. Un aspecto crucial que, en gran medida, determina la capacidad lateral de las fachadas de mampostería y muros con aperturas, se ha encontrado en la capacidad de los elementos estructurales para resistir el cortante y, en particular, en la capacidad que ofrecen los dinteles, que son los elementos horizontales de fábrica situados sobre o bajo las aperturas y entre los pilares.

Esta capacidad a cortante de los dinteles ha sido analizada desde distintos puntos de vista. Diferentes investigadores han propuesto ecuaciones analíticas y criterios simples de fallo para la estimación de esta resistencia. El comportamiento sísmico de los dinteles ha sido también estudiado con métodos numéricos incorporando diferentes niveles de complejidad, tales como micromodelos, macromodelos y el método del pórtico equivalente.

Esta tesina presenta una detallada investigación del estado del conocimiento sobre el comportamiento sísmico de fachadas de mampostería, con especial interés en la respuesta de los dinteles en su propio plano. La investigación incluye observaciones de pasados terremotos y casos experimentales, así como estrategias numéricas y simplificadas para la caracterización de la respuesta de los dinteles cuando están sometidos a cargas laterales.

Basado en las conclusiones del estado del arte, se ha desarrollado un modelo numérico siguiendo la estrategia de macromodelización por elementos finitos. El modelo adoptado se ha calibrado utilizando una campaña experimental previa como problema de referencia. Al mismo tiempo, un detallado estudio paramétrico se ha efectuado para investigar la influencia de diversos parámetros como son las propiedades mecánicas de la obra de fábrica y la interacción entre esta y la viga dintel de madera. Una vez que el modelo ha sido calibrado, se ha aplicado a un nuevo experimento para estimar su respuesta.

This page is left blank on purpose.

RESUM

RECERCA SOBRE LA CAPACITAT ESTRUCTURAL DE LES LLINDES EN FAÇANES D'OBRA DE FÀBRICA

L'estudi de la resistència lateral de façanes d'obra de fàbrica i, en general, de murs amb apertures, és de vital importància per la verificació d'estructures de maçoneria front a accions sísmiques. S'han efectuat significatius esforços de recerca al voltant de la caracterització del comportament sísmic d'aquest tipus d'estructures, tant amb tècniques experimentals com numèriques. Un aspecte crucial que, en gran mesura, determina la capacitat lateral de les façanes de maçoneria i murs amb apertures, s'ha trobat en la capacitat dels elements estructurals per resistir la cisalla i, en particular, la capacitat que ofereixen les llindes, que són aquí els elements horitzontals d'obra de fàbrica situats sobre o sota les apertures i entre els pilars.

Aquesta capacitat a cisalla de les llindes ha estat analitzada des de distints punts de vista. Diferents investigadors han proposat equacions analítiques i criteris simples de trencament per a l'estimació d'aquesta resistència. El comportament sísmic de les llindes ha estat també estudiat amb mètodes numèrics incorporant diferents nivells de complexitat, tals com micromodels, macromodels i el mètode del pòrtic equivalent.

Aquesta tesina presenta una detallada investigació de l'estat del coneixement sobre el comportament sísmic de façanes de maçoneria, amb especial interès en el comportament de les llindes en el seu pla. La recerca inclou observacions de passats terratrèmols i casos experimentals, així com estratègies numèriques i simplificades per a la caracterització de la resposta de les llindes quan es sotmeten a càrregues laterals.

Basat en les conclusions de l'estat del coneixement, s'ha desenvolupat un model numèric seguint l'estratègia de macromodelatge per elements finits. El model adoptat s'ha calibrat emprant un campanya experimental prèvia com a problema de referència. Al mateix temps, un detallat estudi paramètric s'ha efectuat per investigar la influència de diversos paràmetres com ara les propietats mecàniques de la maçoneria i la interacció entre aquesta i la biga llinda de fusta. Un cop el model ha estat calibrat, s'ha aplicat a un nou experiment per estimar la seva resposta.

A més, un micromodel simplificat s'ha adoptat amb la intenció d'obtenir una solució més explícita. Una anàlisi paramètrica reduïda ha posat en relleu la importància que tenen algunes propietats, les quals són molt difícils de definir experimentalment, tals com els paràmetres de la interfície entre els blocs i el morter.

Els resultats d'aquestes estratègies numèriques revelen les possibilitats i punts febles del mètode dels elements finits per simular i avaluar el comportament d'estructures d'obra de fàbrica no reforçada sotmeses a càrregues laterals en el seu pla. Finalment, s'inclou una discussió dels resultats de la tesina i idees per a futures línies de recerca.

This page is left blank on purpose.

ΠΕΡΙΛΗΨΗ

Διερεύνιση της αντοχής των διαδοκίδων-ανωφλιών σε προσόψεις κτιρίων από άοπλη τοιχοποιία

Η μελέτη της οριζόντιας διατμητικής αντοχής των προσόψεων άοπλης τοιχοποιίας και γενικά των τοίχων με ανοίγματα θεωρείται ζήτημα υψίστης σημασίας για την αποτίμηση της σεισμικής φέρουσας ικανότητας των κτιρίων από φέρουσα τοιχοποιία. Την τελευταία περίοδο σημαντική ερευνητική δραστηριότητα έχει αφιερωθεί στον χαρακτηρισμό της σεισμικής συμπεριφοράς αυτού του τύπου των κατασκευών τόσο με πειραματικές, όσο και με αριθμητικές μεθόδους. Ένας καθοριστικός παράγοντας για την φέρουσα ικανότητα προσόψεων φέρουσας τοιχοποιίας και τοίχων με ανοίγματα σε οριζόντια φορτία, είναι η διατμητική αντοχή των δομικών στοιχείων που λαμβάνουν μέρος και , πιο ειδικά, αυτή των διαδικίδων-ανωφλιών, τα οποία βρίσκονται πάνω ή εκατέρωθεν ανοιγμάτων ή μεταξύ των πεσσών.

Η διατμητική αντοχή των διαδοκίδων-ανωφλιών από τοιχοποιία έχει μελετηθεί με βάση μια σειρά από διαφορετικές προσεγγίσεις. Διάφοροι ερευνητές έχουν προτείνει μια σειρά από αναλυτικές εξισώσεις και απλοποιημένα κριτήρια αστοχίας για την εκτίμηση της διατμητικής αντοχής τους. Η σεισμική συμπεριφορά των διαδοκίδων-ανωφλιών έχει αναλυθεί επίσης με μια σειρά από αριθμητικές μεθόδους που εμπεριέχουν διαφορετικό βαθμό περιπλοκότητας, όπως μικρομοντελοποίηση, μακρομοντελοποίηση και μοντέλα βασισμένα στην μέθοδο των ισοδύναμων πλαισίων.

Η παρούσα διπλωματική εργασία εμπεριέχει μια λεπτομερή βιβλιογραφική ανασκόπηση, αναφορικά με την σεισμική συμπεριφορά των κτιρίων από άοπλη τοιχοποιία, επικεντρωμένη στην εντός επιπέδου συμπεριφορά των διαδοκίδων-ανωφλιών. Η έρευνα αυτή περιλαμβάνει τις παρατηρήσεις από προηγούμενους σεισμούς, και πειραματικούς ελέγχους, καθώς αριθμητικές και αναλυτικές προσεγγίσεις, που στοχεύουν στον χαρακτηρισμό της συμπεριφοράς των διαδοκίδων-ανωφλιών σε οριζόντια φόρτιση.

Με βάση τα συμπεράσματα της βιβλιογραφικής ανασκόπησης, αναπτύσσεται ένα αριθμητικό μοντέλο βασιμένο στην μέθοδο μακρομοντελοποίησης Πεπερασμένων Στοιχείων. Το επιλεγόμενο μοντέλο αναπτύσσεται και η αξιοπιστία του επικυρώνεται χρησιμοποιώντας μια προηγούμενη πειραματική έρευνα σαν σημείο αναφοράς. Μια εκτενής και λεπτομερής παραμετρική έρευνα εκτελείται με στόχο την αποσαφίνηση της επιρροής διαφορετικών παραμέτρων, όπως οι μηχανικές ιδιότητες της τοιχοποιίας και η αλλιλεπίδραση μεταξύ του ξύλινου ανωφλιού και της τοιχοποιίας. Στην συνέχεια το αναπτυσσόμενο μοντέλο εφαρμόζεται σε ένα νέο πείραμα με στόχο να αποδώσει μια εκτίμηση της αναμενόμενης συμπεριφοράς.

Επιπρόσθέτως ένα απλομοιημένο μικρομοντέλο αναπτύσσεται, στην προσπάθεια να αποδοθει μια πιο ακριβής λύση. Μια περιορισμένη παραμετρική μελέτη αναδεικνύει την επιρροή παραμέτρων που είναι δύσκολο να οριστούν πειραματικά όπως οι ιδιότητες της διεπιφάνεις μεταξύ δομικού λίθου και κονιάματος αρμού.

Τα αποτελέσματα από τις αριθμητικές προσεγγίσεις αναδεικνύουν τις δυνατότητες και τα μειονεκτήματα της μεθόδου των Πεπερασμένων Στοιχείων να προσομοιάσει και να εκτιμήσει την συμπεριφορά προσόψεων άοπλης τοιχοποιίας σε οριζόντια φόρτιση. Τέλος ακολουθεί η παρουσίαση των συμπερασμάτων που πηγάζουν από τα αποτελέσματα της παρούσας διπλωματικής εργασίας καθώς και μια σειρά από προτάσεις για περαιτέρω έρευνα αναφορικά με το υπό μελέτη αντικείμενο.

TABLE OF CONTENTS

TABLE OF FIGURES

TABLE OF TABLES

This page is left blank on purpose.

1. INTRODUCTION

1.1 Motivation

Earthquake is probably the most dangerous natural phenomenon that can threat the integrity of Unreinforced Masonry structures, putting in danger human lives and economical value. During the observation of past earthquakes the out of plane collapse mechanisms have been identified as the most dangerous. The observation and categorization of those mechanisms (D'Ayala and Paganoni 2010) have been proved valuable for the implementation of interventions that aim to the improvement of the connection between orthogonal walls and floor diaphragms, which will result to a desired box behavior of the masonry structure. Once the out of plane mechanisms have been prevented the in plane behavior of the masonry facades is the critical factor that defines the overall capacity of the masonry structure.

Although the in plane behavior of piers in masonry facades has been studied and identified by several experimental, numerical and analytical campaigns (Calderini et al. 2009), limited knowledge exists about the strength of masonry spandrels. The evaluation of their strength is based so far on available formulations derived for pier panels and provided by existing codes like Eurocode 8 (CEN) 1998). Those codes allow the spandrel panels to be included in the evaluation of the masonry capacity only in the presence of tie-rods, or reinforced concrete ring floor beams, at the top and lintels well-bonded to the adjoining piers at the bottom. Other codes like FEMA 356 ((ATC-43 Project) 1998) and New Zealand guidelines (NZSEE 2006) allow the calculation of the spandrel strength based on the strong spandrel-weak pier assumption. This case is not suitable for existing masonry buildings, due to the presence of just wooden or steel lintels without adequate anchorage length to support gravity loads. The assumption of weak spandrel-strong pier is also unsuitable, since it leads to full uncoupling between piers and spandrel.

The last years several experimental campaigns have been executed in order to investigate the strength of masonry spandrels and its contribution to the behavior and capacity of masonry facades (Gattesco et al. 2008), (Beyer and Dazio 2012), (Augenti et al. 2011), (Graziotti et al. 2011), (Graziotti et al. 2014), (Knox 2012), (Allen et al. 2016). In addition several numerical approaches have been implemented to these cases (Parisi et al. 2011), (Beyer and Mangalathu 2014), as well as known and new analytical expressions to validate their accuracy. These studies revealed that the strength of masonry spandrels cannot be neglected and has an important role in the in plane resistance of unreinforced masonry façades.

1.2 Objectives

The work to be accomplished with this thesis aims to assess the strength of spandrels in masonry façades against horizontal loads, by means of different numerical methods adequately calibrated

using experimental reference results. More specifically the main objectives of this thesis were the following:

- To carry out a detailed research in the state of the art on the response of masonry spandrels in façades, experimental previous research, applicable numerical and simplified analytical methods.
- To select and validate adequate numerical methods for the analysis of masonry façades including a micro and a macromodel for masonry structures
- To carry out parametric studies in order to understand the influence of several material properties as well as the presence of the timber lintel and its connection with the masonry component.
- To analyze a new case of an experimental façade to be tested in the laboratory and estimate its strength and nonlinear behavior.
- To draw conclusions on the performance of masonry façades and lintels and on the applicability of numerical methods to simulate their strength response.

1.3 Outline

In order to fulfill the objectives of this thesis, the work is organized into the following five chapters:

Chapter 1: Introduction:

Introduces the motivation, the objectives and the outline of this thesis.

Chapter 2: State of the art:

Presents previous experimental, numerical and analytical studies that attempted to investigate the behavior of masonry spandrels.

Chapter 3: Macromodelling approach:

Presents the development of a FEM macromodel, using a previous experimental case as benchmark problem.

Chapter 4: Micromodelling approach:

Presents the development of a FEM micromodel, using the same experimental case as in Chapter 3.

Chapter 5: Application of the macromodel to a new test:

Provides the application of the developed macromodel to a different case.

Chapter 6: Conclusions:

Includes the conclusions of the thesis as well as recommendations for further work.

2. STATE OF THE ART

2.1 Introduction

The first stage of this dissertation includes a detailed investigation and presentation of the previous knowledge regarding the seismic assessment of masonry façades. The following chapter includes a brief description of the behavior of unreinforced masonry buildings to seismic actions, as well as the main failure mechanisms that have been observed during past earthquakes. Subsequently this state of the art review is concentrated on the existing knowledge regarding the behavior of masonry spandrels to in-plane lateral loads. The main experimental campaigns that have investigated this topic are presented and their results are analyzed and categorized, in order to clarify the influence of several factors to the behavior of masonry spandrels. Finally a description of numerical, simplified and analytical approaches for the structural analysis of spandrels in masonry façades is performed and a comparison between them is executed.

2.2 Masonry facades

In most unreinforced masonry buildings, façades constitute the main vertical structural member. Therefore their behavior during seismic action is critical for the overall performance of the whole structure. In order to evaluate the seismic capacity of unreinforced masonry buildings the strength of façades is an important factor. A brief description of masonry façades as well as their seismic behavior is following.

2.2.1 Type of elements

Masonry facades can be divided in two different categories of structural elements, piers and spandrels. Piers are the vertical structural elements that are responsible for the bearing of the vertical loads of a structure. Spandrel is the portion of the masonry that exists between the openings of two adjacent floors and couples two adjacent piers together. In existing structures there are several types of spandrels. Their categorization is made by the different geometry (Figure 1), types of lintels in the lower part of the spandrel, as well as the type of the floor slab between two adjacent floors and its relative position with the spandrel.

As regards the lintel type, this can be a linear element made of bricks, stones, wood or concrete, or consist of masonry or stone arch (Figure 2)

Figure 1. Different type of masonry spandrels

Figure 2. Different types of lintel

2.2.2 Seismic behavior

The behavior of masonry façades due to seismic action can be divided in two main categories according to the direction of the seismic action: out of plane and in plane failure modes.

2.2.2.1 Out of plane failure modes

Out of plane collapse mechanisms take place in masonry buildings, where there is not adequate connection between orthogonal walls. Also the presence of non-rigid floor diaphragms, increase the probability of such failure modes. Typical collapse mechanisms have been identified by researchers, from observation of damages in masonry buildings during strong earthquakes (L' Aquila 2009). Some of the most characteristic collapse mechanisms are illustrated in Figure 3, Figure 4 and Figure 5.

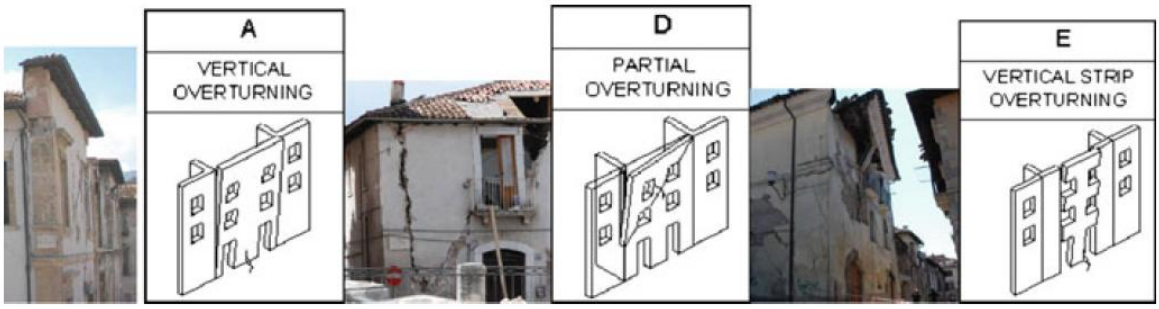

Figure 3. Out-of-plane mechanisms due to poor connections at corners: damage mechanism A, complete overturning of façade: damage mechanism D, partial overturning along a diagonal, mechanism E, partial overturning of the openings vertical strips. (D'Ayala and Paganoni 2010)

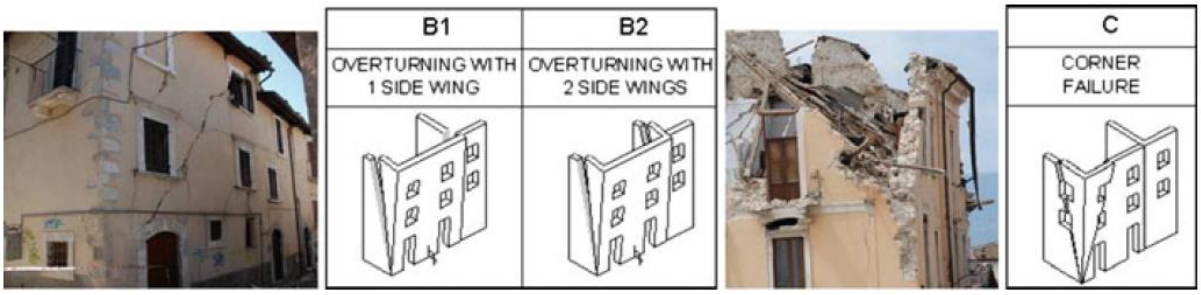

Figure 4. Effects of good connections at corners: damage mechanism B, overturning with side wing/s (left), and damage mechanism C, corner failure (right). (D'Ayala and Paganoni 2010)

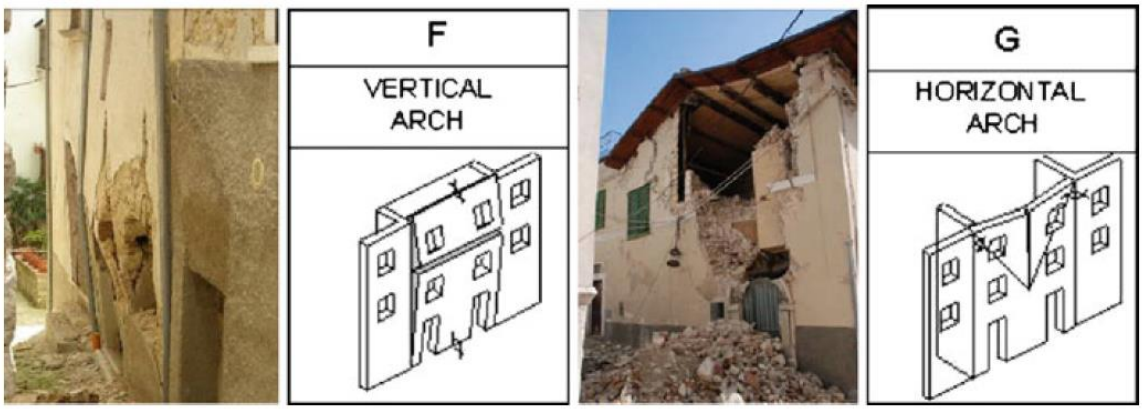

Figure 5. Damage mechanism F-vertical arch (left) and damage mechanism G-horizontal arch (right). (D'Ayala and Paganoni 2010)

2.2.2.2 In plane failure modes

In case of strong connection between orthogonal walls and stiff rigid floor diaphragm, the out of plane failure is prevented and the damage is concentrated in the shear walls parallel to the direction of the seismic action. The damage is often observed to be concentrated in the piers, the spandrels or both types of elements.

(Tomaževič 1999), indicates that in the plane of the walls, bending and shear cause horizontal and diagonal cracks, respectively. In-plane mechanisms induce the typical shear damage, which often is not sufficient to lead to structure collapse. The limited damage in Figure 6 is due to the effective strong connection among the structural components and the presence of floors able to transmit the horizontal forces to shear walls, both characterizing the favorable “box” behavior of buildings under seismic actions. Unfortunately the layout of historic buildings, their discontinuities, the changing in time, lack of maintenance etc., led frequently to different behavior (NIKER Project 2010).

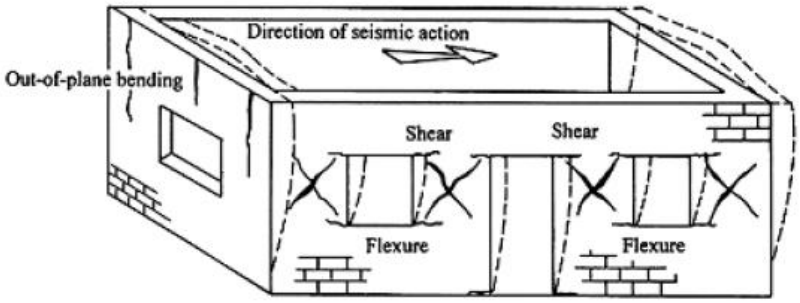

Figure 6. Deformation of the building and typical damage to structural walls. (Tomaževič 1999)

Piers

Observation of seismic damage to complex masonry walls, as well as laboratory experimental tests, showed that masonry piers subjected to in-plane loading may have two typical types of behaviour, with local cracks according to Figure 7(b), with which different failure modes are associated (Calderini et al. 2009):

• Flexural behavior-This may involve two different modes of failure. If the applied vertical load is low with respect to compressive strength, the horizontal load produces tensile flexural cracking at the corners (Figure 7(b)—A branch), and the pier begins to behave as a nearly rigid body rotating about the toe (rocking). If no significant flexural cracking occurs, due to a high applied vertical load, the pier is progressively characterized by a widespread damage pattern, with sub-vertical cracks oriented towards the more compressed corners (crushing). In both cases, the ultimate limit state is obtained by failure at the compressed corners (Figure 7(b)—C branch).

• Shear behavior-This may produce two different modes of failure. In sliding shear failure, the development of flexural cracking at the tense corners reduces the resisting section; failure is attained with sliding on a horizontal bed joint plane, usually located at one of the extremities of the pier. In diagonal cracking, failure is attained with the formation of a diagonal crack, which usually develops at the center of the pier and then propagates towards the corners. The crack may pass prevailingly through mortar joints (assuming the shape of a 'stair-stepped' path in the case of a regular masonry pattern, Figure 7(b)—B1 branch) or also through the blocks (Figure 7(b)—B2 branch).

Figure 8 shows three typical damage patterns associated with the above-described main failure modes.

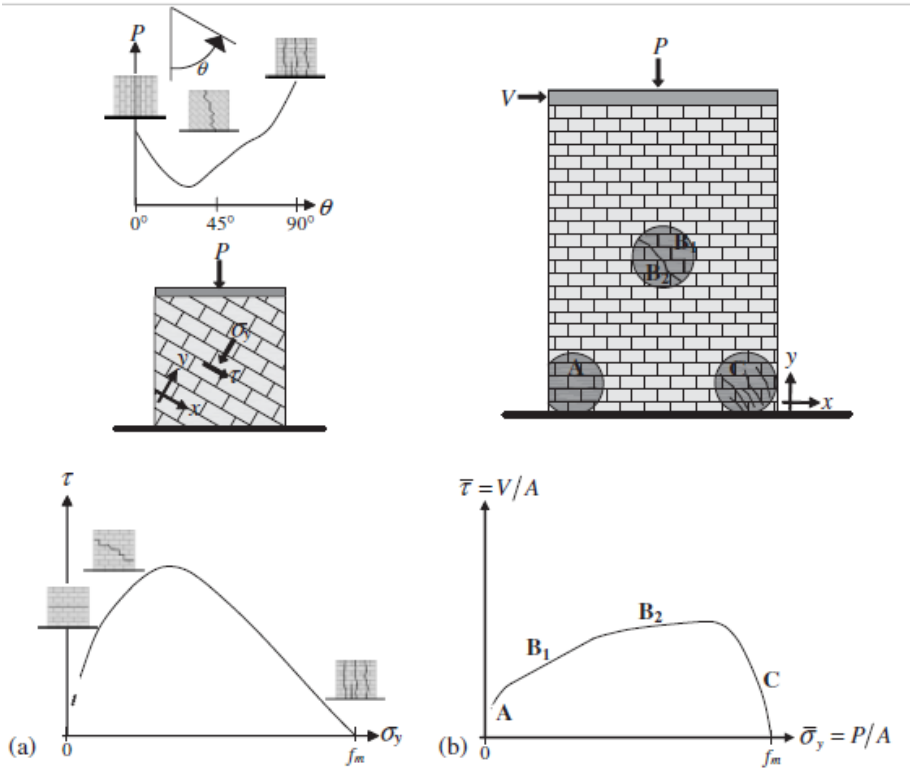

Figure 7. Failure modes and limit domains of masonry: (a) scale of the material and (b) scale of the pier. (Calderini et al. 2009)

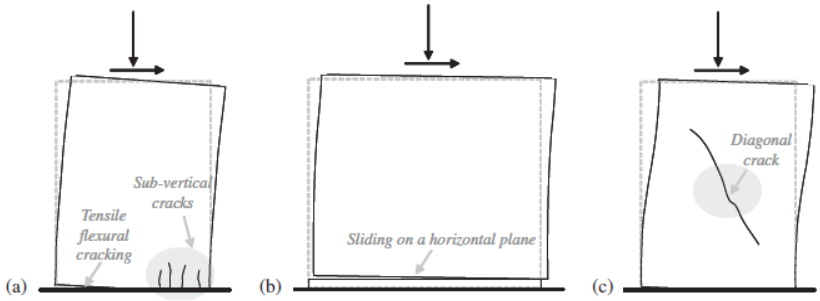

Figure 8. Typical failure modes of masonry piers: (a) rocking: (b) sliding shear failure: and (c) diagonal cracking. (Calderini et al. 2009)

The occurrence of different failure modes depends on several parameters: the geometry of the pier; the boundary conditions; the acting axial load; the mechanical characteristics of the masonry constituents (mortar, blocks, interfaces and relative magnitude between them); the masonry geometrical characteristics (block aspect ratio, in-plane and cross-section masonry pattern) (Calderini et al. 2009).

Spandrels

Although there is less research about the behavior of masonry spandrels comparing the one for piers, their main failure modes have be identified by both experimental studies and observation from past earthquakes. Like in the case of piers, the main failure modes in spandrels are generally characterized as shear and flexural.

A typical failure mode is illustrated in Figure 9. The masonry spandrels have failed in shear and a characteristic diagonal X crack pattern can be observed. This type of failure is occurred due to the relatively wide piers that provide a heavy restraint to the spandrels.

Figure 9. Shear failure of spandrels with shallow masonry arches in an old URM building after the L' Aquila earthquake on 6 April of 2009. (a) Entire building and (b) detail of a spandrel. (Beyer and Dazio 2012)

Another type of failure, observed in a building in the same earthquake, is illustrated in Figure 10, located also in the city center of L' Aquila. The difference with the previous case was the absence of ties, as well as the slenderness of the piers, which were not able to provide sufficient restraint to the axial elongation. Therefore the spandrels failed in flexure by means of wide vertical cracks at both ends of the spandrel. Also due to out-of-plane accelerations, one of the spandrels collapsed.

Besides the pier-spandrel geometry, there are several other parameters that are influencing the spandrel behavior such as the type of the lintel and the boundary condition provided to the spandrel from the piers. A more analytical investigation of all the parameters influencing the spandrels behavior is attempted in the following section.

Figure 10. Flexure failure of spandrels in an old URM building after the L' Aquila earthquake on 6 April 2009: (a) Entire building and (b) detail of a spandrel. (Beyer and Dazio 2012)

2.3 Experimental experience.

Several experimental investigations have taken place for the characterization of the seismic response of unreinforced masonry structures. Nevertheless most of those are concentrated in the behavior of piers, neglecting the contribution of the spandrels, leading to either under nor overestimation of a masonry building's seismic capacity. Only during the last decade a series of experimental studies started to be carried out, in order to evaluate the actual behavior of this structural component. A research in literature allows to find at least 6 examples of experimental studies, with the most interesting cases being the studies in the University of Trieste (Gattesco et al. 2008), the University of Lausanne (Beyer and Dazio 2012), the University of Naples (Augenti et al. 2011), the University of Pavia (Graziotti et al. 2011), (Graziotti et al. 2014), the University of Auckland (Knox 2012) and the University of Newcastle, Australia (Allen et al. 2016).

2.3.1 Experiment description

Regarding the experimental part, those 6 different studies, execute a series of tests in specimens of different dimensions and properties. All the specimens were built with a characteristic H-shape, in

order to evaluate the behavior of spandrels between openings of two adjacent floors. As it is observed in Figure 11 the specimens can be divided in two categories, depending on the position of the spandrels. This configuration is connected with the type of the experimental setup (Figure 12). In the first category of specimens, where the spandrel is located in the middle height of the piers, the test was executed by imposing cyclic vertical rotation or displacement to the spandrels, while in the second category, where the spandrel is located at the top of the piers, the loading is applying by horizontal monotonic or cyclic displacement to the top of the frame. Tests on larger specimens or whole facades have been also carried out in the former years but since they are out of the scope of this thesis, that has been limited to the combination of piers plus spandrel.

Comparing the two different setups, it should be commented that the first category has the advantage of been a statically determined system, which gives the opportunity of obtaining the axial, shear forces and bending moments acting at the spandrel (Graziotti et al. 2011). The disadvantage of this setup is that the piers remain macroscopically undamaged, while the study of a whole portal frame is able to overtake this drawback, allowing the boundary conditions to be modified during the test, although the information about the actual forces is lost.

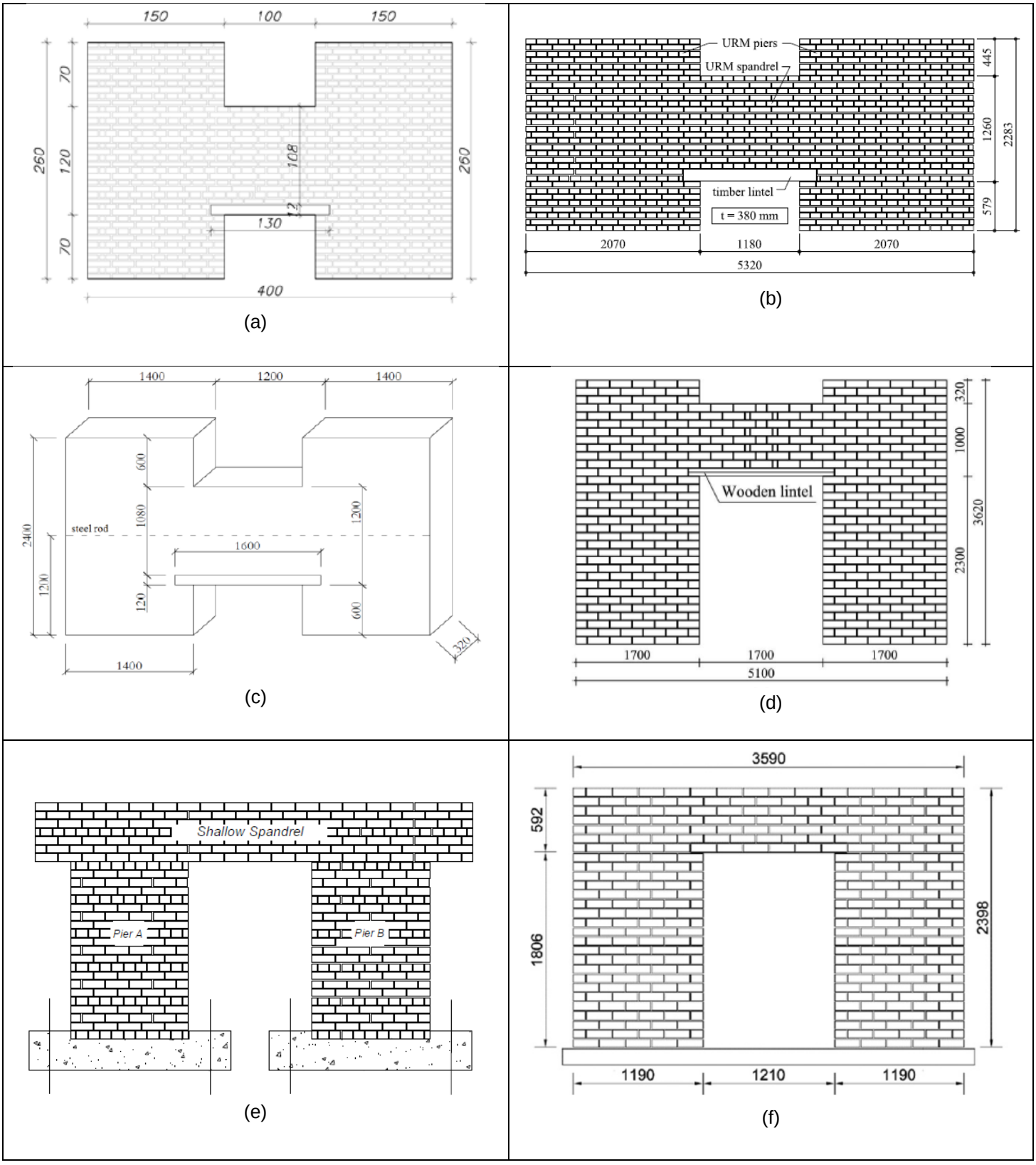

Figure 11. Specimens' geometry from different experimental campaigns. (a) Gattesco et al. (2008) (b) Beyer & Dazio (2012)(c) Graziotti et al. (2011) (d) Augenti et al. (2011) (e) Knox (2012) (f) Allen et al. (2016).

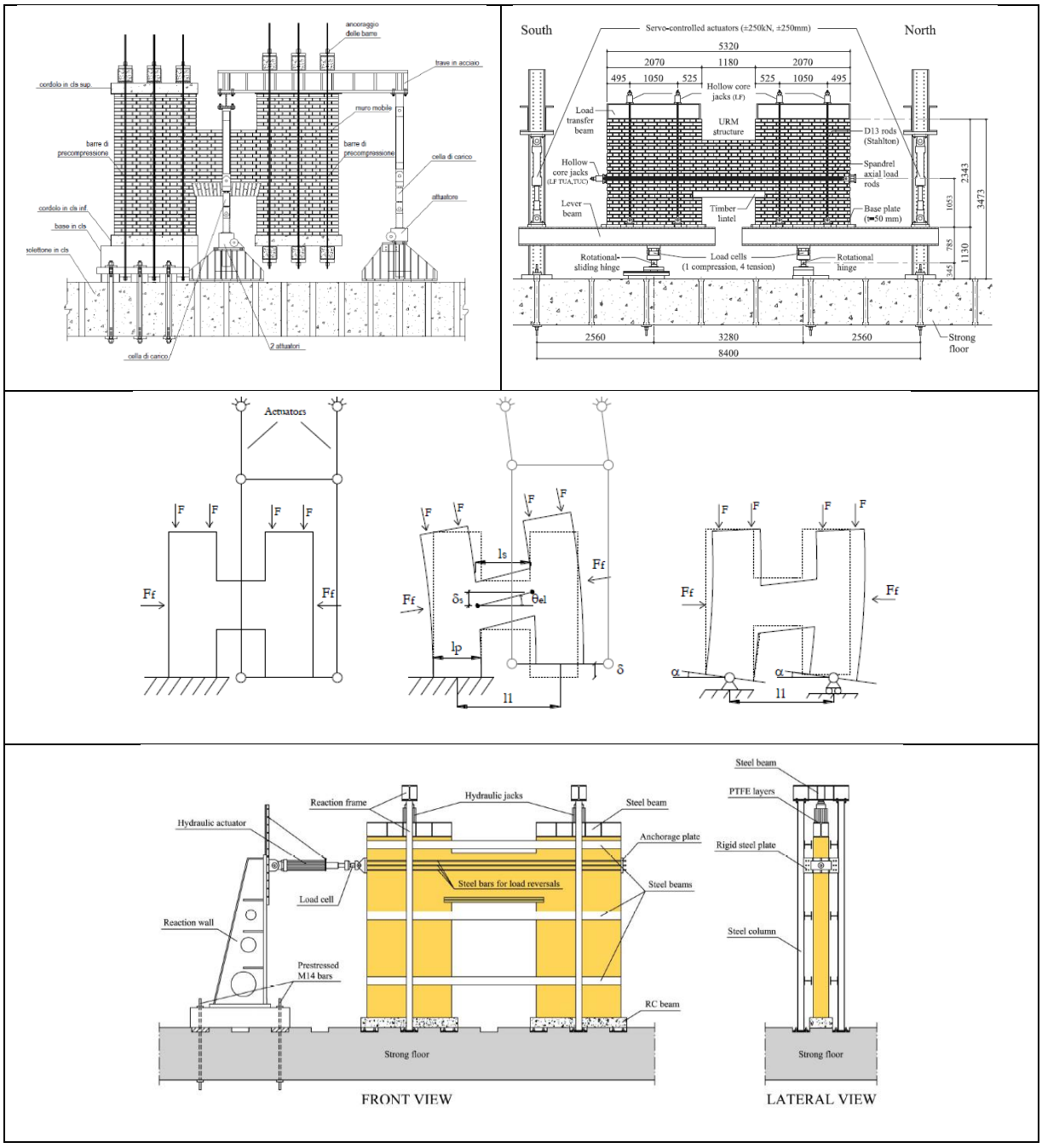
ancoraggio delle barre
trave in acciaio
cordolo in cls sup.
muro mobile
barre di precompressione
barre di precompressione
cella di carico
attuatore
cordolo in cls inf.
base in cls
soletttone in cls
2 attuatori
cella di carico
South
Servo-controlled actuators (±250kN, ±250mm)
North
5320
2070
1180
2070
495
1050
525
525
1050
495
Hollow core jacks (LF)
Load transfer beam
URM structure
D13 rods (Stahlton)
Hollow core jacks (LF TUA,TUC)
Spandrel axial load rods
Lever beam
Timber lintel
Base plate (t=50 mm)
1053
2543
3473
785
1130
345
Rotational sliding hinge
Load cells (1 compression, 4 tension)
Rotational hinge
2560
3280
2560
8400
Strong floor
Actuators
F
Ff
ls
δs
θel
lp
δ
ll
α
Reaction frame
Hydraulic jacks
Steel beam
Hydraulic actuator
Anchorage plate
Steel bars for load reversals
Steel beams
Load cell
Reaction wall
Prestressed M14 bars
RC beam
Strong floor
FRONT VIEW
Steel beam
PTFE layers
Rigid steel plate
Steel column
Strong floor
LATERAL VIEW

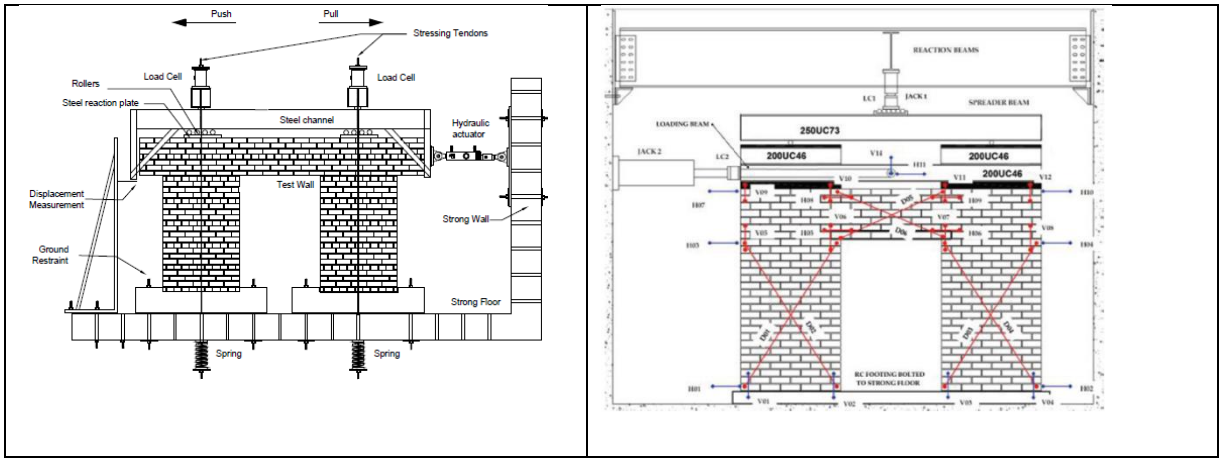

Figure 12. Test setup from different experimental campaigns. (a) Gattesco et al. (2008) (b) Beyer & Dazio (2012)(c) Graziotti et al. (2011) (d) Augenti et al. (2011) (e) Knox (2012) (f) Allen et al. (2016).

As far as the material properties of the specimen are considered, a variety of different types of blocks and mortar were used. An analytical description of the units and mortars is presented in Table 1. Also a series of tests were executed from the researchers in order to evaluate the mechanical properties of the masonry used (Table 2). Those properties were used for numerical studies or the interpretation of analytical formulations.

Table 1. Type of units and mortar for each experimental campaign.

Experimental Campaign	Type of units	fb (MPa)	Type of mortar	fm (MPa)
Augenti et al. (2011)	Tuff stones	4	Pozzolan	2.5
Gattesco et al. (2008)	Clay bricks	>44	Unknown	<2.5
Beyer & Dazio (2012)	Clay bricks	36	Cement	>10
Graziotti et al. (2011)	Stone	-	NH Lime	<2
Allen et al. (2016)	Bricks	-	Cement+lime	-
Knox (2012)	Recycled clay bricks	25	Cement+lime	2.9

Table 2. Mechanical characteristics of the masonry for each experimental campaign.

Experimental Campaign	fc (MPa)	E (MPa)	ft (MPa)	G (MPa)
Augenti et al. (2011)	3.96	2159	0.15	854
Gattesco et al. (2008)	7	4626	-	-
Beyer & Dazio (2012)	6.2	-	-	-
Graziotti et al. (2011)	3.28	2550	0.137	840
Allen et al. (2016)	9.6	9573	-	-
Knox (2012)	9.2	-	-	-

2.3.2 Results-Conclusions

The six different experimental campaigns execute a series of test with specimens of different geometry, materials and properties. In the following paragraph there is an attempt to categorize the results from every campaign and elaborate the results to describe the failure modes and strength of masonry spandrels.

Effect of spandrel depth

The influence of the spandrel aspect ratio was evaluated by Knox (2012) and Allen et al. (2016)

Knox (2012) tested three specimens with the same pier dimensions but different spandrel depth. The results and damage patterns are presented in Figure 13 and Figure 14. Specimen PS1 had a shallow spandrel depth, PS3 a medium and PS4 a large one. As it is observed the spandrel depth leads to an increasing of the lateral capacity of the specimens but not significantly. The crack pattern was in every case characterized as shear. The failure mode indicated that the lateral force was resisted predominantly by the pier rocking.

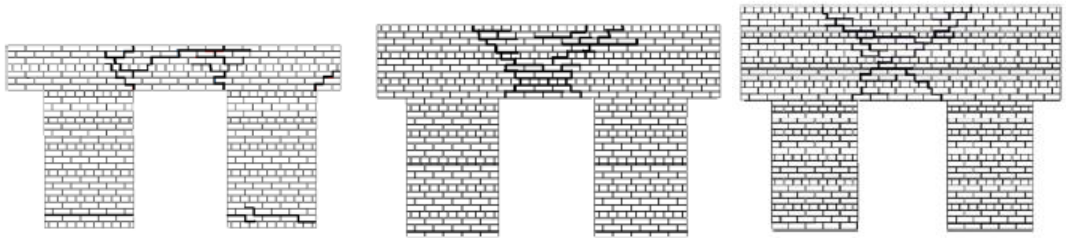

Figure 13. Crack pattern of specimens PS1, PS3 and PS4 respectively. (Knox 2012)

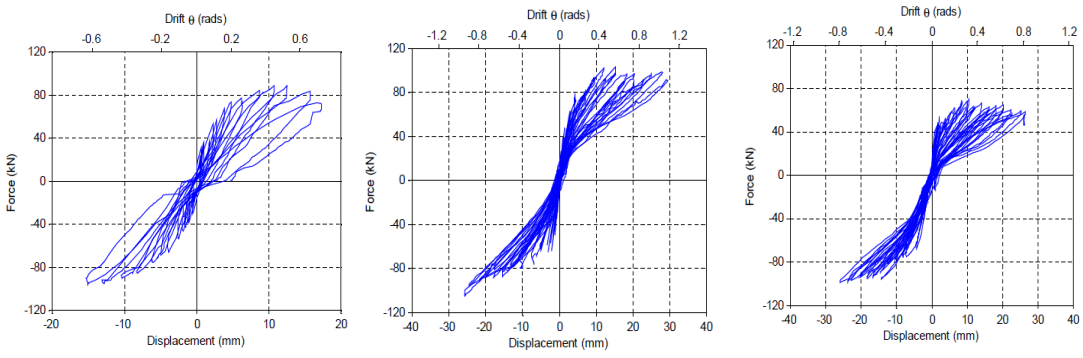

Figure 14. Force-displacement diagrams of specimens PS1,PS3 and PS4 respectively. (Knox 2012)

Allen et al. (2016) investigated also the effect of spandrel's dimensions to its behavior. More specifically specimens with the same pier dimensions and different spandrel depths were tested. The crack pattern and the force displacement diagrams of two specimens are illustrated in Figure 15 and Figure 16. As it is observed, both specimens failed in shear, while in the case of shallow spandrel

there was observed shear failure of the piers too. In terms of capacity the shallow spandrel specimen showed slightly better behavior in terms of ductility. This difference occurred due to the failure of the piers, which absorbed the lateral displacement more effectively.

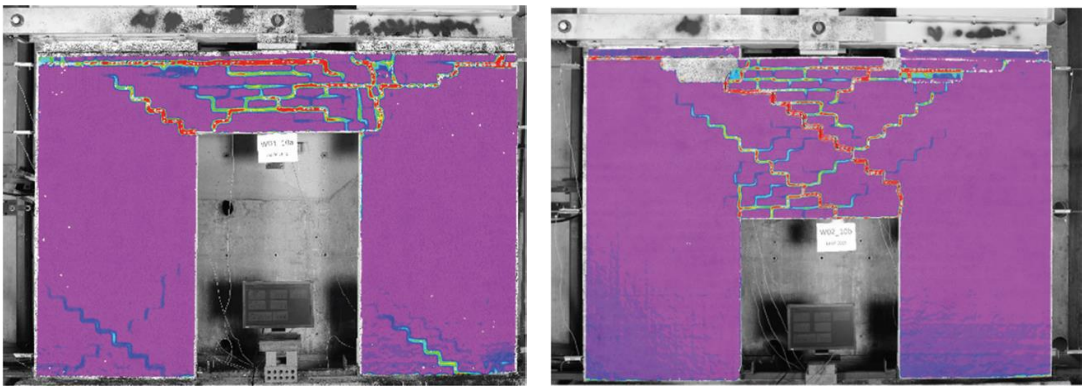

Figure 15. Crack pattern of specimens W01 and W02 respectively. (Allen et al. 2016)

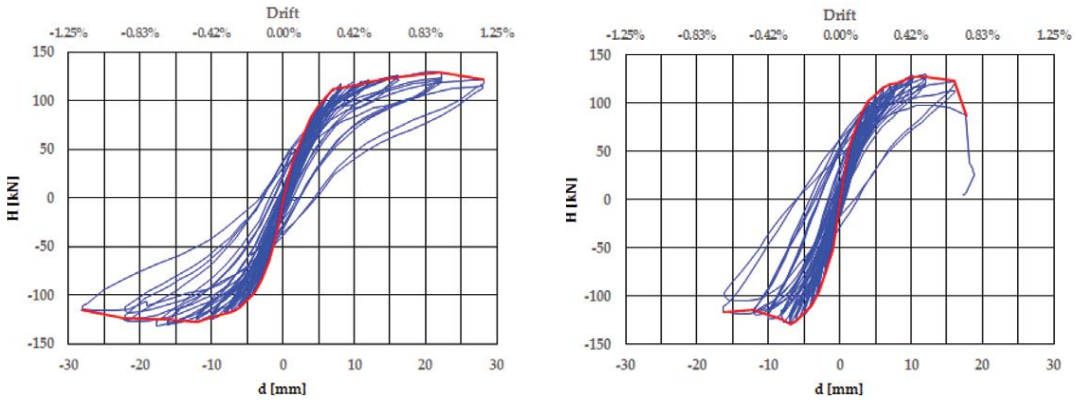

Figure 16. Force-displaceement diagrams of specimens W01 and W02 respectively. (Allen et al. 2016)

Effect of boundary condition

-Piers axial loading

Knox (2012) applied different axial loads to the piers of specimens PS3 and PS5, which had the same identical geometry. PS3 was subjected to an axial load of 0.48 MPa, while PS5 to an axial load of 0.22MPa. The crack pattern and the force displacement diagrams of the two specimens are illustrated in Figure 17 and Figure 18. The failure mode of the piers and spandrel in both substructures was identical and the crack patterns were similar, leading to the conclusion that the relative change in axial stress was insufficient to cause a change in failure mode for consistent pier geometry. The maximum lateral force for PS3 was 35% higher than the maximum lateral force recorded for PS5. The drift at maximum force for PS5 was 3.4 times the drift at maximum force for PS3. These results indicated that axial load increases the capacity of rocking governed piers when subjected to lateral forces, but decreases the ductility.

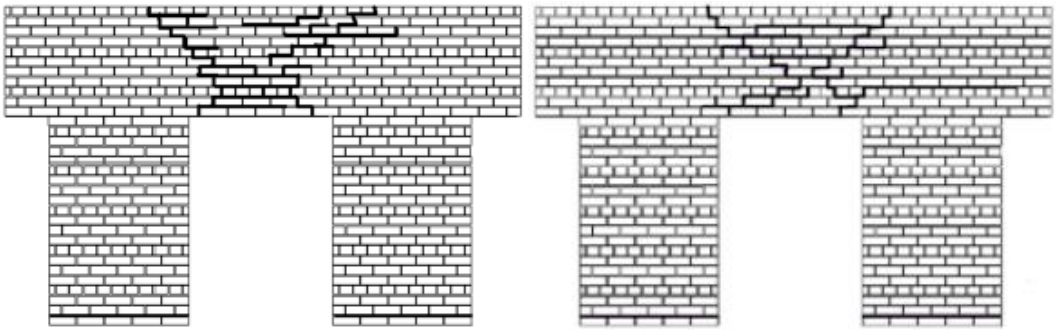

Figure 17. Crack pattern of specimens PS3 and PS5 respectively. (Knox 2012)

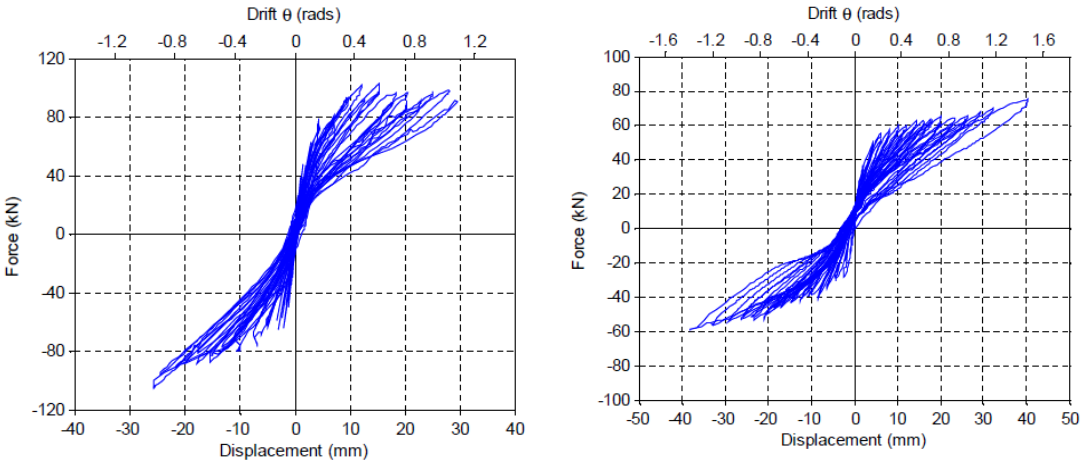

Figure 18. Force-displaceement diagrams of specimens PS3 and PS5 respectively. (Knox 2012)

-Spandrels axial loading

A very important parameter affecting the behavior of masonry spandrels is the axial loading, which is affected by the boundary condition between them and piers. In reality, this boundary condition is modified during an earthquake action. For this reason, it is not possible for a single value of axial load to be adopted during an experimental test. The researchers at the University of Pavia (Graziotti et al. 2011), and Lausanne (Beyer and Dazio 2012) applied different values of axial loading to specimens with identical geometry, in order to study the effect of this modification to the spandrel's behavior.

More specifically Graziotti et al. (2011), tested two identical specimens S1 and S2 with values of axial loading equal to 0 for S1 and a variety of values for S2 from 19 to 75 kN. The crack pattern and the force displacement diagrams of the two specimens are illustrated in Figure 19 and Figure 20. The difference between the two specimens is significant in terms of failure mode. Specimen S1 showed a flexural failure mechanism, while S2 a shear one. This influenced the hysteretic behavior characterized by higher strength and small residual crack widths in case of horizontal compression (limited damage for lower drift values), low strength and large residual cracks in case of absence of

compression. As regards the capacity, the implementation of axial force increased the load capacity, as well as the ductility. The stiffness though remained uninfluenced.

Figure 19. Crack pattern of specimens S1 (without axial load in spandrel) and S2 (with axial load) respectively. (Graziotti et al. 2011)

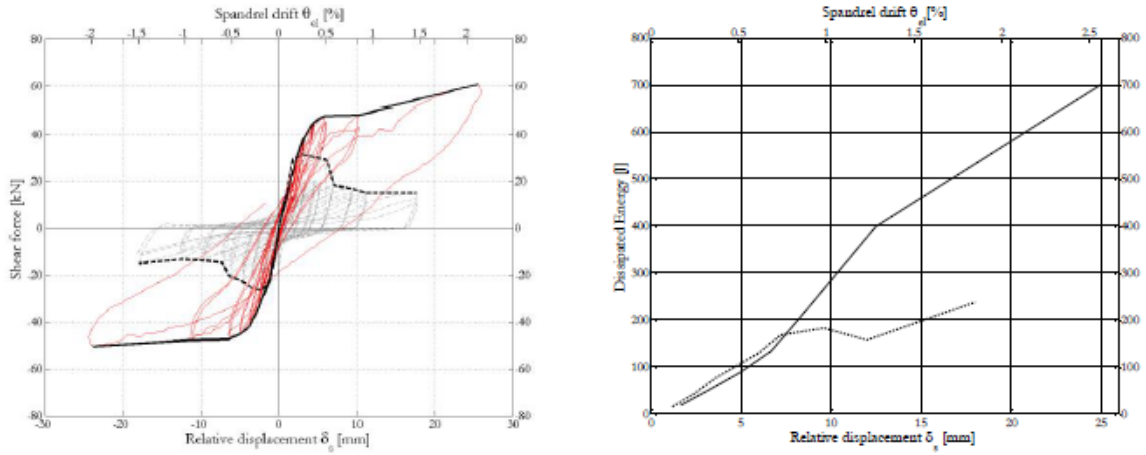

Figure 20. Comparison between force-relative displacement δ_s cycles (S1, dashed - S2, solid) (left); dissipated energy per cycle vs. relative displacement δ_s (S1, dashed - S2, solid) (right). (Graziotti et al. 2011)

Beyer & Dazio (2012) tested specimens of different type of lintels (wooden and brick arch), with and without the application of axial loading to the spandrel. The crack pattern and the force displacement diagrams of the two specimens are illustrated in Figure 21 and Figure 22. Like the experiments performed at the University of Pavia, once again the implementation of axial load to the spandrels altered their behavior significantly. First it modified the failure mechanism from flexural to shear. Regarding the load capacity, there was no significant increase in the maximum load. Nevertheless the ductility of the specimen doubled from a rotation drift of 1.5% to 3%.

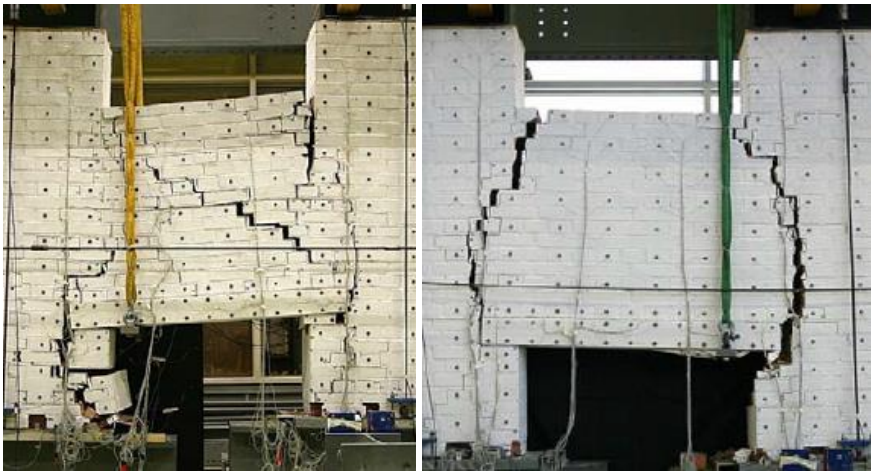

Figure 21. Crack pattern of specimens TUA (80 kN axial load) and TUB (0 kN axial load) respectively. (Beyer and Dazio 2012)

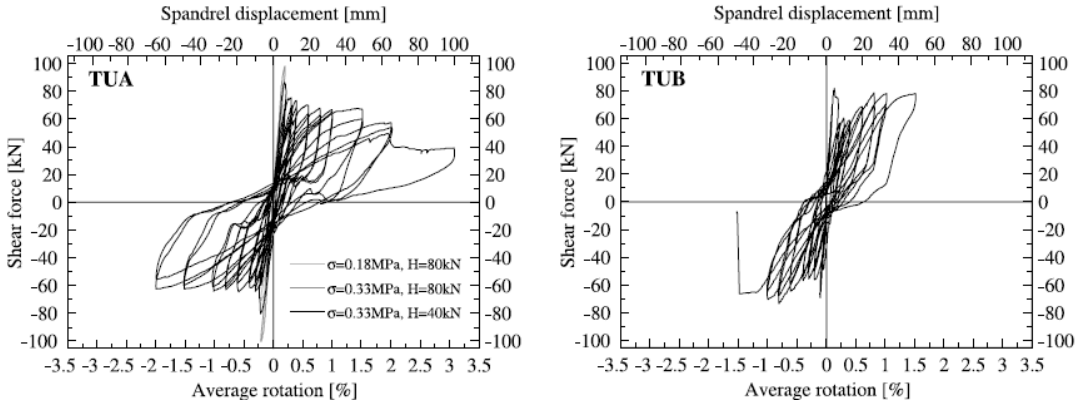

Figure 22. Force-displacement diagrams of the tested specimens. (Beyer and Dazio 2012)

Effect of lintel type

The experience derived from the observation of failure types on real structures after earthquakes, highlight the importance of the lintel type for the behavior of the masonry spandrel. The experimental campaigns that took place in the University of Pavia (Graziotti et al. 2014) and Lausanne (Beyer and Dazio 2012) investigate the influence of the timber and masonry arch lintel to the behavior of the masonry spandrels.

Graziotti et al. (2014) tested 2 full-scale specimens with the same dimensions and properties, but different thickness of lintels. Specimen S3 was built with a timber lintel of 12 cm, while the lintel of specimen S4 had a height of 2.5 cm. The crack pattern and the force displacement diagrams of the two specimens are illustrated in Figure 23 and Figure 24. The crack pattern in both occasions was characterized as shear. The presence of the timber lintel in both cases prevented the collapse of stones at the lower part of the spandrel, although excessive damage occurred. Comparing the force displacement diagrams it is observed an increase of the spandrel's load capacity due to the presence

of a thicker lintel, from 22 to 35 kN. In addition it seems to prevent a softening behavior of the specimen an increased the dissipated energy.

Figure 23. Crack pattern of specimens S3 and S4 respectively. (Graziotti et al. 2014)

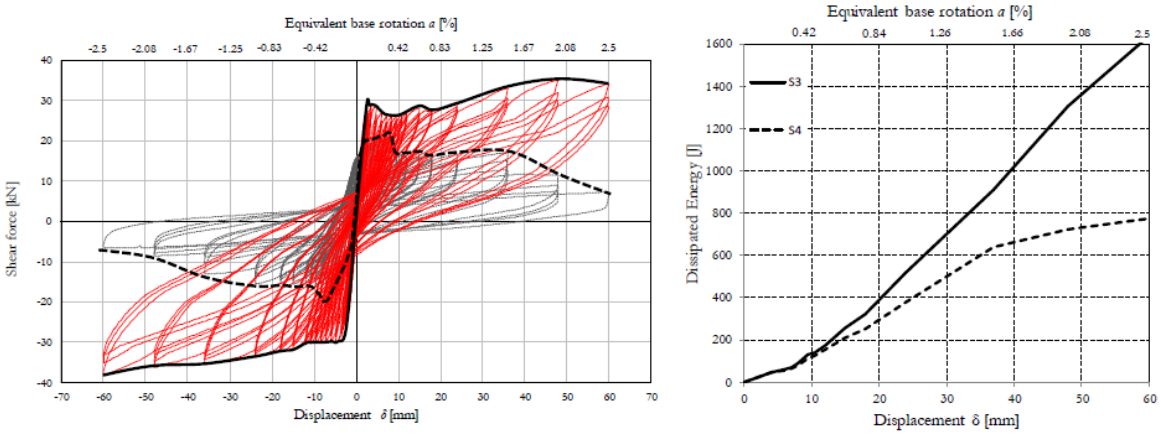

Figure 24. Comparison between force-displacement *δ* cycles (S4, dashed – S3, solid) (left); dissipated energy per cycle vs. displacement *δ* (S4, dashed – S3, solid) (right). (Graziotti et al. 2014)

Beyer & Dazio (2012) investigated the influence of different type of lintels, by testing spandrel specimens with linear timber and arch brick lintel. The crack pattern and the force displacement diagrams of the two specimens are illustrated in Figure 25 and Figure 26. For specimen TUC (arch lintel) the loss in strength was significantly larger than for the TUA specimen with timber lintel since the timber lintel contributed substantially to the integrity of the spandrel at large rotation demands. When the spandrel was damaged the timber lintel served as a support for loose parts of the spandrel. The masonry arch on the contrary was prone to damage and eventually collapsed for higher rotation drifts.

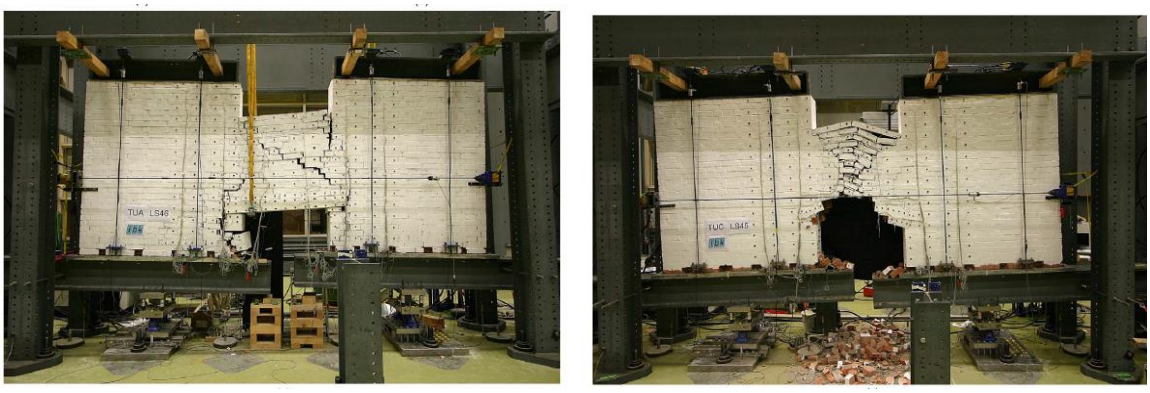

Figure 25. Crack pattern of specimens TUA and TUC respectively. (Beyer and Dazio 2012)

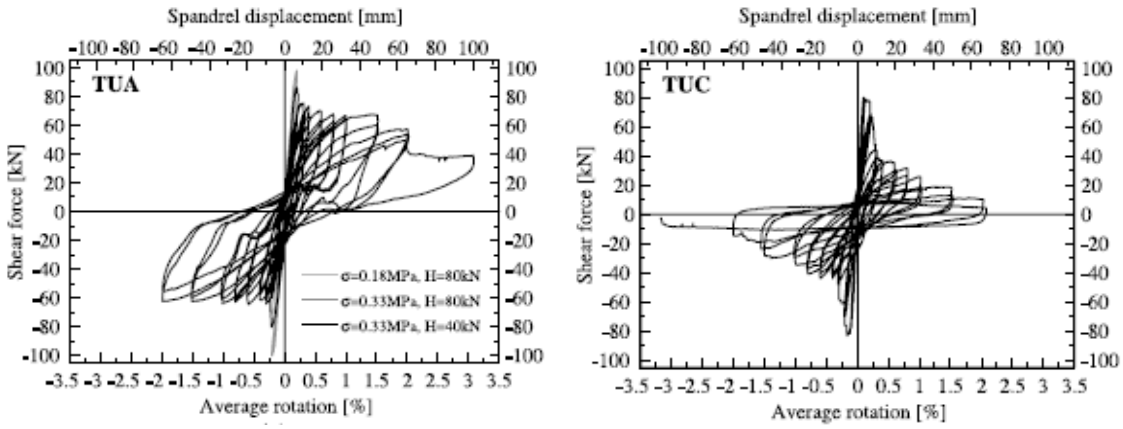

Figure 26. Force-displacement diagrams of specimens TUA (timber lintel) and TUC (arch lintel) respectively. (Beyer and Dazio 2012)

Strengthening techniques

An important aspect of the study about the behavior of masonry spandrels is also the evaluation of existing and new techniques of strengthening in case of severe damage during earthquakes. Augenti & Parisi (2011) presented the evaluation of the lateral strength of a portal frame to monotonic loading. After the implementation of a horizontal displacement equal to 2.8 cm, the tested specimen was repaired with grout injection and then tested again to cyclic load. Finally the specimen was once again repaired and strengthened with the application of a glass-fiber reinforced matrix to both sides of the spandrel. The matrix consisted of a lime-based coating mortar with an addition of glass fibers, as well as a bidirectional alkali resistant glass coated net. The results showed a negligible contribution of the grouting injection to the strengthening of the masonry spandrel. More specifically this technique did not manage to restore the initial strength of the as-built specimen (Figure 27,Figure 28). In the case of the fiber glass matrix strengthening, the initial load capacity of the tested specimen was fully restored (5 kN increase) and the ductility was significantly increased (Figure 28). Another important aspect is the strengthening of the portal frame without the modification of the specimen's stiffness.

This technique proved to significantly upgrade the performance of portal frames to in plane lateral loads, with respect to the principles of compatibility and reversibility.

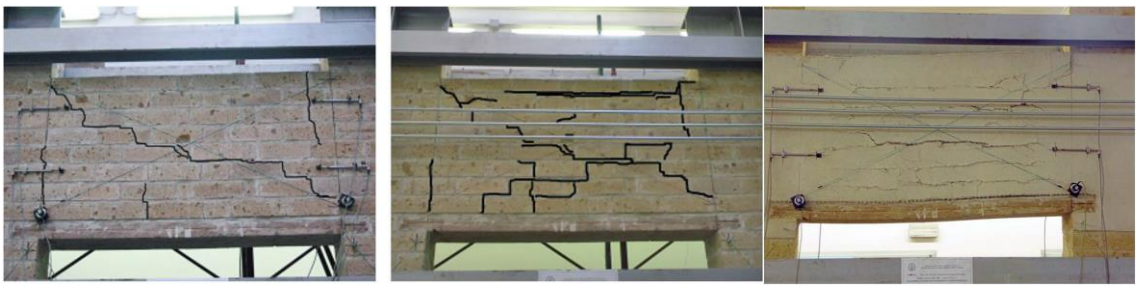

Figure 27. Damage pattern of the (a) as built (b) repaired and (c) strengthen specimen. (Augenti and Parisi 2011)

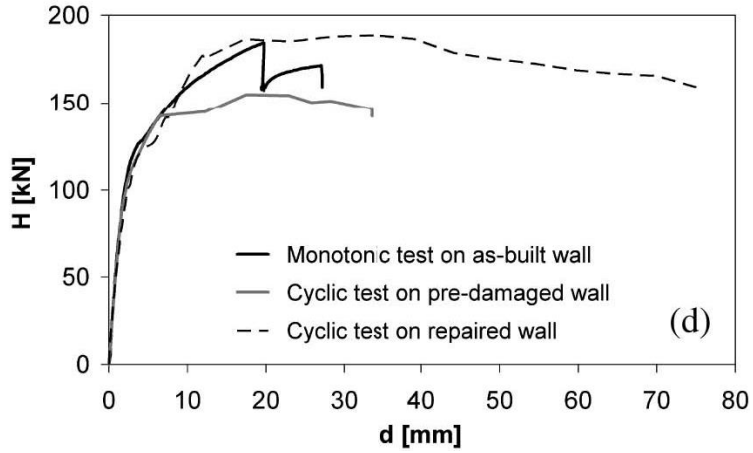

Figure 28. Experimental force-displacement diagrams, envelopes. (Augenti and Parisi 2011)

2.4 Structural analysis of masonry façades

2.4.1 Introduction

The previous section emphasized the importance of spandrels to the in plane response of masonry façades, and attempted to determine their behavior due to seismic loads from both experimental campaigns and observation of post-earthquake areas. After the collection of this knowledge, the next step of this study was the selection of the appropriate tool to analyze the behavior of the masonry spandrels. In this section a state of the art review of the literature is presented, including all the main numerical and simplified analytical approaches that are available for the structural analysis of masonry façades. In the end of this section the final conclusions from this search are made, as well as the selection of the appropriate model that is going to be used in the current study.

2.4.2 Numerical approaches

2.4.2.1 FEM Analysis

Among the different techniques that exist for numerical analysis of structures, Finite Element Analysis offers a huge variety of possibilities for the simulation of historical masonry structures in terms of detailed nonlinear analysis (Roca et al. 2010). Among the variability of FEM analysis techniques, adequate tools should be chosen considering cost, need for experienced users/engineers, level of accuracy required, availability of input data, need for validation and the use of the results (Lourenço 2002). The two main modelling approaches that have been used for historical constructions are the micromodelling and the macromodelling approach. In the following section a brief description of every technique's principle is presented, with an application example to masonry spandrels.

Micromodelling approach

-Principle

In the micromodelling method, the different components of the masonry, namely the units and the mortar and their interfaces are described separately. There are two different types of micromodelling, the detailed and the simplified one. Detailed micro models represent units and mortar with continuum finite elements while unit-mortar interface is represented with interface elements. This approach take into account Young's modulus, Poisson's ratio and, optionally, inelastic properties of both unit and mortar. The interface includes a potential crack/slip plane with initial dummy stiffness to avoid interpenetration of the continuum. This permits the combined action of unit, mortar and interface to be studied under a magnifying glass (Zucchini and Lourenço 2002). Although this approach can represent the behavior of masonry with sufficient accuracy, the large computational effort that requires, make it inappropriate for complicated structures. Therefore a simplified micromodelling approach was created, as a more accurate approach than macromodelling, but with less computational effort than the detailed method (Lofti and Shing 1994), (Lourenço 1994), (Lourenço and

Rots 1997), (Sutcliffe et al. 2001). In this method expanded units represented by continuum elements, are used to model both units and mortar material, while the behavior of the mortar joints and unit-mortar interfaces is lumped to the discontinuous elements.

-Examples of application to masonry spandrels

Parisi et al. (2011)

Based on the experimental campaign of Augenti et al. (2011) a micromodelling simulation was applied in order to evaluate the behavior of masonry facades. The model was calibrated on a specimen subjected to monotonic horizontal loading. Both mortars and units were modeled with quadrilateral isoparametric plane stress element, which were based on quadratic interpolation and Gauss integration. Most of the mechanical parameters were obtained by experimental results, while the compressive fracture energy of the mortar was determined by calibrating the FE model. The model managed to obtain the same load capacity as the experimental (Figure 29), as well as a satisfying though diffused crack pattern. This study is going to be explained in detail in section 3.2.5.1.

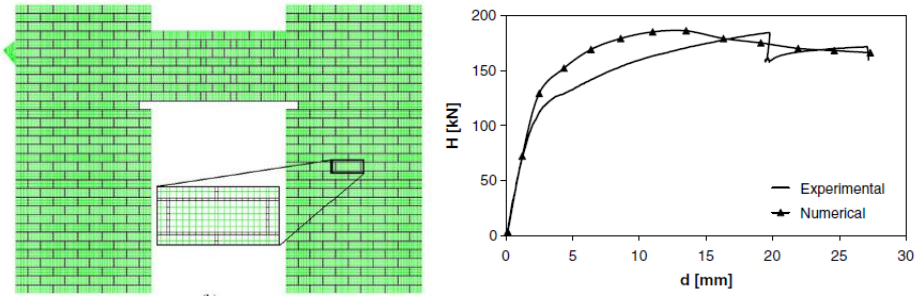

Figure 29. Numerical model and comparison of results with the experimental ones. (Parisi et al. 2011)

Beyer & Mangalathu (2014)

Based on their experimental campaign (Beyer and Dazio 2012) a micromodelling simulation was applied in order to evaluate the behavior of masonry facades. The model was calibrated on a half-portal frame specimen subjected to monotonic rotation of the piers. Although the experimental test included a cyclic loading, experiment and numerical model were compared in terms of global response. The units were modeled with plane stress isotropic elements of quadrilateral shape with elastic behavior, while the mortar was represented by interface elements with zero thickness. The initial failure surface, which characterizes the peak strength of the joint, follows a Mohr-Coulomb law with an ellipsoidal failure surface in the tension regime. Once the interface reaches its maximum shear stress τ, it loses its cohesion c and tensile strength f_t. The residual failure surface accounts only for friction. The tensile and shear softening are defined based on the fracture energy associated with each mode.

Due to the simulation of the mortar joints as elements with zero thickness, the units were simulated with slightly increased dimensions as the real ones. As a consequence the initial analysis with the tensile fracture energy measured by experiments, did not give a representative behavior regarding the

maximum capacity. Once the fracture energy was increased 3.5 times, the numerical capacity curve reached an adequate convergence with the envelope of the experimental hysteretic cycles (Figure 30).

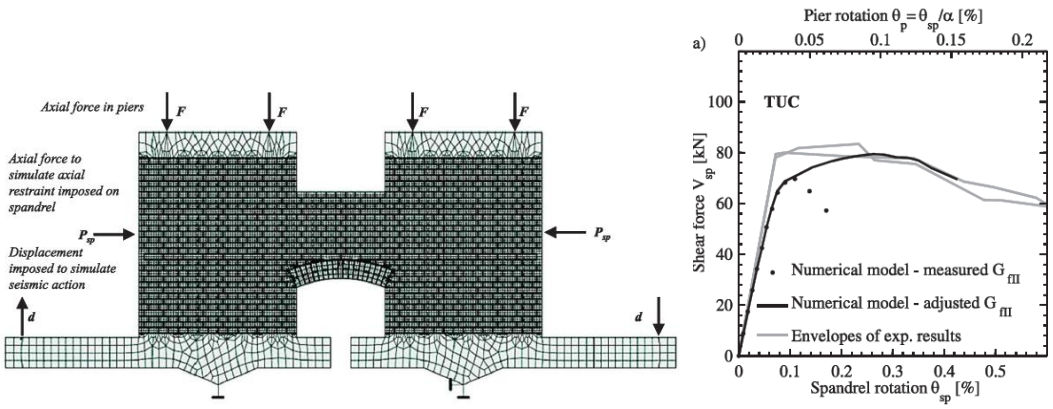

Figure 30. Numerical model and comparison of results with the experimental ones. (Beyer and Mangalathu 2014)

Macromodelling approach

-Principle

The macromodelling approach consists of a FEM method which does not differentiate between individual units and joint. Instead, it considers masonry as a homogeneous continuum. This approach is practical when a compromise between accuracy and efficiency is required. In a macromodel different values of tensile and compressive strength should be taken into account, as well as different inelastic properties for each material axis. A macromodel's mesh is also simpler than the micromodelling approach, since it is not describing the internal structure, therefore the mesh size could be bigger than an individual unit (Roca et al. 2010).

An important parameter of the macromodelling technique is the use of different approaches for the plasticity or the damage constitutive laws. An example of using Continuum Mechanics finite element models is the study of Lourenço (1997) where an approach for in-plane loaded walls was developed. The author combined a concept of plasticity with anisotropic material behaviour by applying different hardening/softening behaviour in each material axis. A Rankine-like yield surface for tension and a Hill-like yield surface in compression were adopted. As a result, the model showed different behaviour along each direction. Implementation of this model ended in satisfactory results in terms of collapse loads and reproduced behaviour. Other examples of orthotropic models is the orthotropic model of Papa (1997), which is containing a homogenization technique, which aims to take into account the interaction between brick and mortar, due to their texture. As a matter of fact, Pelà et al. (2013) proposed a macro-model, based on continuum damage mechanics, for the in-plane analysis of masonry structures. The orthotropic behavior of the material is simulated by means of an original

methodology, resulting from the concept of mapped tensors from the anisotropic field to an auxiliary workspace (Pelà et al. 2011).

A drawback of the macromodelling technique is the smeared crack approach, which is resulting a diffused damage pattern. This is not in a good correspondence with reality, since damages are often appearing in a structure as localized cracks. A proposed solution for this problem was the use of crack tracking algorithm (Clemente 2006), to represent the damage in a more localize and realistic way. This approached was used for the structural analysis of the Mallorca Cathedral, with satisfying results (Clemente et al. 2006).

-Examples of application to masonry spandrels

There are several examples from the application of the macromodelling approach to masonry structures. A case of macromodelling simulation concentrated in masonry spandrels is the Saloustros et al. (2016) model. Based on the experimental campaign of Augenti et al. (2011) a macromodelling simulation was applied. The purpose of this study was the evaluation of a crack-tracking algorithm as a tool for non-linear analysis of structures. The masonry frame is discretized in an unstructured mesh of 2D plane-stress three-noded triangles with average mesh size of 4 cm. The results showed a very satisfying correspondence to the experimental ones, proving that the macromodelling approach, when combined with improved methods as the crack-tracking, can overcome the disadvantages of the smeared crack approach which result to diffused damage model. Therefore it can be a powerful tool for simulating masonry facades, requiring much less computational cost than micromodelling (Figure 31).

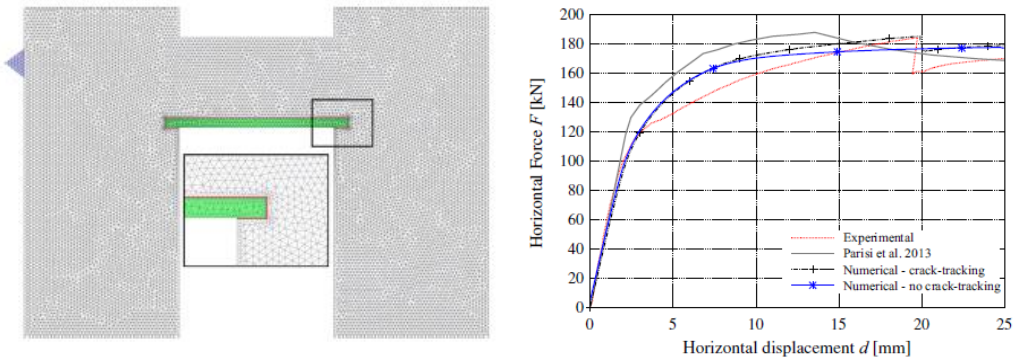

Figure 31. Numerical model and comparison of results with the experimental ones. (Saloustros et al. 2016)

2.4.2.2 Equivalent frame method

-Principle

Equivalent Frame (EF) models are an idealization of a perforated wall as a frame, with pier and spandrel beam elements and rigid offsets to model the joints. There are two general approaches to modelling the non-linear response of the piers and spandrels. The first approach employs elastic beam elements and plastic hinges located at the critical deformation points, which are activated when the shear or moment reaches the code defined strength for a particular failure mode. The second approach uses a non-linear beam with a defined non-linear material constitutive law. The Equivalent Frame model was adapted from non-linear analysis tools used for reinforced concrete frames, and can consider the non-linear behaviour of both the spandrel and the pier (Kappos et al. 2002).

The Equivalent Frame model has been used to model experimental programs and existing buildings to verify its application to unreinforced masonry buildings (Belmouden and Lestuzzi 2009), (Magenes and Fontana 1998), (Pasticier et al. 2007), (Sabatino and Rizzano 2010), (Saloustros et al. 2016). This approach to modelling unreinforced masonry in plane loaded perforated walls is presented as an attractive option for practicing engineers as the elements required are available in many commercial programs, and specialist software with added complexity are becoming more accessible. Another advantage of this method is the requirement of less material properties as the Finite Element models, which would be difficult to be assumed and could only be defined properly by a series of diagnosis and inspection tests.

Nevertheless the use of this method should be done with great caution, since its accuracy is based on the reliability of specific analytical equations that have been proposed by building codes, or researchers. Another critical aspect of the Equivalent Frame method is the appropriate geometrical modeling configuration. In case of regular and especially irregular type of geometry in unreinforced masonry buildings, the appropriate selection of frame scheme, including the appropriate geometry properties for piers and spandrels, can affect significantly the results of an Equivalent frame model. A recent study presented by Structures et al. (2017) examined the influence of those geometrical parameters and irregularities for the in plane assessment of unreinforced buildings, proposing specific frame scheme selections, which were compared with FE models for their validation.

-Examples of application to masonry spandrels

Knox (2012)

Based on the experimental test, including the cyclic horizontal displacement of portal frame specimens, a numerical model was created, based on the equivalent frame method. The shear behaviour was included through non-linear links placed at the mid-height of the piers, and at mid-span of the spandrels. To define a non-linear link to model the shear behaviour, a multi-linear plastic type link was selected, and all the directions of the link were defined as ‘fixed’, except for the critical

translational direction, which controlled the non-linear behaviour. No mass, weight or rotational inertia needed to be applied to the link.

Flexural behaviour was included in the Equivalent Frame model by defining coupled hinges positioned at both ends of the effective pier height, and at both ends of the spandrel span. Using a hinge, rather than a non-linear link, it was allowed direct implementation of the moment-axial strength domains.

The results were satisfying, managing to capture the capacity of the frame and the main failure mechanisms (Figure 32).

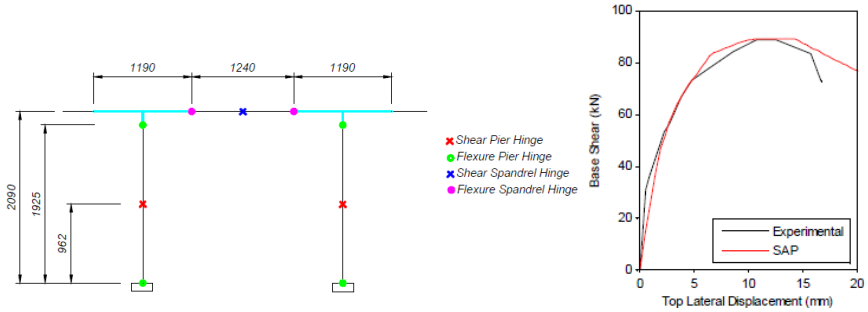

Figure 32. Hinge position for substructures comparison of results with the experimental ones. (Knox 2012)

2.4.3 Analytical approaches

Previous studies have highlighted the importance of masonry spandrels in the seismic capacity of unreinforced masonry buildings (Benedetti and Magenes 2001), (Yi et al. 2006). Nevertheless most of the building codes and regulations tend to ignore the contribution of masonry spandrels adopting the strong pier-weak spandrel model, which leads to full uncoupling of the piers and underestimate the in-plane capacity of masonry facades. Another approach is the weak pier-strong spandrel model which tends to the adoption of infinite strength and stiffness for the spandrel. This section will mention and describe the main simplified analytical expressions that exist in bibliography and regulations, for the in-plane strength of masonry spandrels. Those expressions can be used to equivalent frame models for the assessment of unreinforced masonry buildings.

Eurocode 8 ((CEN) 1998) allows the inclusion of spandrel panels in equivalent frame capacity models only in cases where tensile resistant elements are present, such as in reinforced concrete bond beams, or steel ties. This approach therefore is unsuitable for a big amount of existing historical masonry buildings where there is not presence of those elements.

The Italian Ministry of Infrastructure and Transport (2008) includes two equations for the evaluation of the spandrel strength, in the case of the presence of horizontal tensile resistance elements. (Equations 1-2). Those equations include the calculation of the flexural and shear strength, with the

spandrel strength being the lesser of the two. In case of absence of those elements the spandrel influence to the lateral resistance of unreinforced masonry is neglected.

$$Vf = \frac{d_s H_p}{2}\left(1 - \frac{H_p}{0.85 f_{hu} d_s t_s}\right) \quad (1)$$

$$V_s = d_s b_s f_{vo} \quad (2)$$

H_p the minimum tension resistance of the tensile resistance element

f_{vo} cohesive strength of mortar bed joints

FEMA 306 ((ATC-43 Project) 1998) allows for two different mechanisms associated with either the flexural or shear capacity. In particular, the moment capacity of uncracked spandrels is obtained considering the interlocking at the interface between the pier and the spandrel. For the analyzed walls without collar joints, interlocking takes place only at the bed joints. An elastic stress distribution is assumed at the end of the spandrel with the neutral axis located at the centerline of the spandrel height. The tension and compression resultant forces are derived from the mortar shear strength allowing for the cohesion f_{v0} and the frictional contribution due to compressive stresses in the mortar bed joints.

The expression for the flexural capacity of the spandrel is:

$$M_{R1} = \frac{2}{3} f_{teq} t_s b_h d' \eta \quad (3)$$

Where b_h the thickness of a brick plus the thickness of a mortar joint

d’ the spandrel thickness without the lintel

η, coefficient equal to $\eta = \frac{d'}{4b_h}$

f_{teq} the equivalent tensile resistance due to interlocking which is given by

$$f_{teq} = \frac{b_{eff}}{b_h}\left(f_{vo} + a\sigma_p\right) \quad (4)$$

b_{eff} the effecting interlocking length, equal to 1/2 of the unit thickness

σ_p corresponds to the vertical compressive stress in the adjacent pier

α a reduction factor taken as 0.65 according to Cattari & Lagomarsino (2008)

Thus the shear resistance V_{R1} associated with the flexural capacity can be calculated using equilibrium considerations assuming the spandrel with fixed ends.

$$V_{R1} = \frac{M_{R1}}{b_s} \quad (5)$$

The second failure mode that the FEMA 306 ((ATC-43 Project) 1998) takes into account is the diagonal cracking. The resistance of spandrels in shear is calculated by the equation:

$$V_{R2} = f_{tm} d' t_s \beta \sqrt{1 + \frac{\sigma_n}{f_{tm}}} \quad (6)$$

f_{tm} the tensile diagonal strength which, according to the FEMA 273 (ATC (Applied Technology Council) 1997), can be assumed equal to the cohesive strength of mortar bed joints (f_{v0}).

σ_h the horizontal compressive strength normally equal to zero.

$0.67 \leq \beta = \frac{d'}{b_s} \leq 1.00$

Cattari & Lagomarsino (2008) developed a criterion for the evaluation of the flexural strength of masonry spandrels. These formulations are based in the assumption that the spandrel is behaved as an equivalent strut due to the interlocking phenomenon between the spandrel panel and the adjacent masonry. That way an equivalent tensile strength can be defined, which is able to characterize the spandrel element and not the masonry material. The formulations are based on the following hypotheses: the distribution of tensile stresses (perpendicular to head mortar joints) and that of shear stresses (which develop on the bed joint) are assumed to be uniform; the mechanical properties of head joints are negligible.

These hypotheses lead to two main failure mechanisms: *a*) tensile failure of the block; *b*) shear failure of the horizontal mortar joints.

The tensile strength for the first mechanism is defined by the following equation:

$$f_{tu,a'} = \sigma_x = \frac{f_{bt}}{2} \quad (7)$$

Where f_{bt} the tensile strength of the block

For the second mechanism the equation is giving:

$$f_{tu,b'} = \frac{\Delta x}{2\Delta y}\mu\sigma_y \quad (8)$$

Δx the block width

Δy the block height

μ the friction coefficient

σ_y the compressive stresses acting on the end-section of the spandrels

Based on these formulation an equation of maximum bending moment for the spandrel was proposed

$$M_u=(N,\eta,\mu_c,\mu_t) \quad (9)$$

where $\eta=f_{tu}/f_{cu}$

μc the compressive ductility of masonry

μt the tensile ductility of spandrel

The validation of this criterion was conducted by performing a set of parametrical non-linear analyses. For an aspect ratio of 1.35, two phases of damage were recognized. When the maximum shear force was reached, a damage mechanism characterized by opening of the head joints in the tensile corners of the spandrel was observed, following the forming of diagonal cracks which developed at the center of the spandrel and spread out to the corners. With a high aspect ratio spandrel, a rocking mechanism was activated, where cracks developed in the tensile corners without the propagation of diagonal cracks. These conclusions have been valuable for further studies, regarding the characterization of the shear strength of the spandrel, using the horizontal stresses acting on it as a guide.

Parisi et al. (2011) proposed stress-based analytical equations for the assessment of masonry spandrels connected to the following failure mechanisms:

Toe crushing toe crushing, diagonal tension, stair stepped diagonal sliding and bed joint sliding.

The equation corresponding to the toe crushing of the masonry was obtained from a formulation for masonry piers, with the use of the masonry compressive strength parallel to the bed joints, as a modification.

$$V_t = \frac{d_s}{b_s}(1-\bar{N}_d)N_d \quad (10)$$

N_d = applied axial force

$\overline{N}_d$= same value normalized to the ultimate axial force

The equation for the diagonal tensile cracking is based on the yield criterion proposed by Turnšek & Čačovič (1971). The transformation is purely theoretical and is reported in Augenti (2000).

$$V_t = \beta N_u \sqrt{\frac{\overline{N_d}}{p\beta}} \quad (11)$$

β = ratio between the diagonal tensile strength, at zero confining stress, and the uniaxial compressive strength of the masonry;

p = shear stress distribution factor related to the aspect ratio of the panel

N_u the ultimate axial force $N_u=f_{d,m}$ h t_m

$f_{d,m}$,the referential compressive strength of masonry, assumed to be 85% of the actual one

Finally the equation for stair stepped diagonal sliding and bed joint sliding are formulated from the Mohr Coulomb theory.

$$V_{SD} = \frac{1}{p}(\gamma + \mu_\alpha \overline{N}_d) N_u \quad (12)$$

γ = ratio between the sliding shear strength, at zero confining stress, and the uniaxial compressive strength of the masonry

μ_a = fictitious friction coefficient of the entire masonry, which is assumed equal to 0.4 by Eurocode 6 ((CEN) 1996)

A drawback of these equations is that for the calculation of the spandrel shear strength requires an estimation of the axial force on the spandrel.

Beyer (2012) proposed an analytical method for the estimation of the strength of brick masonry spandrels. In this study the peak and residual strength were estimated for both flexural and shear failure was examined.

Flexural failure

The flexural peak strength was estimated from the tensile strength of the head joints and the interlock of the bed joints

The tensile strength of the head joints was estimated using the parabolic tension cut-off criterion for mortar joints proposed by Rots & Lourenço (1993):

$$f_{hj} = \frac{c}{2\mu} \tag{13}$$

The shear stress in the bed joints is transformed into an equivalent tensile strength according to the equation, which was proposed by Cattari & Lagomarsino (2008)

The total equivalent tensile strength of the uncracked masonry spandrel is then calculated as the sum of the tensile strength of the head joints and the equivalent tensile strength of the bed joints:

$$f_t = f_{hj} + f_{bj} \tag{14}$$

The peak flexural moment for which the f_t is obtained is calculating with the assumption of linear distribution of stresses along the spandrel height:

$$M_{p,fl} = \left(f_t + p_{sp}\right)\frac{d_s^2 t_s}{6} \tag{15}$$

By the moment equilibrium the maximum shear force for the flexural mechanism is calculated:

$$V_{p,fl} = \frac{2M_{p,fl}}{b_s} = \left(f_t + p_{sp}\right)\frac{d_s^2 t_s}{3b_s} \tag{16}$$

p_{sp} the mean axial stress in the spandrel

$$p_{sp} = \frac{P_{sp}}{d_s t_s} \tag{17}$$

P_{sp} the axial force in the spandrel

Regarding the residual flexural strength, assuming that it is governed by a diagonal compression strut, with a compression zone depth of $h_c = P_{sp}/0.85 f_{hm} t_s$, the following equation is obtained:

$$V_{r,fl} = \frac{P_{sp} d_s}{b_s}\left(1 - \frac{p_{sp}}{0.85 f_{hm}}\right) \tag{18}$$

f_{hm} the strength of the masonry in the horizontal direction, parallel to the bed joints

Shear failure

Assuming a rectangular section for the spandrel and parabolic distribution of the shear stresses along the height, a formulation of the shear force for which shear cracking is initiating is:

$$V_{cr,sh} = \frac{2}{3}\tau_{max} d_s t_s \tag{19}$$

where τ_{max} is the maximum shear stress at midheight of the section

For the evaluation of τ_{max} it is assumed that the shear cracking is formed in the bed joints instead of the head, since the bed joints have lower compressive stresses.

Therefore:

$$\tau_{max} = c_p + \mu_p \gamma_o \sigma_{pier} \quad (20)$$

γ_o σ_{pier} the vertical stress on the bed joint at the spandrel axis

Finally the peak shear strength is calculated derived from the peak strength of the bed joints:

$$V_{p,s1} = \frac{2}{3}\left(c_p + \mu_p p_{sp}\right) d_s t_s \quad (21)$$

If shear failure causes cracking through the bricks, the peak shear strength of the spandrel can be estimated similar to the shear strength of piers (Magenes and Calvi 1997):

$$V_{p,2} = d_s t_s \frac{f'_{bt}}{2.3(1+a_v)} \sqrt{1 + \frac{p_{sp}}{f'_{bt}}} \quad (22)$$

f'_{bt} is the direct tensile strength of the bricks and a_v the shear ratio of the spandrel, which is approximately $a_v = b_s/2d_s$.

As far as the residual shear strength is concerned, it is assumed that the masonry spandrel on its own, i.e., neglecting the contribution of a timber lintel or masonry arch, does not develope a reliable residual strength capacity after shear cracking, therefore this strength is neglected.

Contribution of timber lintel

The timber lintel is assumed to be supported over a length s_l in the adjacent piers. Its contribution to the peak flexural and shear strength is neglected due to its flexibility, nevertheless it is significantly contributes to the residual strength of the spandrel for both flexural and shear failure.

Regarding the flexural failure the cohesive strength of the lintel support can contribute to the residual strength with the tension force estimated as

$$T = c_p t_s s_l \quad (23)$$

The equation for the residual flexural strength is finally:

$$V_{r,flo} = \left(P_{sp}(d_s - h_c) + T\left(d_s + h_l - \frac{h_c}{2}\right)\right)\frac{1}{b_s} \quad (24)$$

where h_l is the height of the timber lintel. The compression zone depth hc can be estimated assuming a constant compressive stress of 0.85fhm over the height of the compression zone:

$$h_c = \frac{P_{sp} + \frac{T}{2}}{0.85 f_{hm} t_s} \quad (25)$$

The residual shear strength, assuming that the timber lintel is simply supported at one end, fixed at the other and loaded by a point load at midspan, can be calculated by the following equation:

$$V_{r,s} = \frac{11}{16} P_{sp} \frac{d_s}{b_s} \quad (26)$$

2.5 Conclusions

The research that was performed regarding the state of the art led to some valuable conclusions about the selection of the appropriate strategy for the current study.

First of all the evaluation of the spandrel strength in masonry façades is a very interesting and important topic concerning the estimation of the in plane capacity of masonry façades. Several experiments have been performed the last years about this topic, the amount of different material type and patterns though, is not yet allowing the adequate understanding of this problem. Further investigation should be performed with the assistance of structural analysis techniques. Taking into account the review about the different structural analysis approaches that are available, the FE macromodelling approach proved to be the most appropriate in terms of accuracy and computational cost. Another modeling approach worth investigated is the micromodelling approach, since it has proved to obtain more explicit results. Due to the complexity of these techniques and the requirement of several material properties as an input, their calibration based on appropriate benchmark problems is considered necessary. Finally another important aspect is their application with both academic and commercial software in order to be reliable but also applicable in engineering practice.

3. MACROMODELLING APPROACH

3.1 Introduction

In order to investigate the in plane behavior of masonry facades and especially the strength of spandrels, the macromodelling finite element method was selected. Based on the conclusions that were made by extended investigation on the state of the art, the macromodelling technique revealed as the most appropriate. The method is more explicit than the simplified and equivalent frame one, providing an adequate representation of both capacity and failure mode. Furthermore it requires less computational cost than micromodelling as well as a smaller number of mechanical parameters as an input. Therefore the calibration of unknown parameters such as fracture energy is easier. The numerical model that is going to be presented in the following section was created by the commercial Finite Element software DIANA. The development of this macromodel, using a benchmark problem, and its further application to a new case, are the core of this thesis. Nevertheless, giving the academic aim of this dissertation, a micromodel has been also developed as an appendix to the main work and is explained in chapter 4.

3.2 Experimental campaign at University of Naples

Augenti et al. (2011) investigated, through an experimental-numerical campaign the in plane behavior of masonry spandrels. This experiment was used as a benchmark problem in the context of this thesis, in order to calibrate the numerical model, which was described above. A detailed description of the experimental case is presented in the sections below.

3.2.1 Geometry

A full-scale portal frame specimen made of double-leaf tuff masonry was constructed in order to evaluate the behavior of masonry spandrels. It consisted of two URM piers connected by a spandrel panel resting on a wooden lintel with bond length of 150 mm at both sides. The global dimensions of the specimen were 5.10 m long, 3.62 m high and 0.31 m thick and are illustrated in detail in Figure 33. This specimen configuration is not statically determined and it is not easy to determine the reaction forces acting in the spandrel, but it is a realistic approximation of a real portal frame. This is happening due to the presence of whole piers which are absorbing energy due to the loading cycles, as it is happening in real structures. Also this geometry is simulating the modification of the boundary condition between piers and spandrels during the loading process.

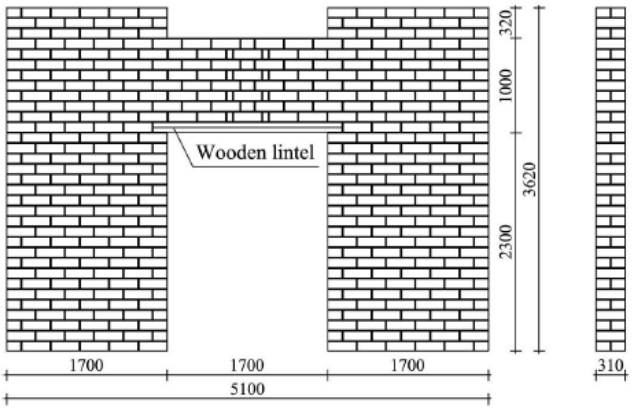

Figure 33. Geometry of tested specimen. (Augenti et al. 2011)

3.2.2 Material properties

The masonry specimen was constructed with yellow tuff stones (150 × 300 × 100 mm in size) from a quarry near Naples, Italy, and a hydraulic mortar composed of natural sand and pozzolan alike reactive aggregates with a water-sand ratio by weight of 1:6:25. Tuff stones were characterized by uniaxial compression tests on cubic specimens with edge length of 70 mm, whereas mortar was characterized through similar tests on specimens with dimensions 40 × 40 × 160 mm (Table 3).

Table 3. Tuff units, mortar mechanical properties.

Material	Tensile strength f_t (MPa)	Compressive strength f_c (MPa)	Young' s modulus E (Gpa)	Shear modulus G (MPa)
Yellow tuff units	0.23	4.13	1.54	0.44
Pozzolana-like mortar	1.43	2.5	1.52	0.66

Augenti & Parisi (2010) estimated mechanical properties of the entire tuff masonry (assumed as a unique “equivalent homogeneous material”) through two series of uniaxial compression tests along the directions parallel and orthogonal to the mortar bed joints of prisms (610 × 650 × 150 mm in size). The tuff units used for masonry prisms had the same dimensions of those employed for the tested wall and were bonded to one another through pozzolana-like mortar joints with a thickness of 10 mm. The instrumentation and the testing procedure used for masonry prisms were in compliance with American standards. The tensile strength was defined by diagonal compression tests, executed in specimens 310 × 1230 × 1230 mm^3 in dimensions (Parisi et al. 2013). The cohesion and the friction angle between mortar and unit were derived by triplet tests (Augenti and Parisi 2011). The mechanical properties derived from those tests are presented in Table 4 and Table 5.

Table 4. Mechanical properties of tuff-stone masonry. Compression tests

Test	Compressive strength	Young' s modulus	Shear modulus	Poisson ratio
	fc (MPa)	E (Gpa)	G (MPa)	v
Compression ⊥ to bed joints	3.96	2.159	854	0.27
Compression // to bed joints	3.85	2.016	777	0.35

Table 5. Mechanical properties of tuff-stone masonry. Diagonal compression and triplet tests.

Tensile strength	friction angle	cohesion
ft (MPa)	φ	c
0.15	0.279	0.146

3.2.3 Test set-up

The specimen was rigidly connected to the laboratory strong floor. For this purpose RC beams with dimensions 1700 × 310 × 200 mm were realized below the piers and were cast to Ω-shaped steel plates. The latter were in turn bolted to squared holes of the laboratory floor slab (Figure 34).

Vertical loads were applied in the piers with two transverse steel frames located at the centerlines of the masonry piers, simulating gravity loads applied to a real structure portal frame from the above floors. Bidirectional hydraulic jacks with maximum capacity of 500 kN were placed over rigid steel beams and were put in contrast with the cap beams of the transverse frames. The rigid steel beams placed over the piers of the specimen were employed to get rather uniform distribution of normal stresses throughout cross sections of the piers. Two Teflon polytetrafluoroethylene (PTFE) layers were placed between the jacks and the rigid steel beams to avoid any frictional resisting force at the interface.

“The lateral loading was applied through a horizontal servocontrolled hydraulic actuator (maximum capacity of 500 kN and stroke of +-250 mm) bolted to a nonprismatic reaction wall having a lateral load-carrying capacity of 250 kN and a corresponding horizontal displacement equal to 0.77 mm. The other end of the horizontal actuator was pinned at a perforated steel plate, which in turn, for cyclic tests only, allowed to employ six steel bars (18-mm diameter) aimed at applying force at the opposite end of the specimen. These bars ran along the wall spandrel at both sides of the wall. Finally, three steel beams were bolted to the columns of the transverse frames at both sides of the masonry wall to prevent potential out-of-plane failure modes.”

Regarding the loading protocol, a constant vertical load of 200 kN was applied to each pier. The lateral force was applied to the spandrels with an increased displacement at a constant rate of 0.01 mm/s up

to a displacement reading at the actuator of 28 mm (corresponding to an interstory drift ratio, θ, of approximately 1%). After the monotonic test, researchers applied cyclic loading, and also repaired and strengthen the specimen to perform a new test. In the aim of using it as a benchmark problem, the monotonic case has been selected.

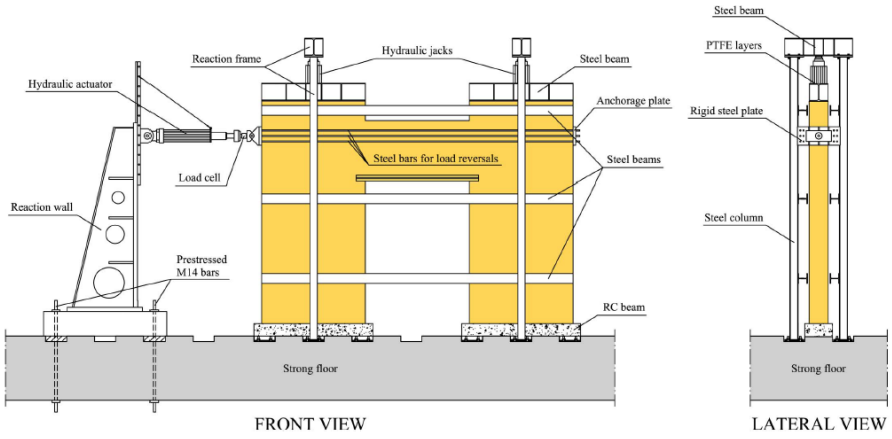

Figure 34. Experimental set-up of the University of Naples experiment. (Augenti et al. 2011)

3.2.4 Results

Damage pattern

The crack pattern of the specimen is illustrated in Figure 35. During the lower loading values flexural rocking cracks were observed at the base of both piers (Figure 35a). After that vertical flexural cracks occurred at the end sections and the middle of the spandrel panel (Figure 35b). As the displacement increased, the pier cracks become more evident and a diagonal shear cracking took place in the spandrel (Figure 35b). It is also important to point out that the horizontal loading stopped before the specimen collapsed, in order to get repaired and used again as a specimen. That means that the specimen studied here didn't reach its maximum capacity, although the maximum load capacity and an important part of its post peak behavior was obtained.

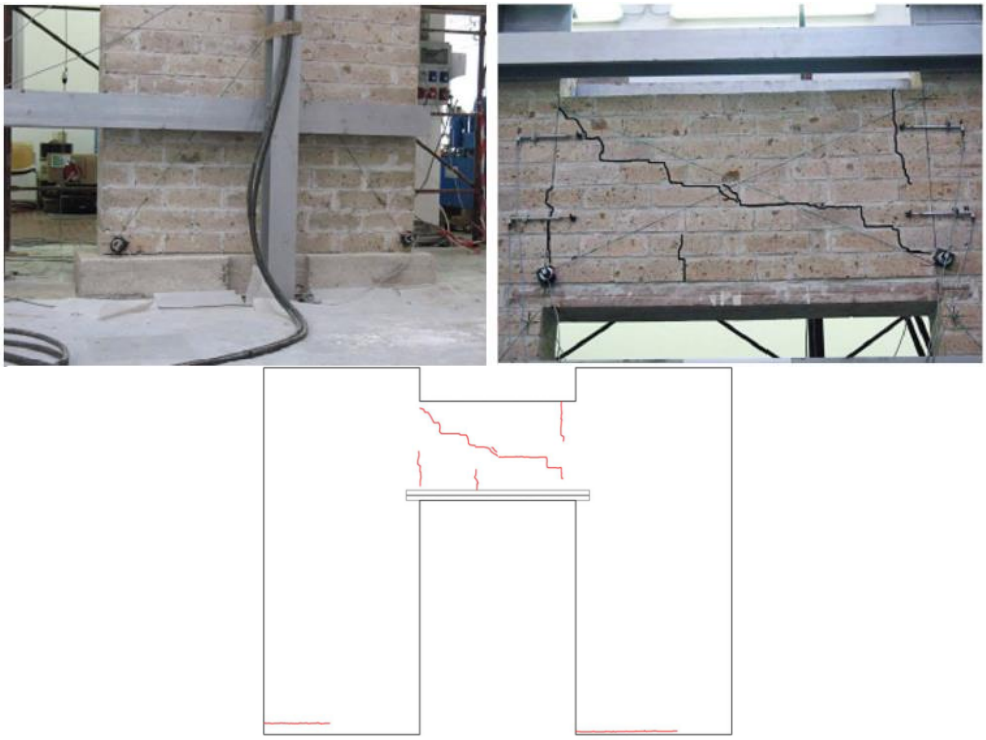

Figure 35. Cracking pattern a) at the base of the piers and b) at the spandrel panel and (c) complete crack pattern. (Augenti et al. 2011)

Force displacement curve

The experimental force-displacement curve is illustrated in Figure 36. Until a lateral displacement of approximately 3 mm the structure has an elastic behavior. After that the flexural cracks has formed at the piers bases and spandrel, resulting in a decreased stiffness. The frame specimen is reaching its peak strength of 184 kN at a displacement of 19.74 mm when the shear cracking in the spandrel is forming. The reaching of the peak strength is followed by an instant drop of strength of about 15% in terms of lateral strength. Then the lateral force capacity is increasing again reaching the value of 172 kN for the displacement of 27.18 mm, when the loading process stopped.

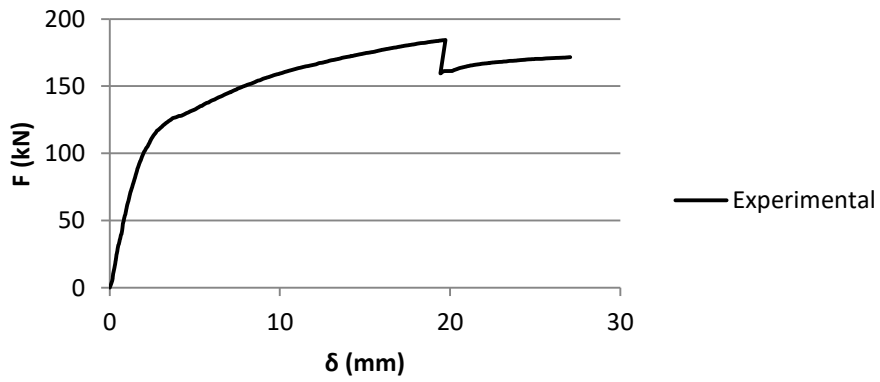

Figure 36. Force-displacement curve obtained by the experimental results. (Augenti et al. 2011)

3.2.5 Previous numerical approaches

In order to validate the numerical model developed in this thesis it was considered useful its comparison, not only with the experimental case, but also its comparison with cases which have considered the same benchmark problem. Those cases, which used a variety of modeling strategies and tools, are presented in detail bellow.

3.2.5.1 Parisi et al. (2011) model

Parisi et al. (2011) used a Finite Element numerical approach to further investigate the nonlinear in-plane response of masonry walls with openings, which was calibrated with the experiment described above. For the creation of the model, a micromodelling FE approach was created with the commercial DIANA FEA software, so that tuff stones and mortar joints were separately defined as isotropic continuum elements without frictional interfaces between them, according to a smeared-crack approach.

Both masonry units and mortar joints were meshed into CQ16M shell elements, whose total number was 41,065 (Figure 37). A CQ16M element is an eight-node quadrilateral isoparametric plane stress element. It is based on quadratic interpolation and Gauss integration. Typically, a quadrilateral element approximates strain and stress distributions over the element surface. The strain, εij, varies linearly in the i-direction and quadratically in the j-direction. The shear strain, γij, varies quadratically in both the i- and j-directions.

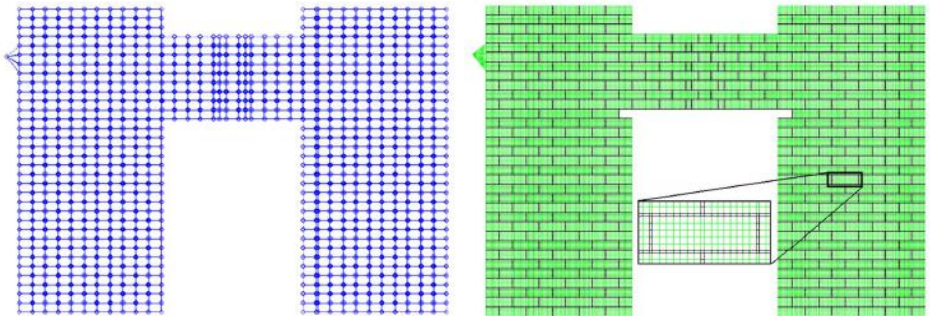

Figure 37. Finite element model and mesh of the subassemblage.

Vertical loads on the piers were applied with a uniform pressure to provide 200 kN axial forces for each pier. This is not exactly representing the actual punctual load applied in the physic tests by means of cylindrical jacks. Lateral loading on the subassemblage was applied, as an imposed displacement, and related pressure were distributed with a rigid device modeled by CT12M elements. A CT12M element is a six-node triangular isoparametric plane stress element.

The mechanical behavior of both tuff stones and mortar in the elastic range was defined by means of Young's and shear moduli (see Table 3). The used material model was a multidirectional fixed crack model (i.e., Rankine-type yield criterion) for tension with a plasticity model (i.e., Von Mises yield

criterion) for compression based on exponential softening in tension and parabolic softening in compression (Figure 38. FEM nonlinear material models for tuff stones and mortar.).

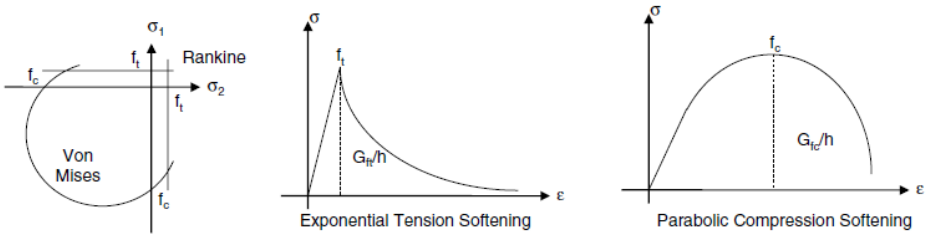

Figure 38. FEM nonlinear material models for tuff stones and mortar.

According to the authors all sensitivity analyses showed a negligible influence of the wooden lintel above the opening and some stress concentrations at the masonry-wood interface, so the lintel was not included in the final numerical model. However, these conclusions are not supported by evidences in the published paper. As it will be seen later with the analyses developed for this dissertation, the presence of the lintel does actually influence numerically; this fact is consistent with the experimental evidences shown by Graziotti et al. (2014) and reported in section 2.4.2 of this document. The numerical model was calibrated for tensile and compressive fracture energies. Tensile fracture energy was set to $1 \cdot 10^3$ and $4 \cdot 10^3$ Nmm/mm^2 for the tuff stones and mortar, respectively, whereas the compressive fracture energy was assumed to be 2 and 0.08 Nmm/mm^2, respectively. The energy values for the tuff stones in compression and the mortar in tension were derived from experimental tests, whereas the tensile fracture energy of the tuff stones was derived from tests performed by Asprone et al. (2009), and the compressive fracture energy of the mortar was determined by calibrating the FE model.

The cracking pattern of the numerical model is presented in Figure 39. As it is observed the micromodelling approach simulated adequately the cracking pattern, managing to obtain flexural cracking at the base of the piers and the end of the spandrel section, as well as the shear crack in the spandrel panel. Those cracks were smeared according to the adopted numerical modeling strategy. This cracking pattern does not aim to represent effective discrete cracks; it highlights the surfaces where cracking strains occur numerically over the continuous medium. Actual cracks would open along few discrete lines (strain localization) because the effective width is the integral of the cracking strain over the marked surfaces.

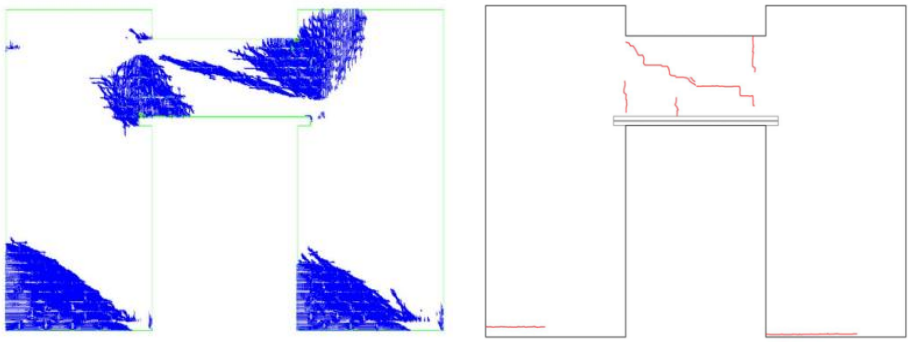

Figure 39. Comparison between numerical and experimental cracking pattern.

The force-displacement diagram obtained by the numerical solution is compared with the experimental one in Figure 40. The numerical model managed to obtain the maximum load capacity of the specimen (186 kN versus 184 kN in the experiment) as well as the same elastic stiffness. Regarding the post-peak behavior of the model, the numerical approach did not manage to simulate the exact behavior of the structure, which included a hardening behavior until the maximum displacement of 28mm.

Finally it has to be pointed out that the test stopped before the specimen collapse, therefore an estimation of the collapse mechanism or the maximum displacement capacity of the structure is not possible. Nevertheless valuable conclusions were made by this numerical investigation about the nonlinear behavior of masonry walls with openings.

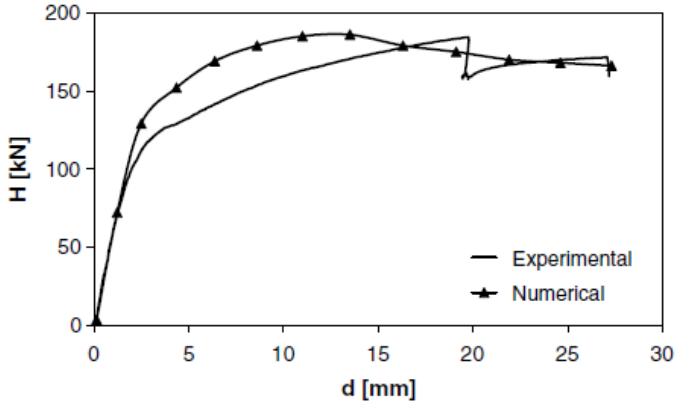

Figure 40. Comparison between numerical and experimental force-displacement curve.

3.2.5.2 Saloustros et al. (2016) model

Saloustros et al. (2016) applied a macromodelling approach in order to evaluate the efficiency of a crack-tracking algorithm in the modeling of quasi brittle materials, such as concrete and masonry. As a

benchmark problem, the same experimental case of the University of Naples (Augenti et al. 2010) was used.

The macromodelling Finite Element model was created with the software COMET, created at the Technical University of Catalonia. Constitutive model based on the continuum damage mechanics presented in Cervera et al. (1995) is used for the simulation of fracture. The model benefits from the use of two separate damage scalar indexes to distinguish between tensile and compressive damage. This is an important characteristic for the simulation of degradation in materials such as concrete and masonry which have quite different capacity under tension and compression. The continuum damage model is presented in Figure 41.

The aim of this work was to apply the know-how of objective mesh-localization approaches to the analysis of structures made of quasi-brittle materials that experience multiple cracking. The adopted numerical technique is the classical smeared crack approach enhanced with a local crack-tracking algorithm

Most of currently available crack-tracking algorithms focus on the simulation of cracks starting from the boundary of the discretized domain and propagating towards a single orientation. This drawback limits the application of such algorithms, which cannot be used for the analysis of structures experiencing internal cracking such as shear cracks. To overcome this limitation, in this work the local-crack tracking algorithm presented by Cervera et al. (2010) is adequately enhanced for the simulation of cracking initiating from internal elements of the mesh and propagating along two opposite orientations. This section presents the main features of the algorithm focusing on its novel contributions.

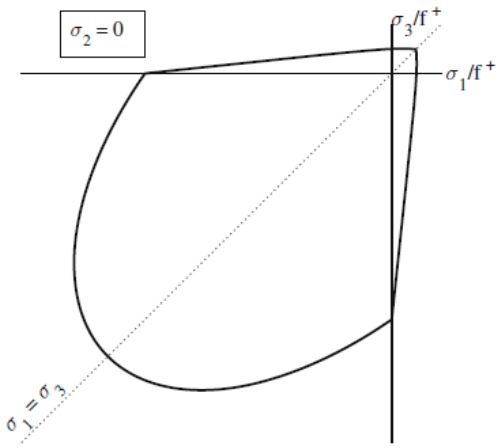

Figure 41. Adopted damage surface under plane-stress conditions. (Saloustros et al. 2016)

Regarding the numerical model the masonry frame is discretized in an unstructured mesh of 2D plane-stress three-noded triangles with average mesh size of *he* = 4 cm (10678 nodes) (Figure 42). The masonry was modeled with the properties presented in Table 6. Linear elastic behaviour was

assumed for the timber lintel with Young's modulus of E=15 GPa. In order to simulate better the interaction between timber lintel and masonry, a mortar of 10 mm thickness was created at their interface with negligible tensile strength and reduced stiffness (Table 7). This allowed the appropriate separation of the lintel on its left end and the correct coupling between the right end and the pier.

.

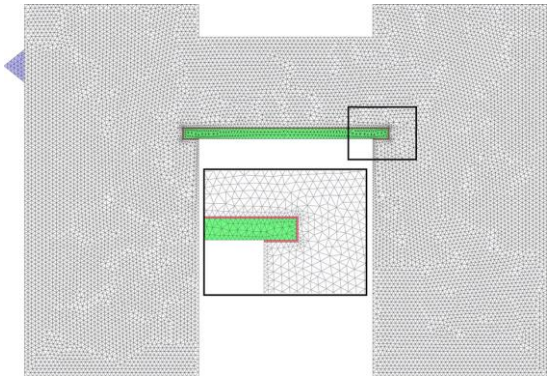

Figure 42. Discretized domain used for the numerical simulation. (Saloustros et al. 2016)

Table 6. Material properties selected for masonry.

E	f^+	f^-	v	ρ	G^+	G^-	f_b^-/f^-
GPa	MPa	MPa	-	kg/m^3	J/m^2	J/m^2	-
1.54	0.13	3.9	0.2	1200	15	35000	1.15

Table 7. Material properties selected for interface mortar.

E	f^+	f^-	v	G^+	G^-
GPa	MPa	MPa	-	J/m^2	J/m^2
0.02	0.01	3.9	0.2	5	35000

The resulting cracking pattern of this numerical approach is presented in Figure 43. The final cracking pattern is a satisfying approximation of the experimental cracks. Also the sequence of the crack propagation that is presented in Figure 43 is a good approximation of the experimental one that was described in section 3.2.4.

Regarding the numerical model capacity, the comparison between numerical approach and experimental force-displacement curve is presented in Figure 44. It is observed a very good approximation of the experiment behavior. More specifically the numerical model is able to estimate the maximum horizontal load capacity with great accuracy. The model has an increasing load capacity until the peak load, followed by an instant drop of strength and finally a hardening behavior until the maximum displacement, which is also in good correspondence with the specimen behavior. The same

authors replied the analyses without the enhancement, obtaining a more diffused crack pattern and decreased strength. Their results and the one of Parisi et al. are shown in (Figure 44).

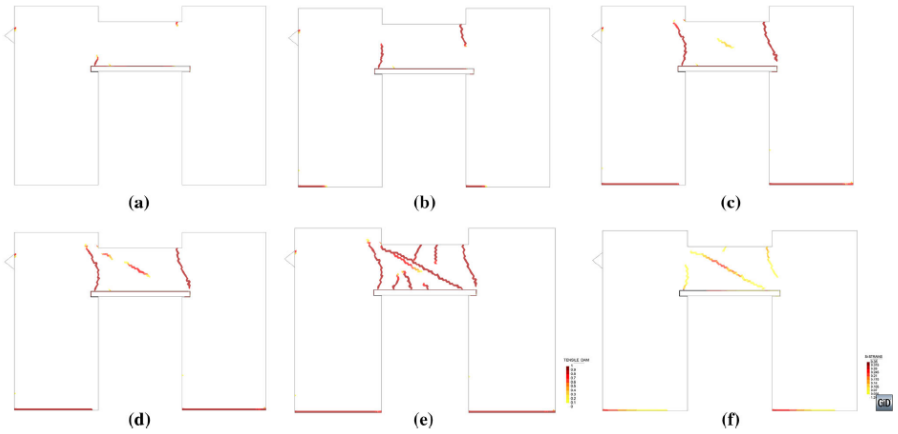

Figure 43. Tensile damage contour for: a d=15 mm, b d=3.3 mm, c d=12.3 mm, d d=17.3 mm, e d=20.7 mm, f. Maximum principal contour for d=20.7 mm (Saloustros et al. 2016)

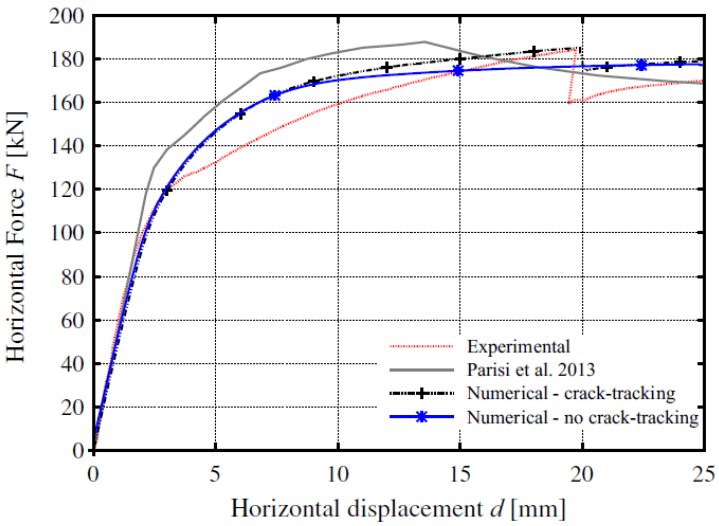

Figure 44. Load-displacement graph of the experimental test and the numerical analyses (Saloustros et al. 2016)

3.2.5.3 Salvatoni & Ugolini (2016)

Prior to this dissertation, two students from Polytechnical University of Milano developed at UPC another numerical model of the same benchamrk problema using the comercial software DIANA FEA. The experimental specimen that was described in the previous sections was modeled with the macromodelling approach, using CT12M shell elements. CT12M element is a six-node triangular isoparametric plane stress element. Vertical loads on the piers were applied with a uniform pressure to provide 200 kN axial forces for each pier. The horizontal loading was applied as an increasing displacement.

The used material model was a total strain based crack model (i.e., Rankine-type yield criterion) for tension with a plasticity model (i.e., Von Mises yield criterion) for compression based on exponential softening in tension and parabolic softening in compression. Also the multidirectional fixed crack model was used, but provided less satisfying results than the total strain model. The mechanical properties that were decided after calibration of the model are illustrated in Table 8.

Table 8. Mechanical properties used for the numerical model.

E	fc	ft	v	ρ	Gc	Gf
GPa	MPa	MPa	-	kg/m^3	J/m^2	J/m^2
1.54	3.96	0.079	0.2	1800	6336	2.3

The cracking pattern of the model is illustrated in Figure 45. The comparison between the cracks obtained in the numerical model and the experimental specimen is giving a good approximation, regarding the cracking pattern in the spandrel panel. By contrast in the piers the cracks are not corresponding to the experimental case, since diagonal cracks are obtained at the base of the piers, as well as the shear crushing of the right pier, which were not detected during the real experiment..

Regarding the force displacement diagram (Figure 46), the numerical model approximated the solution of Parisi micromodel (Parisi et al. 2011), but without managing to obtain a good approximation of the experimental behavior. More specifically, although the maximum capacity was exactly the same as the experimental, the maximum load was obtained for a displacement lower than the experimental. More important, the post peak behavior was characterized by a descending branch, with the experimental having a hardening behavior.

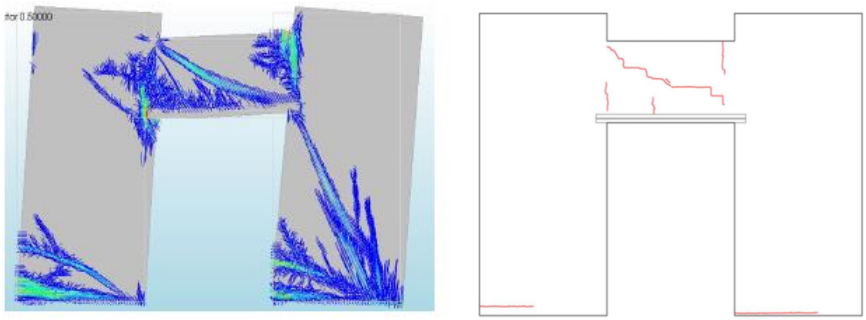

Figure 45. Comparison between numerical and experimental cracking pattern in the research of Salvatoni & Ugolini (2016).

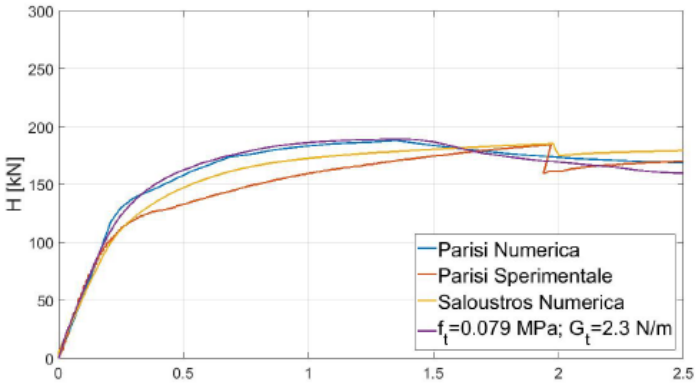

Figure 46. Force-displacement curve of the numerical model. Salvatoni & Ugolini (2016)

3.3 Development of the model

3.3.1 Model characteristics

As it was explained in section 3.1 the numerical approach that was decided to be used for the investigation of the spandrel behavior in masonry façades, is the macromodeling Finite Element method, using the FE software DIANA FEA for its interpretation. A detailed description of the model and its input data is given in the following sections.

3.3.1.1 Geometry

The geometry of the numerical model is presented in Figure 47. The geometry of the masonry specimen and the timber lintel was identical with the specimen's. Additional elements were added to the model in order to represent better the loading procedure. Rectangular elements were added on the top of each pier, in order to simulate the steel beams that were placed between the actuator and the masonry piers. This simulation was selected in order to represent more realistically the distribution of the vertical forces. A vertical force of 200 kN was applied at the top of those elements. Finally a triangular element with steel properties and zero gravity was created at the position of the horizontal loading actuator. A horizontal displacement of 0.028 m was applied on the left corner of the element. The selection of this method to apply the horizontal load was decided in order to allow the quantity of masonry where the horizontal displacement is applied to rotate with the rest of the masonry component and avoid undesirable distribution of stresses in the loading area.

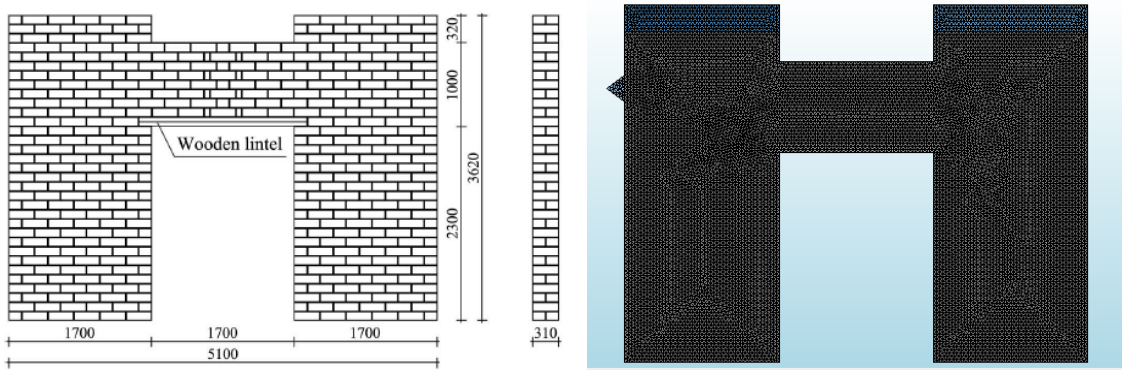

Figure 47. Numerical model geometry

3.3.1.2 Mesh type

The same type of mesh was used to simulate the masonry specimen, as well as the steel beams and the actuator triangular element. This type of mesh is called T6MEM (Figure 48). It is a three-node triangular isoparametric plane stress element. It is based on linear interpolation and area integration. The polynomial for the displacements ux and uy can be expressed as:

$$u_i(\xi,\eta) = \alpha_0 + \alpha_1\xi + \alpha_2\eta \quad (27)$$

The selection of plane stress elements was done, in order to exclude out of plane bending of the specimen, which would not represent the observed behavior during the loading process.

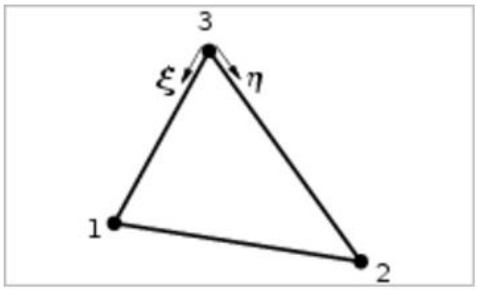

Figure 48. T6MEM element. (DIANA FEA 2016)

3.3.1.3 Material type

The constitutive model used for the numerical model was the total strain based crack model that DIANA FEA provides for Concrete and Masonry materials.

Loading and unloading determination

During loading the material is subjected to both tensile and compressive stress which can result in cracking and crushing of the material. In a fixed stress–strain concept the shear behaviour is modeled explicitly with a relation between the shear stress and the shear strain. The deterioration of the material due to cracking and crushing is monitored with six internal damage variables α_k, collected in the vector α. The internal variables *k = 1,...,n* monitoring the maximum strain and it is taking values greater or equal to zero. The internal variables *k = n +1,...,2×n* monitoring minimum strain and it is taking values smaller or equal to zero (Figure 49) (*n* is the number of strain components). It is assumed that damage recovery is not possible which implies that the absolute values of the internal damage variables are increasing. (DIANA FEA 2016)

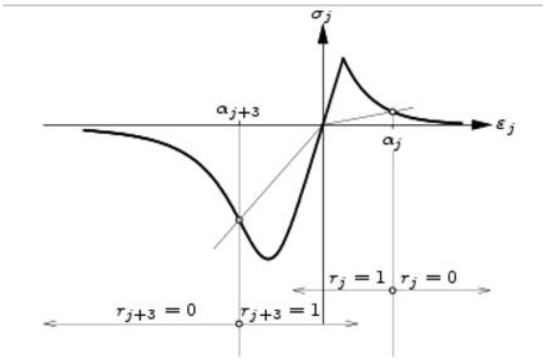

Figure 49. Loading-unloading. (DIANA FEA 2016)

The loading–unloading–reloading condition is monitored with the additional unloading constraints r_k which are determined for both tension and compression to model the stiffness degradation in tension and compression separately. In tension the unloading constraints are given by

$$r_k = \begin{cases} 0 & if \quad {}^{t+\Delta t}_{i+1}\varepsilon_k > \alpha_k \\ 1 & if \quad {}^{t+\Delta t}_{i+1}\varepsilon_k \leq \alpha_k \end{cases} \qquad k = 1, \dots, n \tag{28}$$

and in compression by

$$r_k = \begin{cases} 0 & if \quad {}^{t+\Delta t}_{i+1}\varepsilon_{k-3} > \alpha_k \\ 1 & if \quad {}^{t+\Delta t}_{i+1}\varepsilon_{k-3} \leq \alpha_k \end{cases} \quad k = n+1, \dots, 2xn \tag{29}$$

The update of the internal variables can be expressed as

$${}^{t+\Delta t}_{i+1}\alpha = {}^{t}\alpha + W\Delta\varepsilon \tag{30}$$

with the matrix *W* given by

$$W = \begin{cases} W_{k.k} = 1 - r_k & k = 1, \dots, n \\ W_{k,k-n} = 1 - r_k & k = n+1, \dots, 2xn \end{cases} \tag{31}$$

With the assumption of no damage recovery, the stress in direction *j* is given by

$$\sigma_j = f_j(\alpha, \varepsilon_{nst}) \cdot g_j(\alpha, \varepsilon_{nst}) \tag{32}$$

The uniaxial stress–strain relation, $\boldsymbol{fj}$, is usually not only a function of the internal variable $\boldsymbol{\alpha j}$, but also a function of the internal variables in the other directions and the strain in the other directions, therefore ($\boldsymbol{\alpha}$,$\boldsymbol{\varepsilon}$). If unloading and reloading is modelled with a secant approach, determined by the maximum and minimum strain in each crack direction, the loading-unloading function, denoted as *g* with $\mathbf{0} \leq \boldsymbol{g} \leq \mathbf{1}$, is given by

$$g_j = \begin{cases} 1 - \frac{\alpha_j - \varepsilon_j}{\alpha_j} & if\ \varepsilon_j > 0 \\ 1 - \frac{\alpha_{j+n} - \varepsilon_j}{\alpha_{j+n}} & if\ \varepsilon_j < 0 \end{cases} \tag{33}$$

The uniaxial stress–strain relation is based on the basic strength in the crack directions *f*, multiplied by the loading–unloading function *g*. In the material model which is developed in this project, the effect of confinement and the effect of lateral cracking are taken into account in the basic strength because not only the maximum strength is influenced, but in general also the shape of the stress–strain curve.

Tensile behavior

The tensile behaviour of masonry can be modelled using different approaches, one resulting in a more complex description than the other. For the Total Strain crack model, six softening functions based on fracture energy are implemented. (DIANA FEA 2016)

For the numerical model created for the purposes of this study, an exponential tensile behavior was selected (Figure 50). This function requires as an input the tensile strength of the material as well as the tensile fracture energy.

Figure 50. **Predefined tension softening for Total Strain crack model. (DIANA FEA 2016)**

Compressive behavior

A masonry material subjected to compressive stresses shows a pressure-dependent behaviour, i.e., the strength and ductility increase with increasing isotropic stress. Due to the lateral confinement, the compressive stress–strain relation is modified to incorporate the effects of the increased isotropic stress. Furthermore, it is assumed that the compressive behaviour is influenced by lateral cracking. To model the lateral confinement effect, the parameters of the compressive stress–strain function, f_{cf} and ε_p, are determined with a failure function which gives the compressive stress which causes failure as a function of the confining stresses in the lateral directions. (DIANA FEA 2016)

If the material is cracked in the lateral direction, the parameters are reduced with the factor $\beta_{\varepsilon cr}$ for the peak strain, and with the factor $\beta_{\sigma cr}$ for the peak stress. An overview of possible relations is given below. It is tacitly assumed that the base curve in compression is determined by the peak stress value $f_p = \beta_{\sigma cr} f_{cf}$, and the corresponding peak strain value $\alpha_p = \beta_{\varepsilon cr} \cdot \varepsilon_p$. In summary,

$$f_p = \beta_{\sigma cr} \cdot f_{cf} \tag{34}$$

$$\alpha_p = \beta_{\varepsilon cr} \cdot \varepsilon_p \tag{35}$$

The base function in compression, with the parameters f_p and α_p, is modelled with a number of different predefined and user-defined curves.

For the numerical model created for the purposes of this study, a parabolic compression behavior was selected (Figure 51).

The parabolic curve in DIANA is a formulation based on fracture energy, according to Feenstra 1993. The parabolic curve is described by three characteristic values (Figure 51).

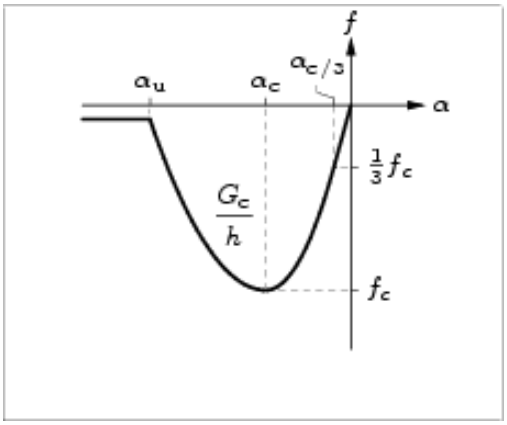

Figure 51. Parabolic compression curve. (DIANA FEA 2016)

3.3.1.4 Initial properties input

The material properties input for the Total Strain Based Crack Model was based in the experimental tests that were executed at the University of Naples for the characterization of the tuff stone masonry (section 3.2.2).

The mechanical properties of the numerical model are presented in Table 9. More specifically the values of Young's Modulus E, Poisson's ratio v, density ρ, compressive strength f_c and tensile strength f_t were derived from the experimental tests described in section 3.2.2

The values of E and f_t were modified during the calibration process in order to obtain the desired behavior of the numerical model.

As regards the tensile fracture energy, although there are recommendations and available equations to correlate tensile strength and tensile fracture energy (Lourenço 2008), a value for the tensile fracture energy of the masonry as a composite material is not possible. The factors that affect the bond between unit and mortar are highly dependent on the units (material, strength, perforation, size, air dried or pre-wetted, etc.), on the mortar (composition, water contents, etc.) and on workmanship (proper filling of the joints, vertical loading, etc.).

As it is mentioned in Lourenço (1996), a recommendation for the value of the bond tensile strength based on the unit type or mortar type is impossible. Nevertheless, an average value of the bond mode I fracture energy equal to 0.012 Nmm/mm2 can be, in principle, adopted. Due to the relatively low value of tensile strength used for the masonry component (0.15 N/mm^2), a slightly lower value of 10 Nmm/mm^2 was adopted. Nevertheless the value was updated during the adaptation of different values for the tensile strength.

Not much data exists about the post-peak behavior of masonry prisms. For an estimation of the compressive fracture energy, it is recommended to adopt the values proposed for concrete in the Model Code 90 (CEB-FIP 1993), to simulate anisotropic behavior.

For compressive strength less than 12 N/mm2 the Model Code 90 (CEB-FIP 1993) is proposing an average ductility $d_{u,c}$ equal to 1.6 mm. Therefore:

$$G_c = d_{u,c} f_c = 1.6\ mm \cdot 3.96\ N/mm^2 = 6443\ N/m \quad (36)$$

The rotating orientation that implemented was the rotating one with crack bandwidth specification based on the Rots model. The fixed crack orientation was also applied and its influence is discussed in following sections 3.3.2.4.

Table 9. Mechanical properties of the numerical model.

E	v	ρ	fc	Gc	ft	Gf
GPa	-	kg/m3	MPa	N/m	MPa	N/m
2.16	0.27	1200	3.96	6443	0.15	10

3.3.2 Numerical solution

The Finite Element method is a complex numerical method. In order to obtain a satisfying solution it is very important to specify parameters like the iteration method, the mesh size, the load step size, the crack orientation and the convergence criterion. An optimal option for all those parameters is not possible to be defined. Therefore they should be adjusted to every different analysis. The following section is justifying the selection of the numerical solution that was adopted.

3.3.2.1 Iteration method

A purely incremental method usually leads to inaccurate solutions in nonlinear analysis, unless very small step sizes are used. In an iterative process the errors that occur can be reduced successively. This in fact realizes an *implicit procedure.* The allowable step size is usually higher than in case of a process without iterations (e.g. an explicit process). The general procedure is the same for all iteration processes.

In all procedures, the total displacement increment Δu is adapted iteratively by iterative increments δu until equilibrium is reached, up to a prescribed tolerance. Indicating the iteration number with a right subscript, the incremental displacements at iteration *i* + 1 are calculated from

$$\Delta u_{i+1} = \Delta u_i + \delta u_{i+1} \quad (37)$$

The difference between several procedures is the way in which **δu** is determined. The iterative increments are calculated by use of a `stiffness matrix' **K** that represents some kind of linearized form

of the relation between the force vector and displacement vector. The used stiffness matrix can change every iteration, the matrix that is used in iteration *i* is called K_i . A direct approach is to determine the iterative increments by

$$\delta u_i = K_i^{-1} g_i \tag{38}$$

where g_i is the out-of-balance force vector at the start of iteration *i* . In this case a linear set of equations is solved at every iteration.

For the equilibrium iteration of the model the Regular Newton-Raphson method was selected. In the Regular Newton-Raphson iteration the stiffness relation (38) is evaluated at every iteration (Figure 52). This means that the prediction of (37) is based on the last known or predicted situation, even if this is not an equilibrium state.

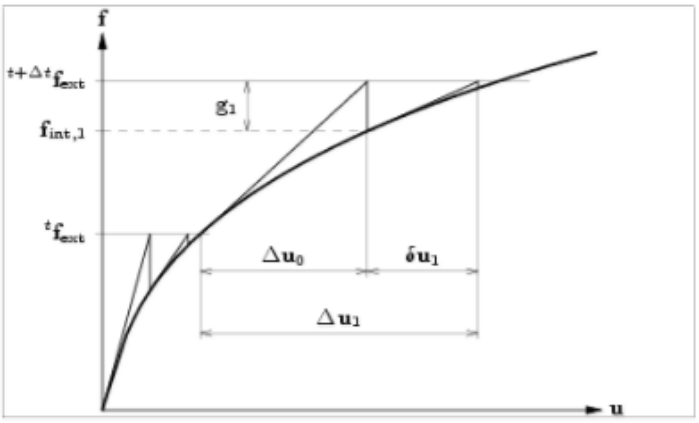

Figure 52. Regular Newton-Raphson iteration (DIANA FEA 2016)

The Regular Newton-Raphson method yields a quadratic convergence characteristic, which means that the method converges to the final solution within only a few iterations.

A disadvantage of the method is that the stiffness matrix has to be set up at every iteration and, if a direct solver is used to solve the linear set of equations, the time consuming decomposition of the matrix has to be performed every iteration as well. Moreover, the quadratic convergence is only guaranteed if a correct stiffness matrix is used and if the prediction is already in the neighborhood of the final solution. If the initial prediction is far from the final solution, the method easily fails because of divergence.

Finally the convergence norm was selected as displacement control, since the model's loading was applied as an imposed horizontal displacement, with convergence tolerance of 0.01.

3.3.2.2 Mesh size

The initial analyses were executed without the simulation of the timber lintel following the indications of Parisi et al. 2011 about the minor influence of the timber lintel to the overall behavior of the specimen.

Several analyses were executed in order to evaluate the proper mesh size.

The resulting force-displacement diagrams for mesh size of 10, 7.5 and 4 cm are presented in Figure 53. It is observed that the mesh size although it is not influencing the overall behavior, influences the convergence between numerical and experimental results. The mesh size of 4 cm gave a solution closer to the experimental one therefore it was selected as the optimal one for the rest of the thesis.

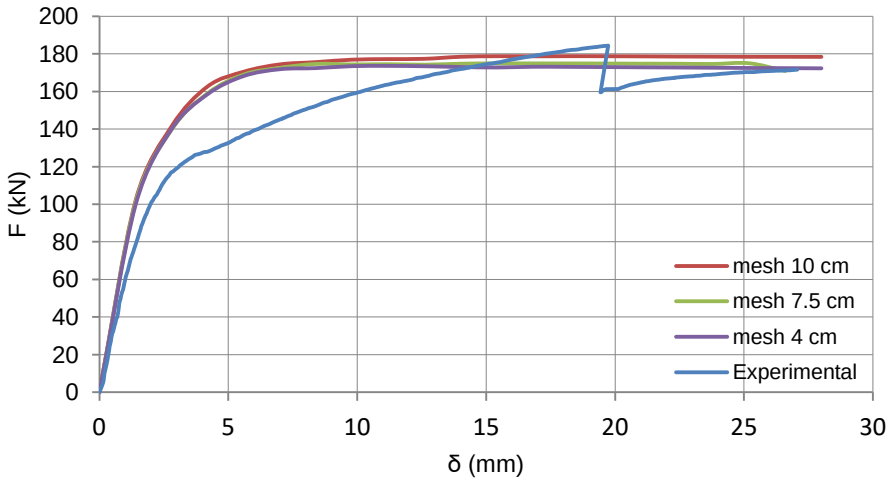

Figure 53. Mesh size influence

3.3.2.3 Step size

Another important parameter that is influencing a numerical model is the load step size. The maximum horizontal displacement imposed to the model was 2.8 cm as much as the experimental one. Since the maximum displacement was constant, a different step size resulted to a different number of steps

As it is observed in Figure 54 the decreasing of the displacement increment from 0.05 to 0.01 resulted a better approximation of the load-displacement curve. Nevertheless a further decrease of the step size to 0.005 did not change significantly the behavior of the model. Therefore a step size of 0.01 was considered suitable for the analysis, since a smaller step size would result to a higher computational cost without any important effect on the model accuracy.

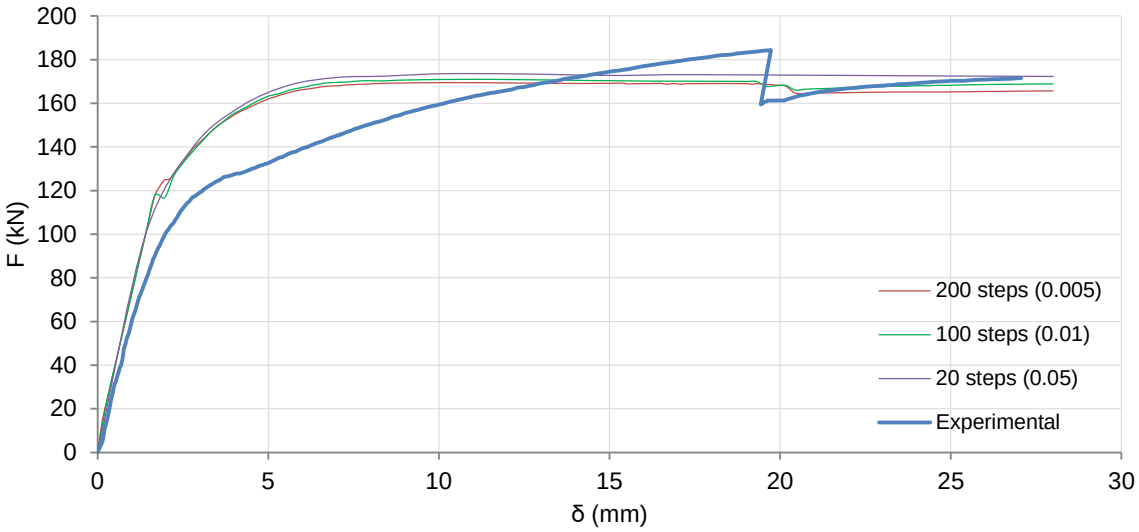

Figure 54. Step size influence

3.3.2.4 Crack orientation

The Total Strain Based Crack model provides two different methods for the specification of the crack orientation, fixed and rotating. (DIANA FEA 2016)

The basic concept of the Total Strain crack models is that the stress is evaluated in the directions which are given by the crack directions. The strain vector ε_{xyz} in the element coordinate system *xyz* is updated with the strain increment $\Delta\varepsilon_{xyz}$ according to

$$^{t+}\Delta^{t}_{i+1}\varepsilon_{xyz} = {}^{t}\varepsilon_{xyz} + {}^{t+}\Delta^{t}_{i+1}\Delta\varepsilon_{xyz} \tag{39}$$

which is transformed to the strain vector in the crack directions with the strain transformation matrix **T**,

$$^{t+}\Delta^{t}_{i+1}\varepsilon_{nst} = \mathbf{T}\ \ {}^{t+}\Delta^{t}_{i+1}\varepsilon_{xyz} \tag{40}$$

In a coaxial rotating concept the strain transformation matrix **T** depends on the current strain vector, i.e.,

$$\mathbf{T} = \mathbf{T}(\,{}^{t+}\Delta^{t}_{i+1}\varepsilon_{xyz}) \tag{41}$$

whereas in a fixed concept the strain transformation matrix is fixed upon cracking. The behaviour in compression is evaluated in a rotating coordinate system when the material is not cracked, where in case of a fixed concept the compressive behaviour is evaluated in the fixed coordinate system determined by the crack directions.

Another difference of those models is the shear behavior. In the fixed crack concept the shear stiffness is reduced after cracking. For the current implementation in DIANA, only a constant shear stiffness reduction is modeled, i.e.

$$G^{cr} = \beta G \quad (42)$$

with β the shear retention factor, $0 \leq \beta \leq 1$. For the rotating crack concept the shear retention factor can be assumed equal to one.

In order to evaluate the influence of those two concepts different analyses were executed with same mechanical properties (Table 10) and different crack orientation. For the fixed crack concept several values were given to the β factor.

The interface element used for those analyses was the uniform interface which is going to be described in section 3.4.3.2.

The results are presented in Figure 55 and Figure 56.

Table 10. Mechanical properties of the models.

E	v	ρ	fc	Gc	ft	Gf
GPa	-	kg/m^3	MPa	N/m	MPa	N/m
1500	0.27	1200	3.96	6336	0.15	10

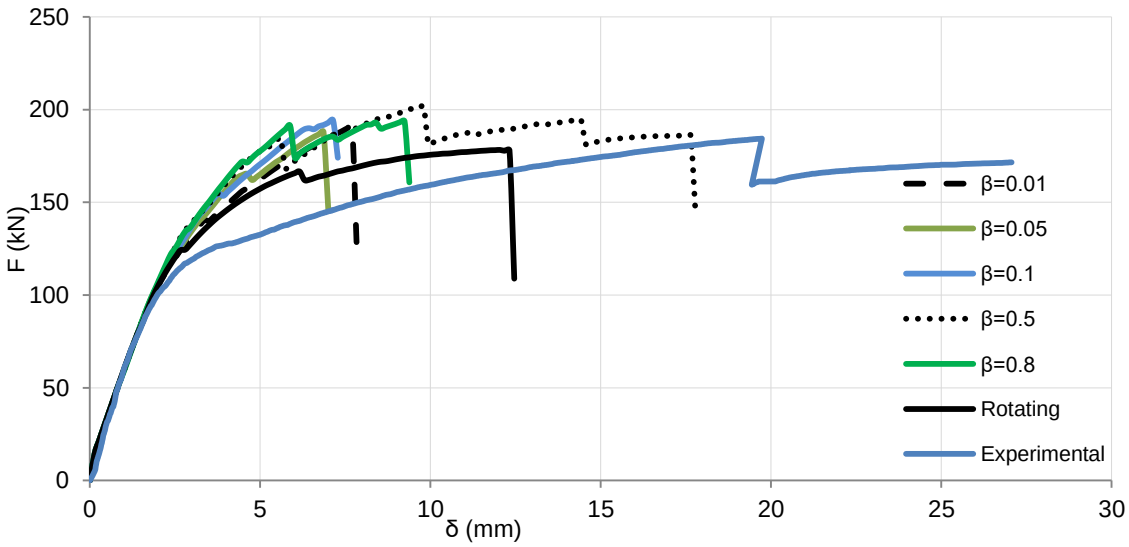

Figure 55. Load-displacement graph for different crack orientation concepts

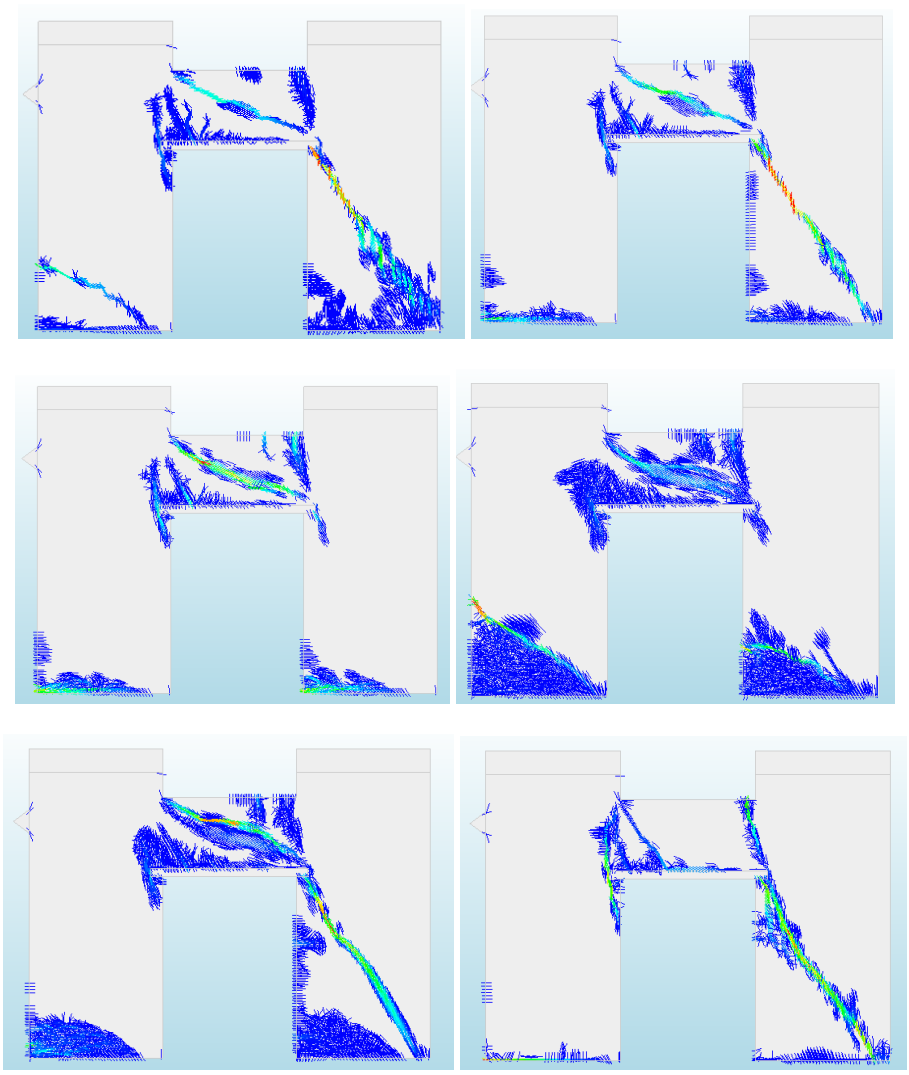

Figure 56. Damage contour for (a) β=0.01 (b) β=0.05 (c) β=0.1 (d) β=0.5 (e) β=0.8 (f) rotating crack orientation

The results are showing a negative influence of the fixed crack orientation to the numerical model's effectiveness. Although the fixed crack orientation is contributing to the obtaining of the diagonal crack in the spandrel panel, it is also affecting the behavior of the piers, creating shear cracks either to the base of each pier, either to the right pier. Even for the case of β=0.1 where the crack pattern is satisfying, the load-displacement graph overestimate the capacity of the structure.

By contrast the rotating crack orientation was the only one that managed to obtain a similar capacity to the experimental case. The most critical effect of this concept is that is managing to obtain linear flexural cracks in the base of the piers as in the experimental case. The diagonal cracks in the piers obtained by the implementation of the fixed crack concept are modifying the behavior of the model and provide an unrealistic representation of the actual behavior.

These observations led to the adoption of the rotating crack orientation, for the following analysis.

3.4 Parametric study

The finite element structural analysis of masonry requires a good knowledge of the masonry's behavior as well as the parameters that the adopted material models require. In order to evaluate the influence of several parameters of the Total Strain Based Crack Model and their influence to the non-linear response of the numerical model, several analyses were performed with a variety of different values for the mechanical parameters. The results from those analysis as well as the conclusions that were derived from them are presented in the following sections.

Another part of this parametric study that is going to be discussed in the following sections is the simulation of the timber lintel and the influence of the interface between lintel and masonry.

3.4.1 Influence of tensile strength

In the Total Strain Based Crack model a Raknine plasticity model is adopted, meaning that the damage is affected mainly by the tensile strength. Therefore the understanding of the tensile strength's influence was considered essential for the proper simulation of the numerical approach. In addition the tensile strength values obtained by the experimental tests (Parisi et al. 2013) showed a large dispersion, therefore a modification of this value was considered necessary.

The other mechanical properties of the masonry component as well as the interface element are presented in Table 11, Table 12.

Table 11 Mechanical properties of masonry component

E	v	ρ	f_c	G_c	f_t	G_f
GPa	-	kg/m^3	MPa	N/m	MPa	N/m
1500	0.27	1200	3.96	6336	0.15	10

Table 12 Mechanical properties of interface between masonry and timber

k_n	k_t	c	φ	ψ
N/m^3	N/m^3	N/m^2	rad	rad
1.17E+13	1.36E+11	0.146	0.279	0.01

The results of these analyses are presented in Figure 57 and Figure 58. It is observed a strong relation between the value of the tensile strength and the propagation of the diagonal crack in the spandrel panel. Lower values of tensile strength make easier the creation of this crack. For higher

values the shear present only flexural cracks resulting to an increasing concentration of stresses in the piers.

Another important aspect is the influence on the load displacement graph. Although the tensile strength is not affecting the maximum capacity of the model, it is affecting the value of horizontal displacement for which the spandrel fails in shear. More specifically the spandrel failure can be found in the point of the graph where an instant drop of load is observed. It can be concluded that increasing values of tensile strength resulted to the failure of the spandrel for higher horizontal displacement. This conclusion was very valuable for the selection of the final value of tensile strength for the final calibrated model.

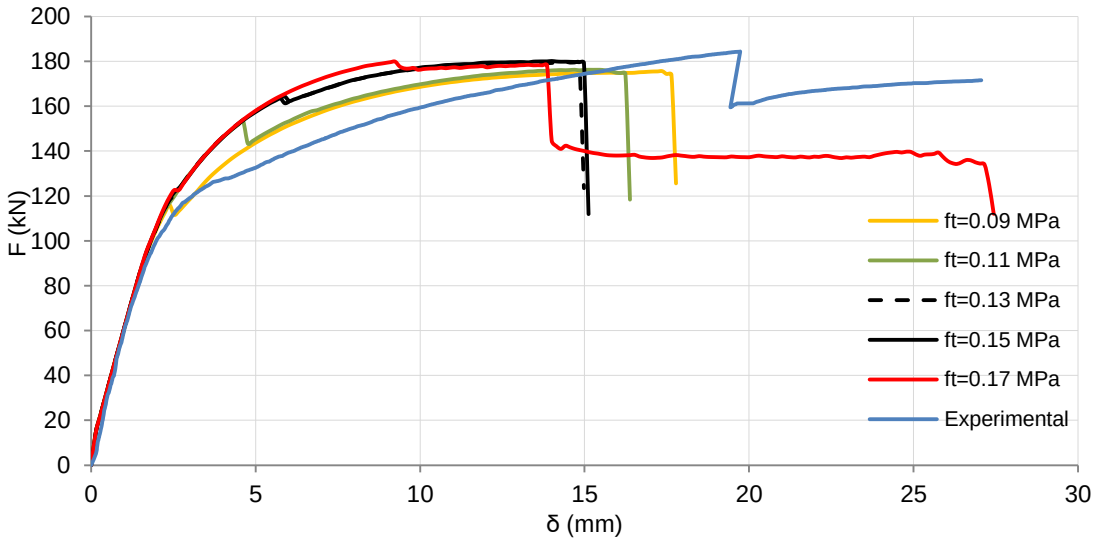

Figure 57. Load-displacement graph for different values of tensile strength

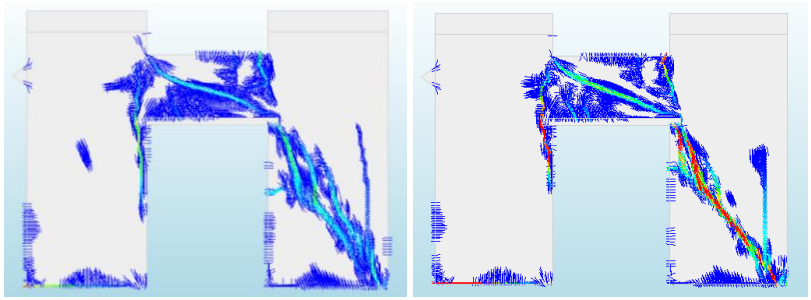

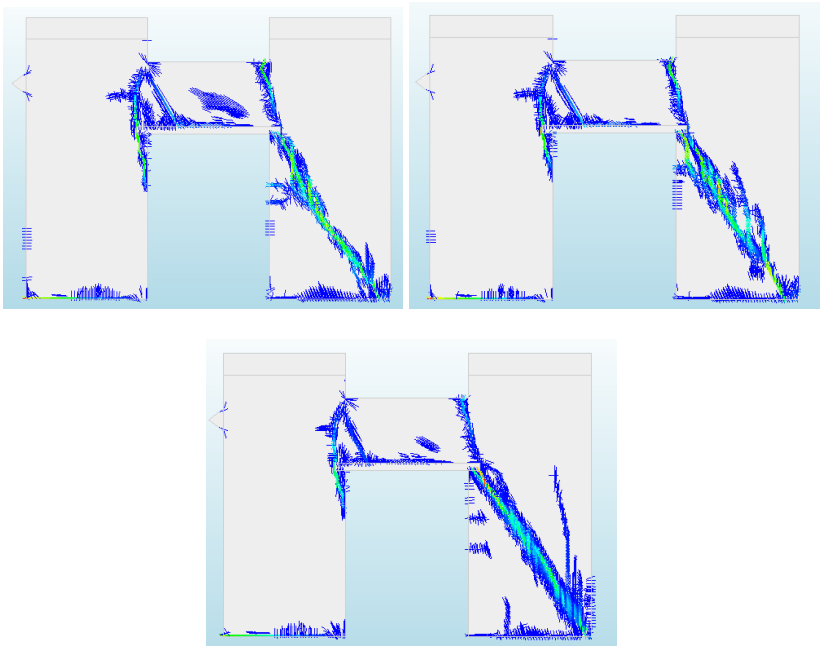

Figure 58. Damage contour for (a) f_t=0.09 MPa (b) f_t=0.11 Mpa (c) f_t=0.11 MPa (d) f_t=0.13 MPa (e) f_t=0.15 MPa (f) f_t=0.17 MPa

3.4.2 Influence of tensile fracture energy

As it was mentioned in previous section, the tensile fracture energy of the masonry as a composite material is difficult to be evaluated. A specific relation between it and another mechanical property of the masonry such as the tensile strength is not available so far. Its value is mainly based on bibliographical proposals (Lourenço 1996). Regarding the physical meaning, the tensile fracture energy is the energy an element is absorbing before it fails in tensile. Its value also controls the ductility of an element in tensile. Its behavior on a model must be evaluated with the adoption of a variety of different values.

The sensitivity analysis was carried out for the mechanical parameters presented in section 3.3.1.4. Five different values were given to the tensile fracture energy and their results are presented in Figure 59 and Figure 60.

It is observed that is not affecting significantly the damage pattern of the model. Nevertheless it is affecting the force displacement graph. More specifically increased values of fracture energy resulting increased ductility. It is observed that only for G_f=14 N/m the analysis is completed, while for lower values the model collapses due to diagonal cracking of the right pier for much lower displacement values.

As it was concluded from this sensitivity analysis the value of tensile fracture energy is not affecting significantly the results and its value should be adjusted to the value of the tensile strength to provide the desired ductility required.

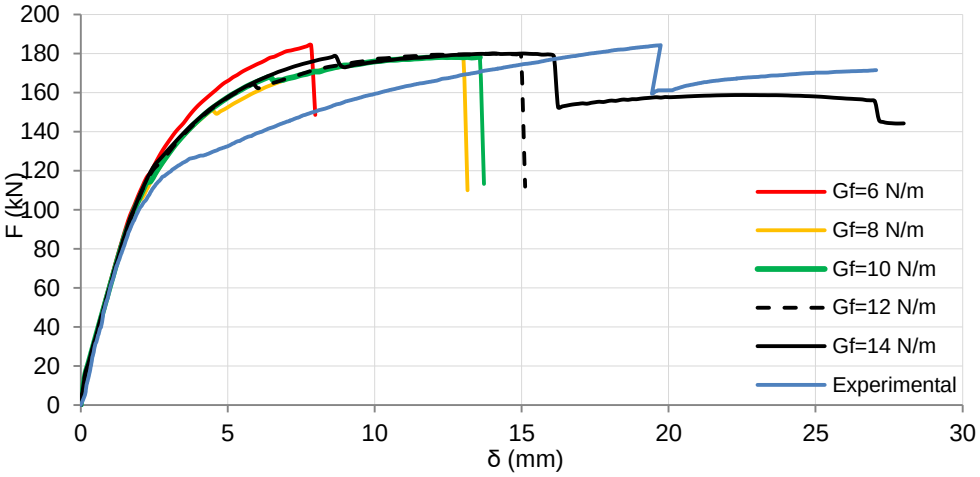

Figure 59. Load-displacement graph for different values of tensile fracture energy

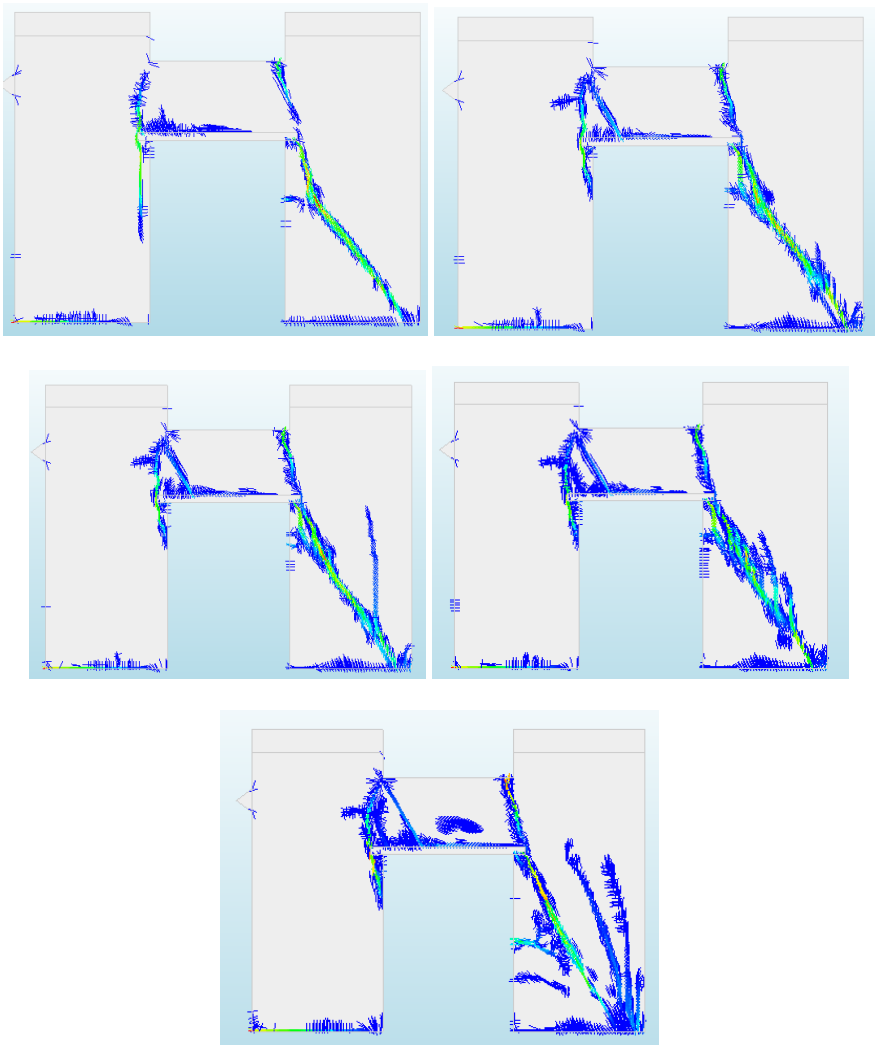

Figure 60. Damage contour for (a) G_f=6 N/m (b) G_f=8 N/m (c) G_f=10 N/m (d) G_f=12 N/m (e) G_f=14 N/m

3.4.3 Influence of timber lintel

3.4.3.1 Timber lintel without interface

Since the first analyses that were executed without the presence of the lintel failed to simulate the experimental crack pattern, the modelling of the timber lintel was considered necessary in order to simulate the real geometry with more accuracy.

The timber lintel was modeled using a linear elastic isotropic material model. The mechanical properties were:

Young's Modulus E=12 GPa

Poisson's ratio v=0.15

Density ρ=800 kg/m^3

With the addition of the timber lintel the behavior of the model changed significantly.

The first analysis showed an increased stiffness of the model in the elastic region. In order to match the elastic behavior of the experimental case the Young's Modulus was reduced from 2.19 GPa to 1.5 GPa. This change affected and later changing only the elastic region, without affecting the non-linear behavior.

As it is observed in Figure 61, the force-displacement curve of the new model is approaching better the experimental one in terms of maximum strength. Also the new model managed to obtain the shear cracking in the spandrel panel (Figure 62). These observations lead to the conclusion that the presence of the timber lintel is contributing to the improvement of the numerical model.

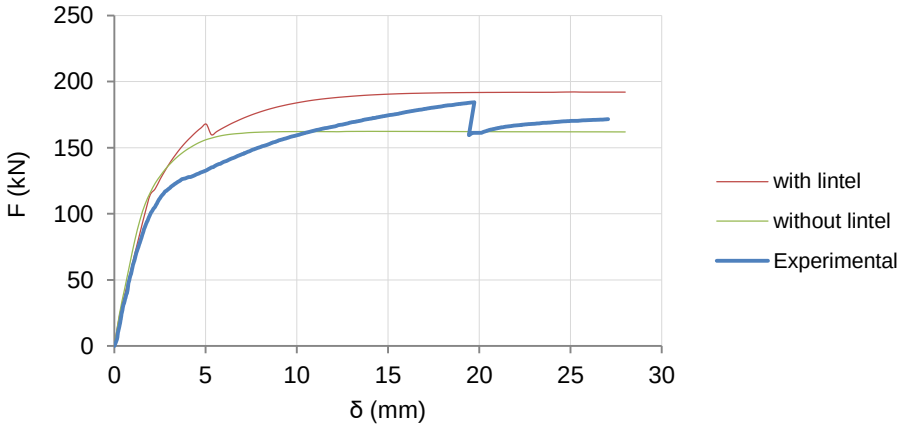

Figure 61. Timber lintel influence

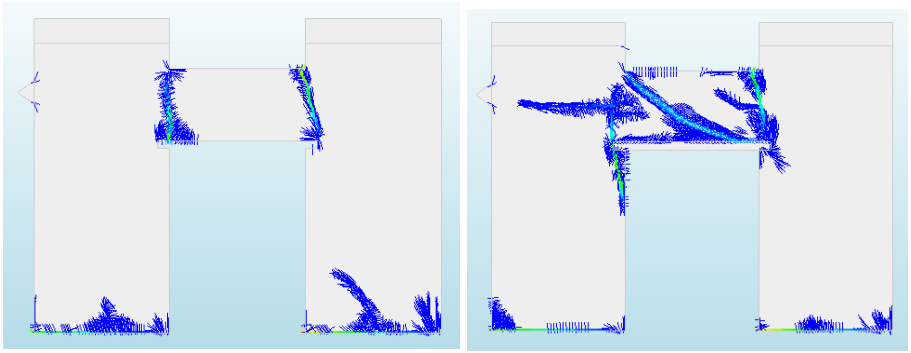

Figure 62. Crack pattern for numerical model (a) without and (b) with timber lintel. Maximum horizontal displacement d=28 mm.

Having a more analytical observation of the crack pattern different damage stages can be identified. More specifically:

For horizontal displacement d = 2 mm the structure stops to behave elastic and enters the non-linear area. At this point flexural cracks have been formed in the base of the piers as well as the end corners of the spandrel. (Figure 63a).

For horizontal displacement d = 5.7 mm a diagonal shear crack has been formed in the spandrel panel, resulting a sudden drop of the horizontal load capacity. (Figure 63b).

For horizontal displacement d = 28 mm the cracks have expended and a horizontal crack has formed in the left pier (Figure 63c).

Although the sequence of the crack propagation is satisfying and approximates the experimental one, the horizontal crack in the left pier for the last load step does not agree with the experimental one. In addition the shear failure of the spandrel is obtained for a displacement much lower than the experimental one (5.7 mm versus 19.16 mm for the experimental).

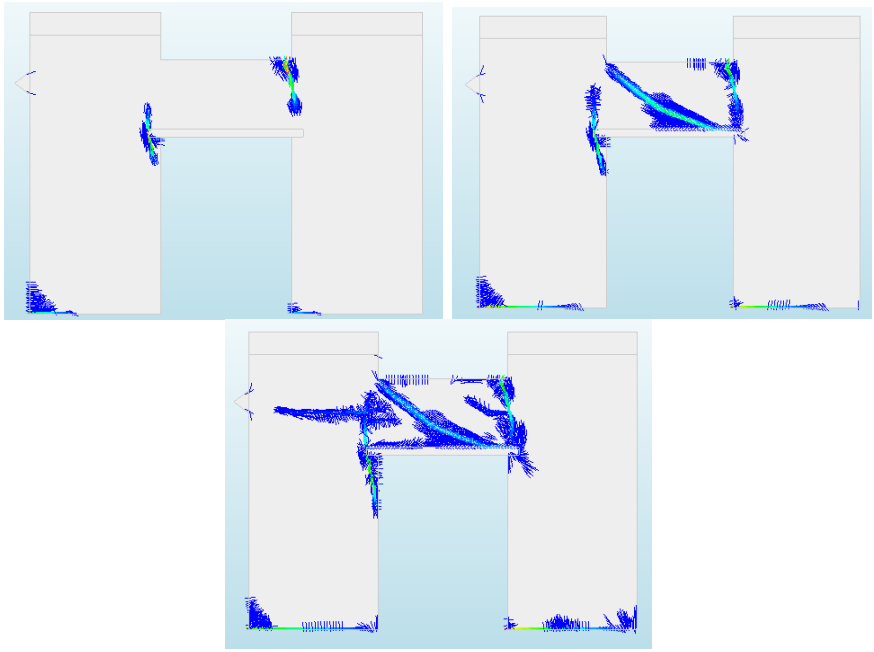

Figure 63. Crack damage for different values of horizontal displacement (a) d = 2 mm (b) d = 5.7 mm (c) d = 28 mm

3.4.3.2 Interface lintel-masonry

The implementation of the timber lintel showed a significant influence on the overall behavior of the numerical model, as it was discussed in the previous section. Nevertheless the interaction between masonry component and timber lintel was not realistic since it was defined with a continuum model. In order to obtain a more realistic representation an interface element was implemented between masonry and timber lintel (Figure 64). The type of element selected was the L8IF element available on DIANA software (Figure 65). The L8IF element is an interface element between two lines in a two-dimensional configuration. The local *xy* axes for the displacements are evaluated in the first node with *x* from node 1 to node 2. Variables are oriented in the *xy* axes. The element is based on linear interpolation.

The material model that was chosen was based in the Coulomb friction. The Coulomb friction criterion is illustrated in Figure 66.

For the definition of the Coulomb friction model DIANA requires as input parameters the normal and shear stiffness, cohesion, friction angle and dilatancy angle.

Although a significant number of experimental and analytical approaches exist about the friction between mortar and block, those parameters have not been defined explicitly for the interaction between mortar and timber. For this reason the initial values were defined based on the existing experience about the mortar-brick interaction and were updated, according to the conclusions that were made by the numerical analysis.

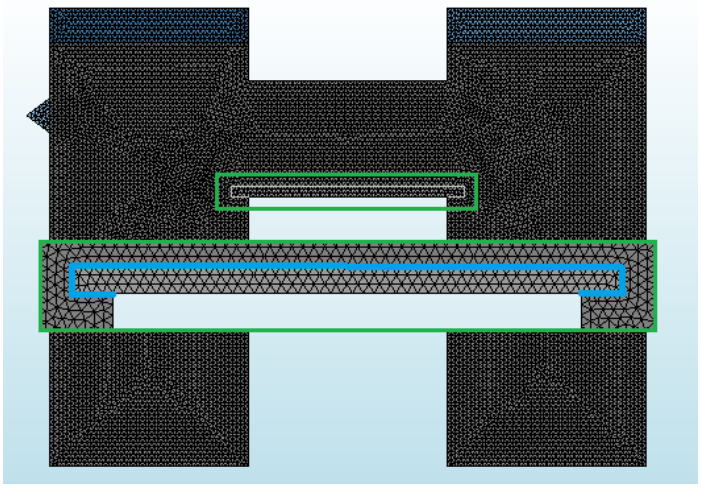

Figure 64. Application point of interface element

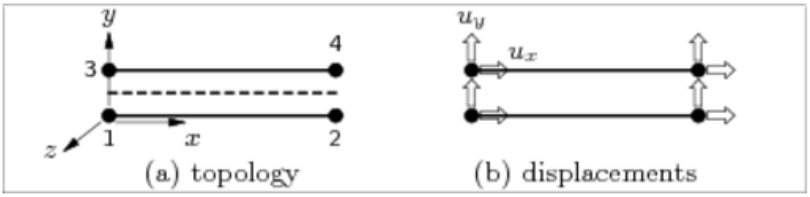

Figure 65. L8IF element

The normal and shear stiffness were defined by CUR (1994) with the following equation:

Normal stiffness:

$$k_n = \frac{E_u E_j}{h_j\left(\left|E_u - E_j\right|\right)} \tag{43}$$

Shear stiffness:

$$k_t = \frac{G_u G_j}{h_j\left(\left|G_u - G_j\right|\right)} \tag{44}$$

where:

E_u, E_j the Young's Modulus of the unit and mortar respectively

G_u, G_j the shear Modulus of the unit and mortar respectively

h_j, the thickness of the mortar joint

The values of the Young's and Shear modulus for units and mortar were derived from the experimental tests executed for the purposes of the campaign in the University of Naples and described in the section 3.2.2 (Table 3). It should be also noted here that this due to lack of data about

the unit—mortar-timber interface, the unit-mortar interface properties are considered as a starting point. The joint thickness is defined by the geometry and it is equal to 10 mm

Substituting those values to the equations the following values are obtained:

k_n = 1.17e13 N/m^3

k_t = 1.35e11 N/m^3

The values of the cohesion and the friction angle were derived from the experimental tests performed to triplet specimens for the definition of the mortar-unit interaction (section 3.2.2, Table 5). Therefore:

c=0.146 N/m^2

φ=0.279 rad

The diltancy angle was kept in a low value, approximately equal to zero, due to the absence of restriction and confinement at the top of the specimen.

ψ=0.05 rad

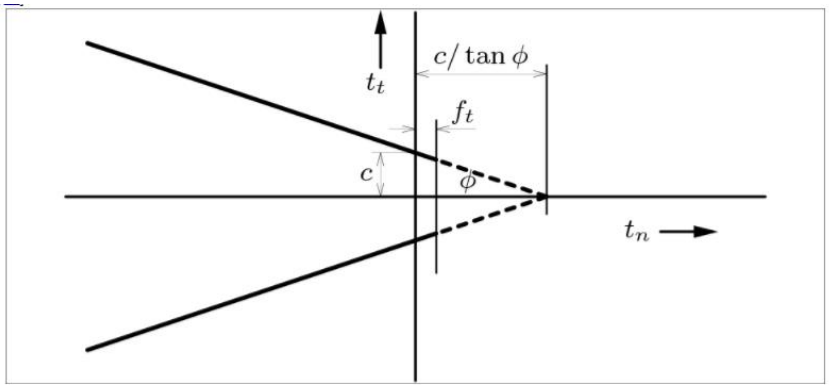

Figure 66. Coulomb friction criterion

The first analysis executed with the application of the interface between timber and masonry showed controversial results.

The cracking pattern resulted from the analysis is presented in Figure 67. At the end of the elastic region, flexural cracks had been formed in the base of the piers as well as the end section of the spandrel. As the horizontal displacement was increasing a diagonal crack was formed in the spandrel but without a clear shear form. Finally the specimen collapsed with the creation of a diagonal crack in the right pier. Cracks were also formed in the interface lintel-masonry.

The comparison between the previous analyses in terms of force-displacement diagram is illustrated in Figure 68. The new model managed to simulate in a more appropriate way the capacity curve of the

model, resulted a maximum force closer to the experimental one. Nevertheless it did not obtain the same ductility. The inability of the spandrel to fail in shear led to a concentration of stresses to the piers, resulting to the failure of the right one.

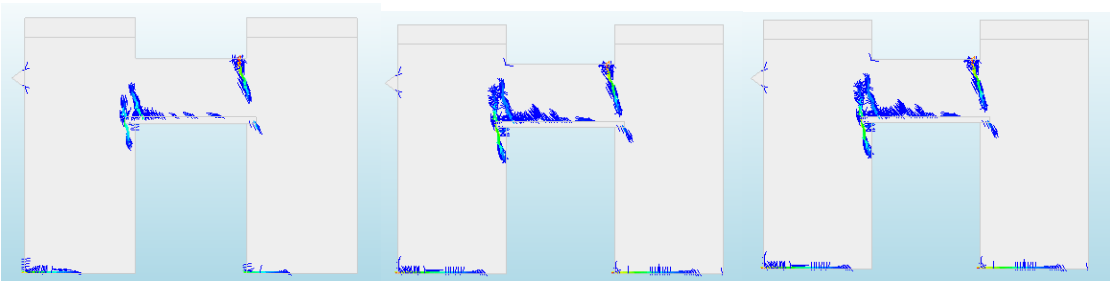

Figure 67. Crack pattern of analysis with interface element (a) d = 2.8 mm (b) d = 6.3 mm (c) d = 12.46 mm

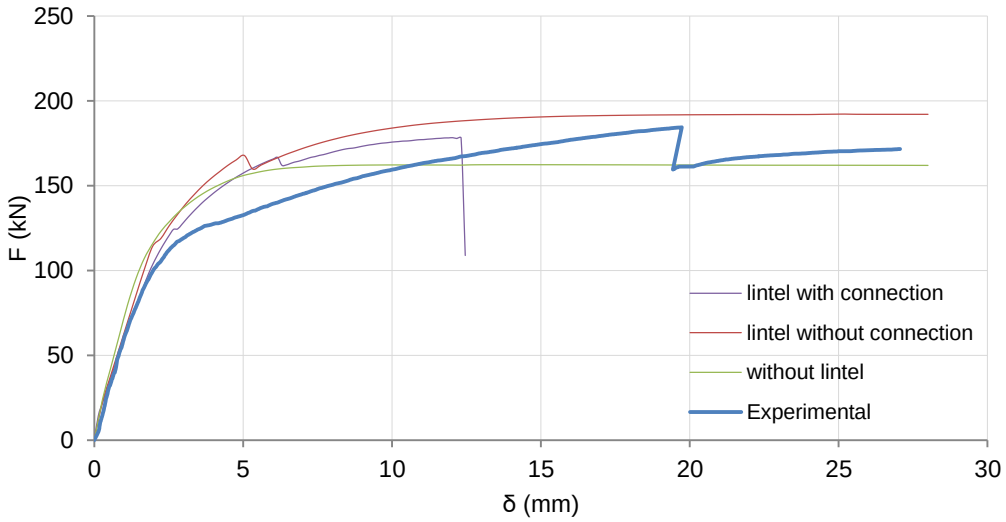

Figure 68. Force-displacement diagram comparison

In order to improve the result the tensile strength was decreased from 0.15 MPa to 0.11 MPa in order to obtain diagonal failure at the spandrel. The value was selected after a series of analysis with different values of tensile strength (see more analytical in section 3.4.1) Also the tensile fracture energy was increased from 10 to 12 N/m to result a more ductile behavior in shear failure. The results are illustrated in Figure 69 and Figure 70.

The sequence of cracks was in good approximation with the experimental ones. At the end of the elastic region (d=1.82 mm) flexural cracks formed in the base of the piers as well as the end section of the spandrel. For d= 4.76 mm the spandrel failed in shear while for the maximum displacement of d=16.38 mm the right pier failed in shear, resulting the collapse of the model.

Although a good approximation seemed to be obtained in terms of crack pattern, the shear failure of the spandrel was obtained for a much smaller horizontal displacement (4.76 mm instead of 19.16 mm at the experiment).

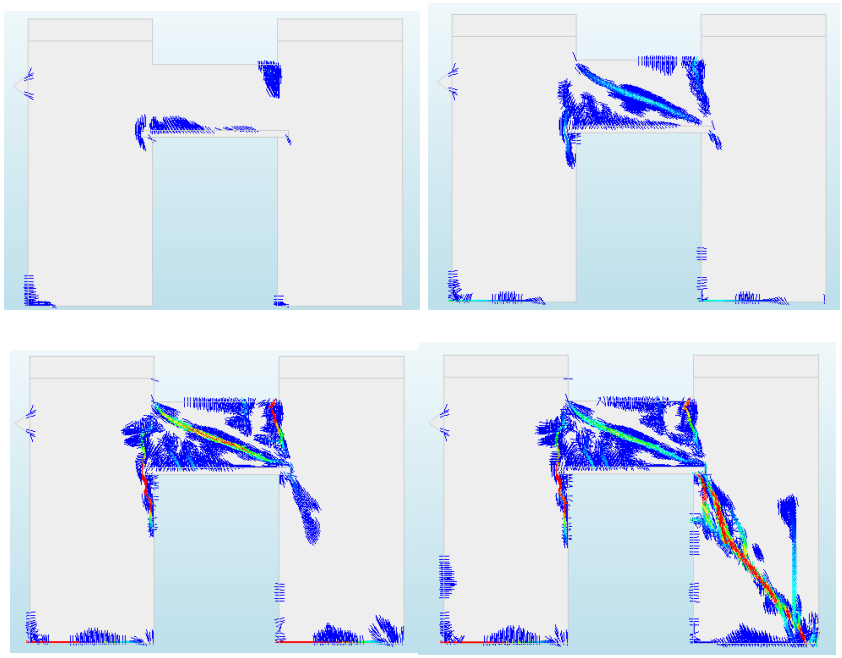

Figure 69. Crack pattern for (a) d=1.82 mm (b) d=4.76 mm (c) d= 16.24 mm (d) d=16.38 mm

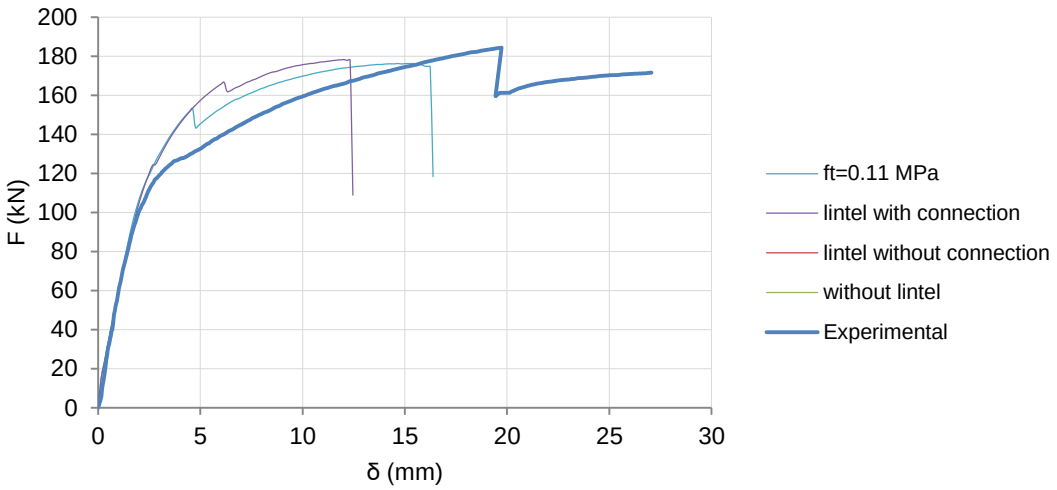

Figure 70. Force-displacement diagram comparison

In order to evaluate the behavior of the model and its drawbacks a more detailed examination of the spandrel panel cracks was executed. Two main observations were made. (Figure 71). First of all a

high concentration of smaller diffused cracks is observed at the interface element between masonry and timber. These cracks are created due to the high stiffness of the interface element, which leads to a high concentration of stresses, resulting to the observed cracks. Second the flexural crack in the bottom left section of the spandrel propagated around the timber lintel and not above it as it happen in the experiment. This crack expanded also as a vertical crack in the left pier.

Those observations leaded to the following conclusions:

- The stiffness value of the interface element leads to undesirable diffused cracks at the bottom of the spandrel.
- The interface element fails to define the real connection between lintel and masonry at the lintel's anchorage length of 15 cm. More specifically it does not letting the spandrel to detach from the mortar connecting it with the specimen and also rotate.

This leads to a re-orientation of the cracks and an undesirable behavior for the whole model. The cracks that were created due to the reasons that were mentioned above are weakening the resistance of the spandrel and leading it to an early failure due to shear. The failure of the spandrels leads to the uncoupling of the piers and finally the right one also fails in shear.

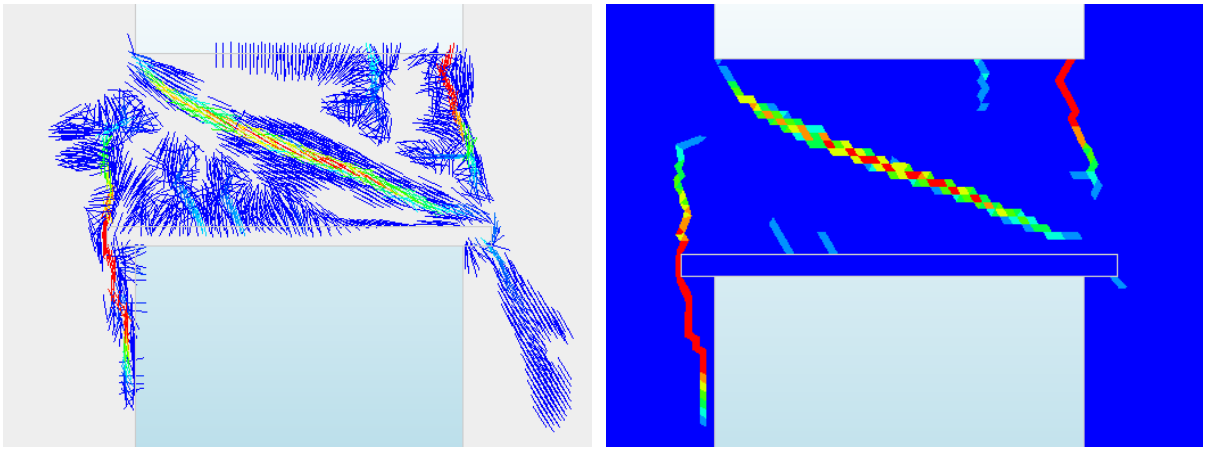

Figure 71. (a) Crack pattern and (b) contour plot of the principal strains for the spandrel panel (d=16.24 mm)

Taking into account those conclusions the decision of an updated interface between timber and masonry was decided. The new interface included two different interface elements, with the same material type (Coulomb friction) but different mechanical properties from the previous ones.

The configuration of the new interface is illustrated in Figure 72. The two different types of interface had the following characteristics:

Middle connection:

The connection connecting the timber lintel with the lower part of the spandrel panel had a decreased stiffness as well as cohesion in order to avoid undesirable concentration of stresses and cracks in the lower part of the spandrel. The mechanical properties of this interface are presented in Table 13.

Anchorage connection:

The interface between lintel and masonry at the position of the anchorage length was designed with great caution. In order to obtain the detachment of the timber lintel from the spandrel and allow its rotation, without causing the cracking pattern described above, this interface element was modeled with much lower stiffness, as well as zero cohesion and significantly reduced friction angle. The mechanical properties of this interface are presented in Table 14.

There should be noted in that point that, although the connection between mortar and mortar has been extensively investigated and characterized, much less information exists about the interaction between mortar and timber. The initial values that were obtained by experimental results (Table 5), proved inadequate to simulate the actual state of interaction.

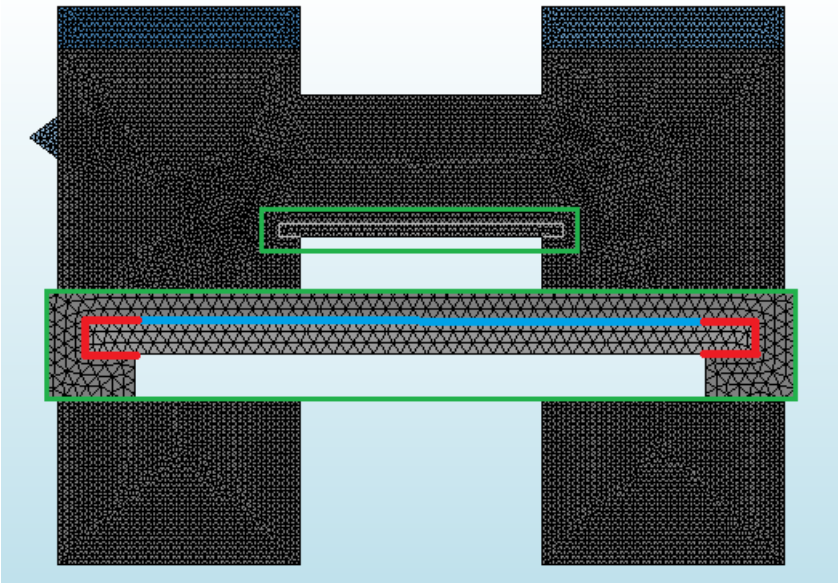

Figure 72. New addopted connection

For this reason a sensitivity analysis was carried out in order to evaluate the influence of every interface parameter and select the optimal one for the calibration of the model. The results of the sensitivity analysis will be presented in detail in section 3.4.3.3. The final properties of the interface that were presented above were decided after different trials during the sensitivity analysis.

Table 13. Mechanical properties of middle interface connection

k_n	k_t	c	φ	ψ
N/m^3	N/m^3	N/m^2	rad	rad
6.21E+10	6.21E+10	0.1	0.4	0.01

Table 14. Mechanical properties of anchorage interface connection

k_n	k_t	c	φ	ψ
N/m^3	N/m^3	N/m^2	rad	rad
6.21E+08	6.21E+08	0	0.1	0.01

3.4.3.3 Interface properties

In section 3.4.3.2 it was concluded that the material properties for the interface between timber and masonry were not be able to be estimated by existing expressions and equations. Due to uncertainties that were concerned those properties, several sensitivity analysis were carried out. These analyses were performed for the connection of the anchorage part of the lintel, since this connection was considered as the most influential for the behavior of the numerical model.

The rest of the model's mechanical properties were kept the same as the final calibrated model (see section 3.5 for exact values).

Influence of stiffness

The results of the sensitivity analysis are illustrated in Figure 73 and Figure 74. These results are justifying the big influence of the connection stiffness to the interaction between lintel-masonry and therefore the behavior of the whole model.

More specifically comparing the damage contour of every analysis, it is shown that the desired crack pattern is obtained by a range of values for the interface stiffness, from approximately 4e8 to 8e8 N/m^3. For these values also a satisfying load-displacement graph is obtained. The only difference is the value of horizontal displacement for which the spandrel is failing in shear. This value can be modified also by different values of tensile strength. That means that the numerical model can match the experimental case for different combinations of tensile strength-interface stiffness. Nevertheless those values should vary within a narrow margin.

On the other hand for higher or lower values than the one mentioned above, it is observed an undesired behavior in both damage pattern and force displacement diagram. The spandrel did not reach a diagonal failure which led to the failure of the right pier.

Those results led to the conclusion that the calibration of the numerical model is strongly influenced by the interface stiffness of the lintel's anchorage length, and it should not exceed certain values.

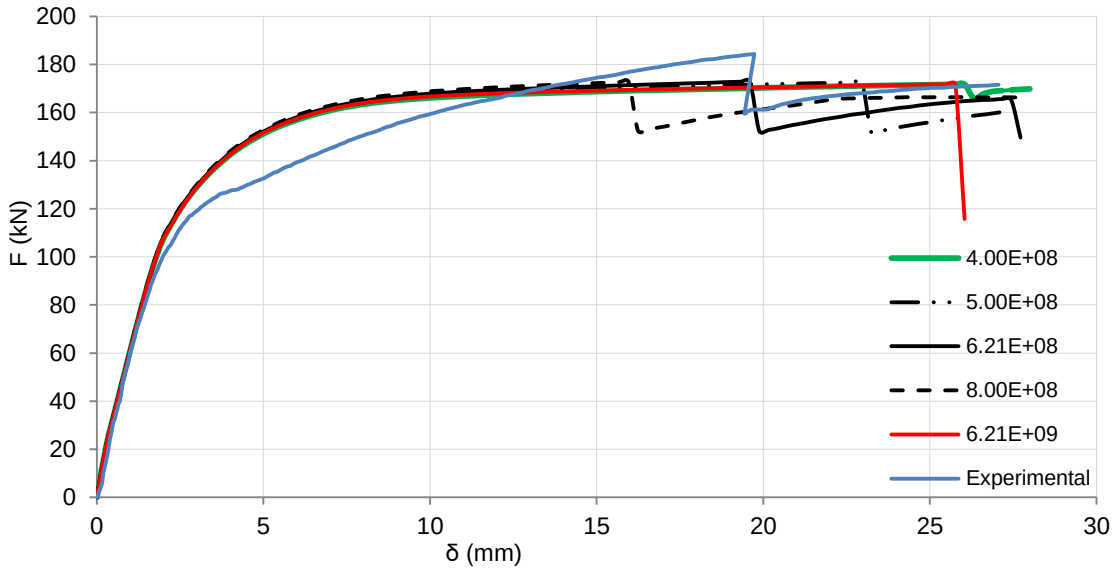

Figure 73. Load-displacement graph for different values of interface normal and shear stiffness k_n,k_t

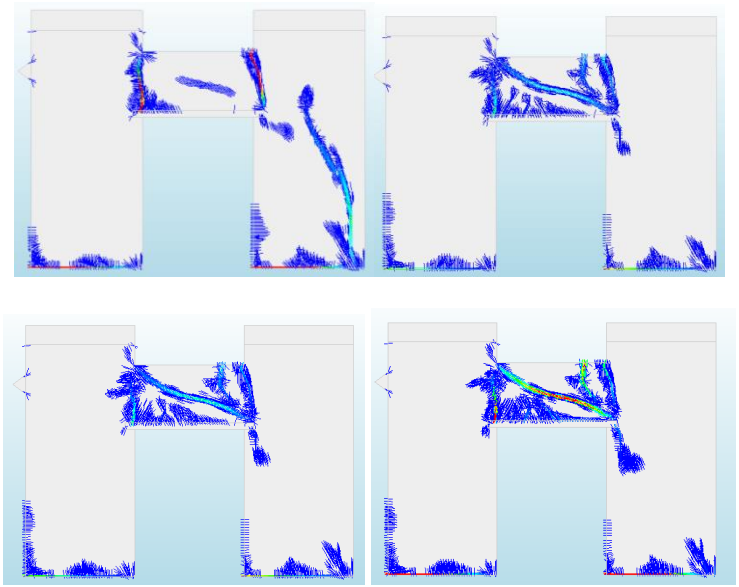

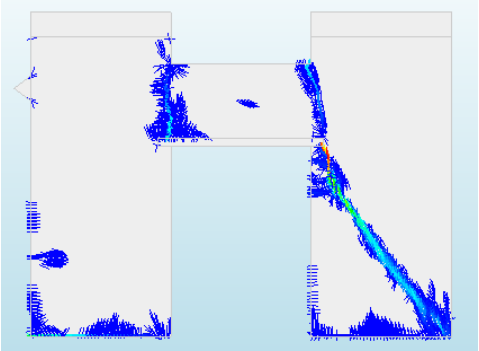

Figure 74 Damage contour for (a) $k_{n,t}$=4 e 8 N/m^3 (b) $k_{n,t}$=5 e 8 N/m^3 (c) $k_{n,t}$=6.21 e 8 N/m^3 (d) $k_{n,t}$=8 e 8 N/m^3 (e) $k_{n,t}$=6.21 e 9 N/m^3

Influence of friction angle

The results of this sensitivity analysis are illustrated in Figure 75 and Figure 76. For a low value of friction angle equal to 0.01 the model is failing in shear simultaneously in the spandrel and the right pier. For φ=0.1 a satisfying result is obtained, while for higher values undesirable cracks are formed in the piers.

Regarding the force displacement graph, the friction angle is not affecting the maximum capacity, but is affecting the displacement for which the spandrel is failing in shear.

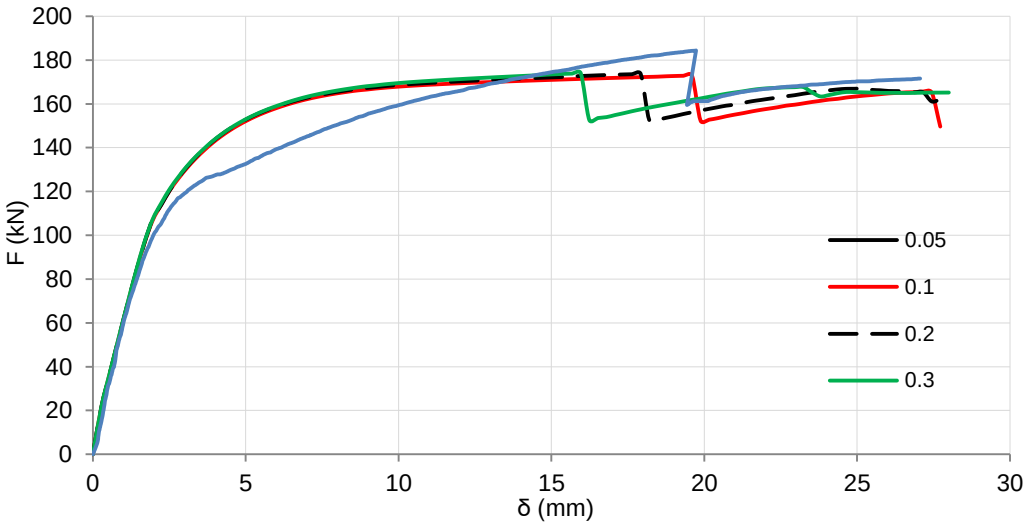

Figure 75. Load-displacement graph for different values of interface friction angle

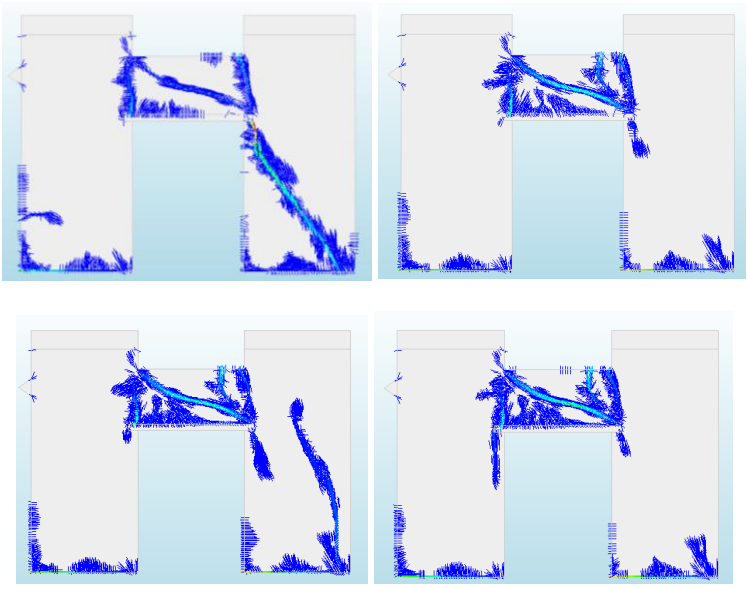

Figure 76. Damage contour for (a) φ = 0.05 rad (b) φ = 0.05 rad (c) φ = 0.1 rad (d) φ = 0.2 rad (e) φ = 0.3 rad

Influence of cohesion

Four different analyses were carried out with different values for the interface's cohesion. The values that were given were 0, 0.01, 0.05, 0.1. The results in terms of both damage pattern and force-displacement graph were identical. This reveals a negligible influence of the interface cohesion to the numerical model. Therefore the initial value of 0 was adopted for the final model.

Influence of dilatancy angle

The sensitivity analysis that was executed for different values of dilatancy angle showed a negligible influence on the damage pattern as well as a small influence in the force-displacement diagram (Figure 77). According to literature The effect of the dilatancy angle is only relevant for applications in which masonry is confined, due to the interlocking effect of the units and the associated stress built-up (Angelillo et al. 2014). Therefore the value of the dilatancy angle was set to 0.01 rad, since the software is not allowing the input of zero for this property.

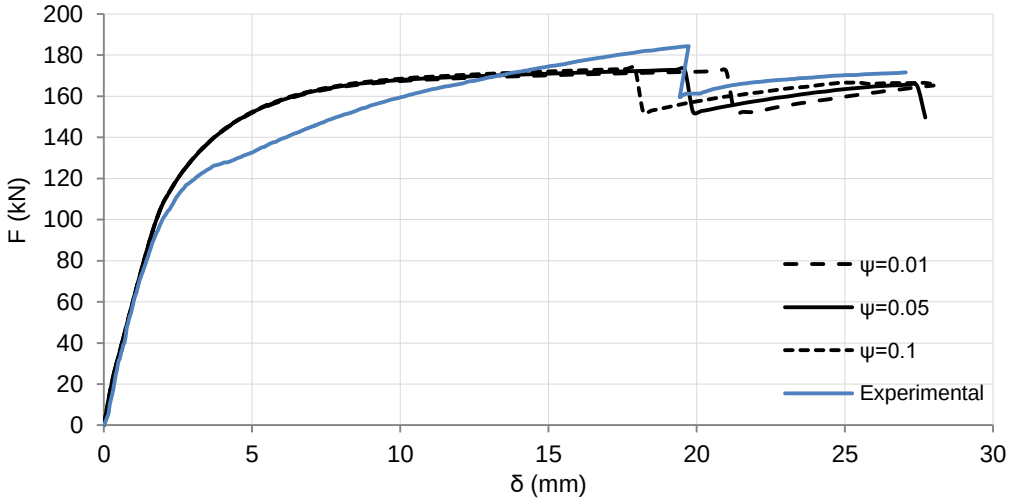

Figure 77. Load-displacement graph for different values of interface dilatancy angle

3.5 Final model

In order to obtain the exact same behavior as the experimental case, mechanical parameters such as tensile strength, tensile and compressive fracture energy were changed, taking into account the parametric analyses, which was be described in section 3.4. The mechanical properties of the Total Strain Based Crack material model chosen for the masonry component are presented in Table 15. Regarding the crack model, Rotating crack orientation was selected as well as the Rots crack bandwidth specification. The properties of the interface element connecting timber lintel and masonry component were the ones presented in Table 13 and Table 14.

Table 15. Mechanical properties of masonry component

E	v	ρ	f_c	G_c	f_t	G_f
GPa	-	kg/m^3	MPa	N/m	MPa	N/m
1750	0.27	1200	3.96	20000	0.1215	14

The crack pattern resulted from the final model is presented in Figure 78 and the force displacement diagram in Figure 79. For horizontal displacement d=2.52 mm, the model is reaching the limits of the elastic region. For this displacement flexural cracks are formed in the base of the piers and the end section of the spandrel panel. Those cracks continue to propagate and for d=10.36 mm diagonal shear cracks are showing up in the middle part of the spandrel. This crack continue to expand and for d=19.88 mm the maximum horizontal force is obtained and the spandrel panel fails in shear causing an instant drop of horizontal from 171.81 kN to 151.72 kN. The instant drop of strength will be followed by a hardening behavior, meaning a further increase of the horizontal force, until the maximum horizontal displacement of 27.16 mm. The final crack pattern was similar to the one for d=19.88 mm with more diffused cracks in the spandrel panel.

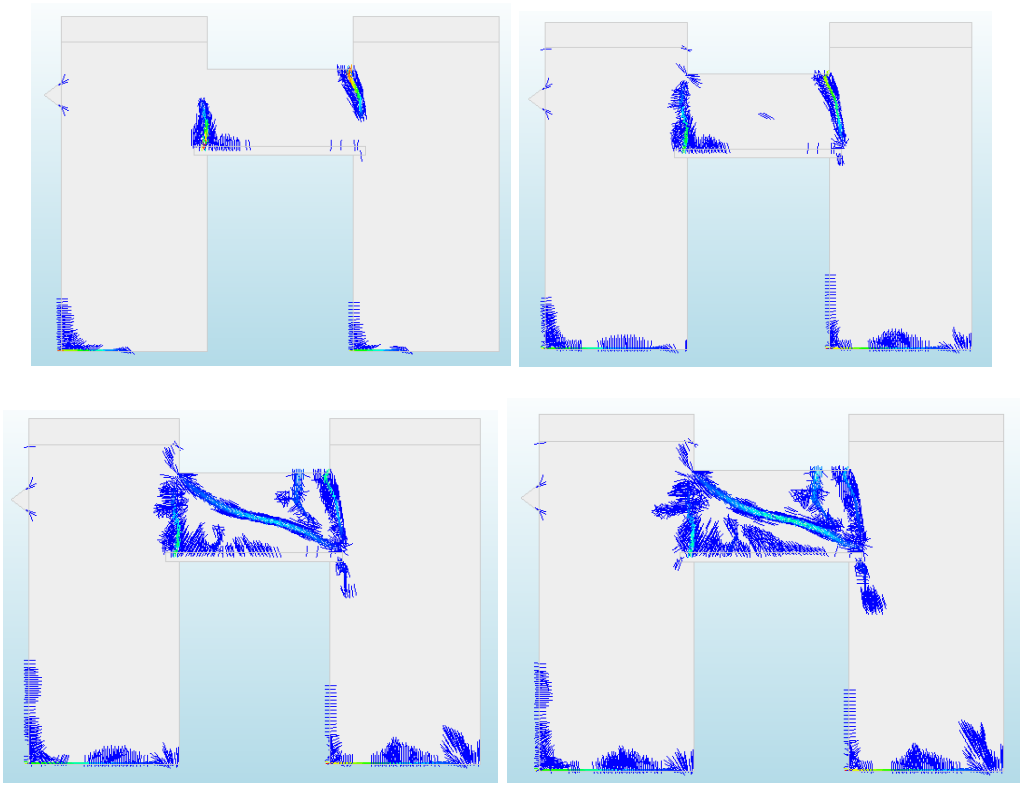

Figure 78. Crack pattern for horizontal displacement (a) d = 2.52 mm (b) d = 10.36 mm (c) d = 19.88 mm (d) d = 27.16 mm

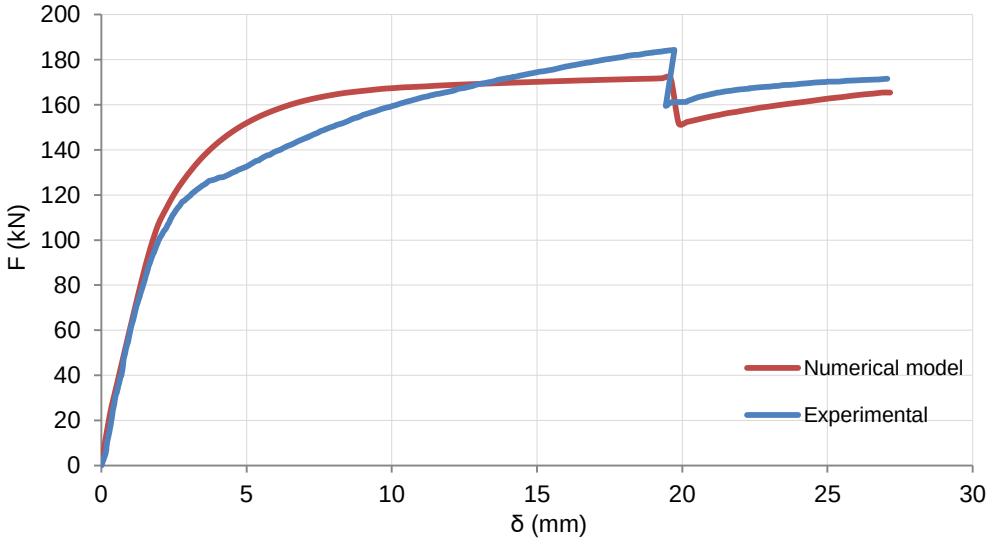

Figure 79 Force-displacement diagram of the numerical model.

Comparing the crack pattern between the FE model and the experiment (Figure 80) it is observed a good approximation of the actual behavior of the portal frame by this numerical approach. The two crack patterns match as far as the main cracks are concerned. The only difference was that the FE model gave a more diffused crack pattern especially in the spandrel panel which could be related to the adoptive damage model. Although the main damage mechanism was represented in a satisfying level.

Regarding the model's force-displacement diagram (Figure 79), it is in good correspondence with the experimental one. It manages to obtain the same elastic branch. Furthermore as far as the non-linear behavior is concerned, both diagrams show a degradation of stiffness with an increasing of the lateral force. After the model reaches the maximum force it is obtaining an instant drop of strength like in the experimental case. This degradation was equal to 11.69% versus 13.5% for the experimental. Also both FE model and experiment specimen, showed a hardening behavior after the instant drop of strength. The only drawback of this model's simulation of the experimental case is the calculation of lower value for the maximum horizontal force. The numerical model obtained a value of 171.81 kN, versus 184.37, meaning a 6.8% difference. This inability of the model to evaluate explicitly the maximum strength was probably due to the adoptive crack model. The adoptive smeared crack approach, gave a more diffused crack pattern as explained above. Those cracks dissipated more energy than the real situation leading to an underestimation of the maximum strength. This conclusion must be taken into account with great caution, for the case of the application of this numerical approach to other cases.

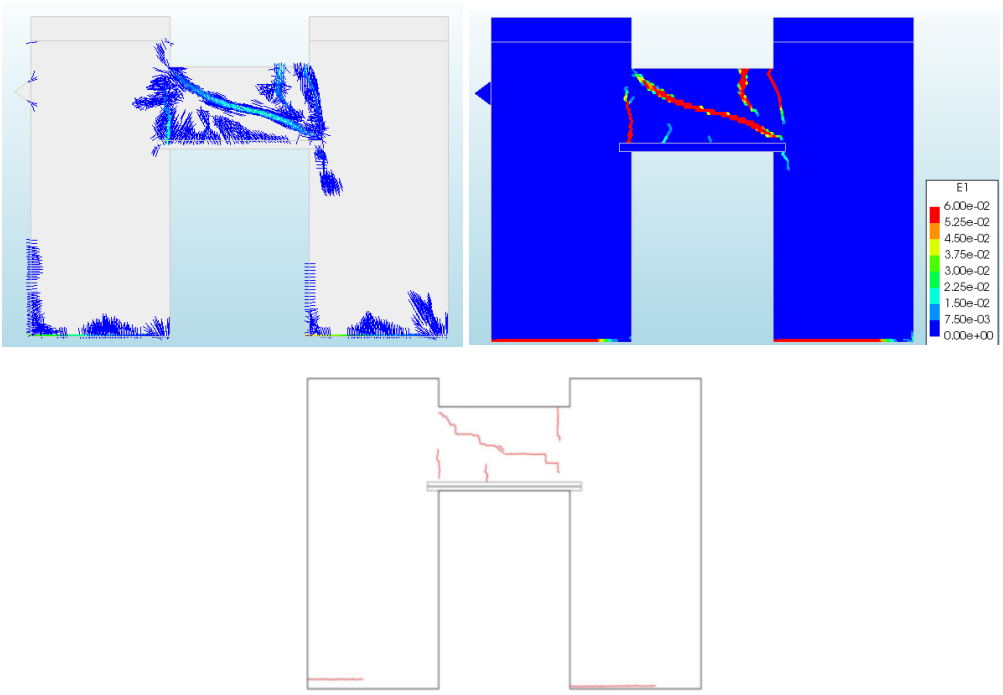

Figure 80. Comparisson between experimental and numerical crack patterns (a) Numerical crack pattern (b) numerical contour of principal strains and (c) experimental crack pattern for maximum horizontal displacement

The evaluation of the numerical model's efficiency required also its comparison with different numerical approaches that used the benchmark problem of Naple's University. Those cases were explained in sections 3.2.5.1-3.

This comparison is presented in terms of crack pattern in Figure 81 and in terms of force-displacement diagram in Figure 82. It is observed that the numerical model created in the current study is obtaining a better approximation of the damages occurred in the frame than the Parisi et al. (2011) micromodel, as well as the Salvatoni & Ugolini (2016) macromodel. In the first case the decision not to model the timber lintel altered the behavior of the model resulting to a non-representative result with diagonal cracking in the base of the piers. In the second one the inadequate representation between masonry and timber lintel led to a different behavior with diagonal failure of the right spandrel. The model created by Saloustros et al. (2016) gave a very good approximation of the actual state of damage, similar to the one created within this thesis with a less diffused crack pattern due to the use of a crack tracking algorithm.

Regarding the load-displacement graph the models of Parisi et al. (2011) and Salvatoni & Ugolini (2016) obtained a satisfying estimation of the maximum load capacity. Nevertheless the maximum horizontal load was obtained for a displacement lower than the experimental one. This in combination with the obtaining of the diagonal cracks in the piers leads to the conclusion that these models underestimate the displacement capacity of the specimen and do not obtain a satisfying representation of the non-linear behavior of the portal frame. Saloustros et al. (2016) model manage to obtain the exact same behavior of the experimental model also in terms of load-displacement relation. The crack-tracking algorithm with the combination of a good representation of the lintel-masonry interaction allowed the satisfying simulation of the maximum load and displacement capacity of the portal frame.

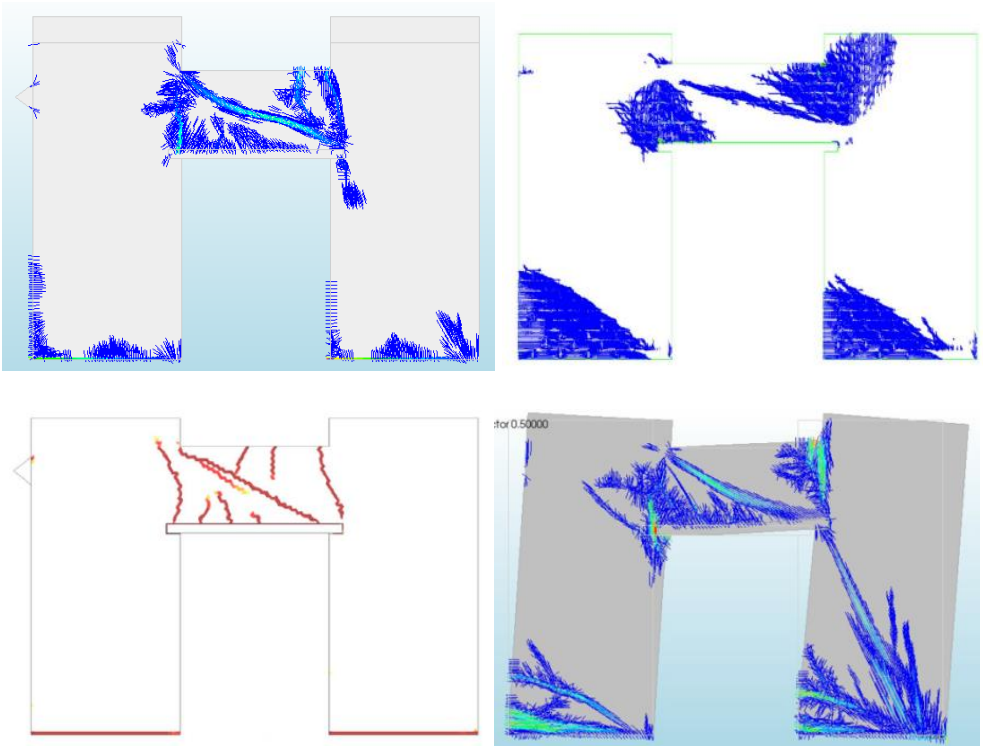

Figure 81. Crack damage contour for: (a) Thesis adopted model (b) Parisi et al. (2011) model (c) Saloustros et al. (2016) model and (d) Salvatoni & Ugolini (2016) model.

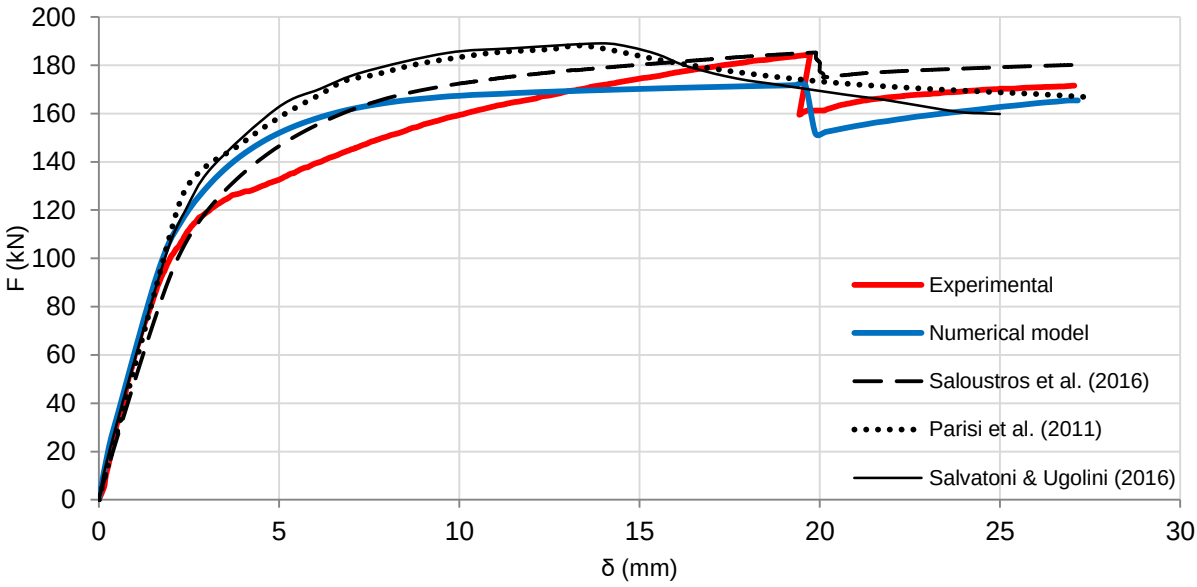

Figure 82. Load-displacement graph of the experimental test and the numerical analyses.

3.6 Conclusions-recommendations

The process of creating and calibrating the numerical model as well as the parametric study and the comparison with similar numerical approaches led to the adoption of several conclusions and recommendations regarding the structural analysis of masonry façades:

- The Finite Element macromodelling approach consists a reliable and explicit tool for the estimation of the in-plane behavior of masonry façades, requiring relatively low computational cost.
- The Finite Element method requires the estimation of several material properties from experimental tests as well as their influence through the execution of an analytical parametric study.
- The proper simulation of the timber lintel-masonry interface is significantly influencing the behavior of masonry spandrels.
- More explicit and accurate methodologies such as micromodelling, can lead to less accurate results if physical parameters such as the lintel influence are not defined properly.
- The smeared crack approach leads to diffused crack pattern, which consequently can lead to underestimation of the spandrels maximum capacity.
- Crack tracking techniques can enhance the possibilities of the macromodelling approach.

4. MICROMODELLING APPROACH

4.1 Introduction

The macromodelling approach that was developed and described in section 3 proved to be a reliable tool for the assessment of masonry façades subjected to in plane lateral loads. Nevertheless some of this method's drawbacks such as the generation of a diffused crack pattern, especially in the spandrel panel, as well as the overestimation of the maximum lateral strength by 6.8%, led to the decision about a supplementary numerical approach of the spandrel's behavior. After detailed examination of the state-of-the-art review presented in section 2, the creation of a micromodel was decided. This approach was considered suitable, since it can give a more realistic and explicit representation of the masonry behavior. The micromodelling technique used was the one of the simplified micromodellig, where the units are modeled separately, and the mortar joint as well as the interface of mortar-unit are represented as a unique interface element based in Coulomb friction.

4.2 Model characteristics

For the micromodel the exact same geometry as the macromodeling approach was selected. Regarding the mesh type, quadratic elements based on quadratic interpolation for the masonry were used to provide greater accurancy in the numerical solutions. Simpler triangular elements based on the quadratic interpolation were used for the timber lintel, since less accuracy was needed. The interface elements between different units were modeled with linear elements based on the quadratic interpolation. The mesh size was set to 4 cm, based on the parametric analysis that was performed for the macromodel.

The material type was defined as Total Strain Based Crack Model for the units, while Coulomb friction interface material model was selected for the interace of unit-mortar and masonry-lintel.

As well as the material properties input is concerned the following decisions were made:

For the unit material model:

The input parameters were derived from experimental tests performed for both units and mortar (Parisi et al. 2011). The values for tensile and compressive fracture energy for the tuff stones were derived initially from the suggestions of Parisi et al. (2011) and were 1 and 2000 N/m respectively. Nevertheless their values were significantly increased. The low value of tensile fracture energy in combination with the mesh size was affecting the numerical solution. In order to obtain for the numerical solution to obtain convergance a value of 20 N/m was adopted. The compressive tensile energy followed the formulation proposed by Mode Code 90 (CEB-FIP 1993) and therefore was set to 12000 N/m since the value of 2000 N/m resulted a brittle damage pattern. Finally the crack orientation was set to rotating, taking int account the conclusions from the macromodelling approach. The initial material parameters for the units are presented in Table 16.

Table 16. Material properties for units.

E	v	ρ	f_c	G_c	f_t	G_f
GPa	-	kg/m^3	MPa	N/m	MPa	N/m
1540	0.2	1172	4.13	12000	0.23	20

The interface parameters for the connection of timber and masonry were derived from the calibrated macromodel (Table 13, Table 14), since all the parameters have been already calibrated through a detailed parametric study (section 3.4.3.2).

The material properties of the interface between units were derived by certain suggestion of the bibliography (Lourenço 1996). More specifically:

The normal and shear stiffness were defined by CUR (1994) with the following equation:

Normal stiffness: $k_n = \frac{E_u E_j}{h_j(|E_u - E_j|)}$

Shear stiffness: $k_t = \frac{G_u G_j}{h_j(|G_u - G_j|)}$

where:

E_u, E_j the Young's Modulus of the unit and mortar respectively

G_u, G_j the shear Modulus of the unit and mortar respectively

h_j, the thickness of the mortar joint

The values of the Young's and Shear modulus for units and mortar were derived from the experimental tests that executed for the purposes of the campaign in the University of Naples and described in the section 3.2.2 (Table 3). The joint thickness is defined by the geometry and it is equal to 10 mm

Substituting those values to the equations the following values are obtained:

k_n = 1.17e13 N/m^3

k_t = 1.35e11 N/m^3

The tangent of the friction angle was set to 0.75 since it was proved to be independent by the type of unit and mortar (Lourenço 1996).

The value of the dilatancy angle was set equal to 0, due to high confining stresses acting on the interface

The cohesion was set to 1.5 times the tensile strength of the unit (Lourenço 1996), therefore:

c=1.5ft=1.5 0.23=0.345

4.3 Numerical solution

The iterative method was again defined by the regular Newton-Raphson method. The convergence norm was again defined as displacement control, since the loading was applied as a lateral imposed displacement, with convergence tolerance of 0.01.

Due to the inability of the model to obtain numerical solution in the first analysis that were executed the use of arc length parameter was selected with the method of spherical path. The arc length method control point was set to a node in the top right face of the right pier, which was observed to remain relatively unformed during the loading process.

The step size was kept the seam as the macromodel (0.01) in order not to increase the computational cost of the numerical solution.

4.4 Parametric study

The creation of a micromodell is a difficult task, since its calibration requires an increased number of parameters, which have different influence on the model's behavior. Since most of the material properties were defined from experimental tests, a parametric study was executed only in the case of limited material properties. In this section this brief parametric study is presented.

4.4.1 Influence of tensile fracture energy

The tensile fracture energy is a value that is difficult to be obtained by experimental tests. Its value is usually adjusted to every modeling case. Different values for this property were defined and the results are presented in Figure 83, Figure 84, Figure 85 and Figure 86.

It is observed that the value of tensile fracture energy is influencing the ductility of the model, increasing the displacement for which the spandrel fails in shear. The crack pattern was also less diffused for increasing values of fracture energy, while for the value of 40 N/m the spandrel cracking initiated as horizontal instead of diagonal. The load-displacement curves were not significantly affected by this change in terms of maximum strength.

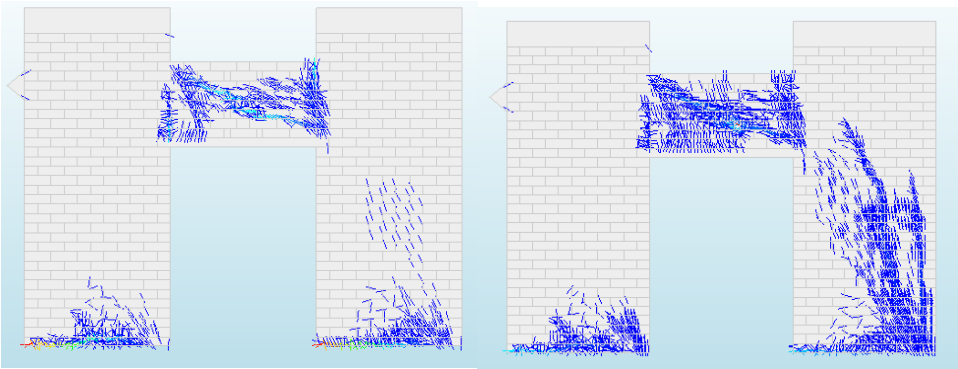

Figure 83. Damage pattern for Gf=20 N/m (a) d=10.92 mm (b) d=22.79 mm

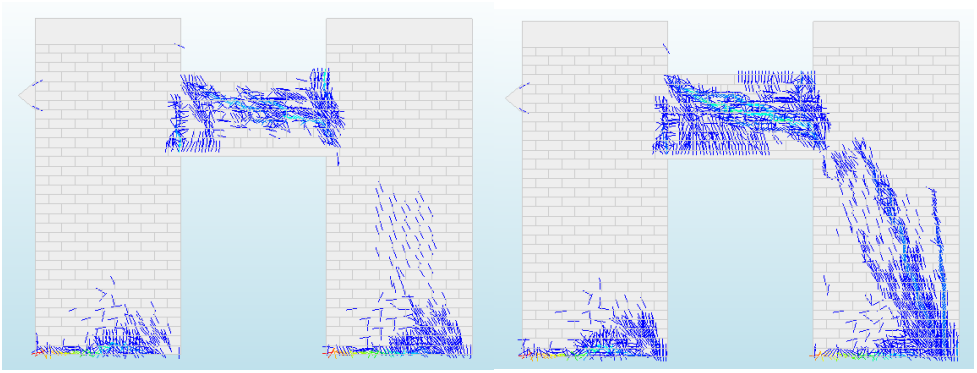

Figure 84. Damage pattern for Gf=30 N/m (a) d=11.07 mm (b) d=27.01 mm

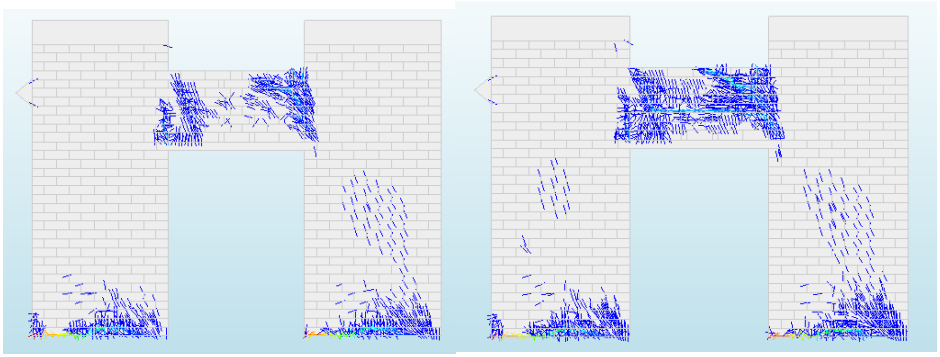

Figure 85. Damage pattern for Gf=40 N/m (a) d=13.47 mm (b) d=27.62 mm

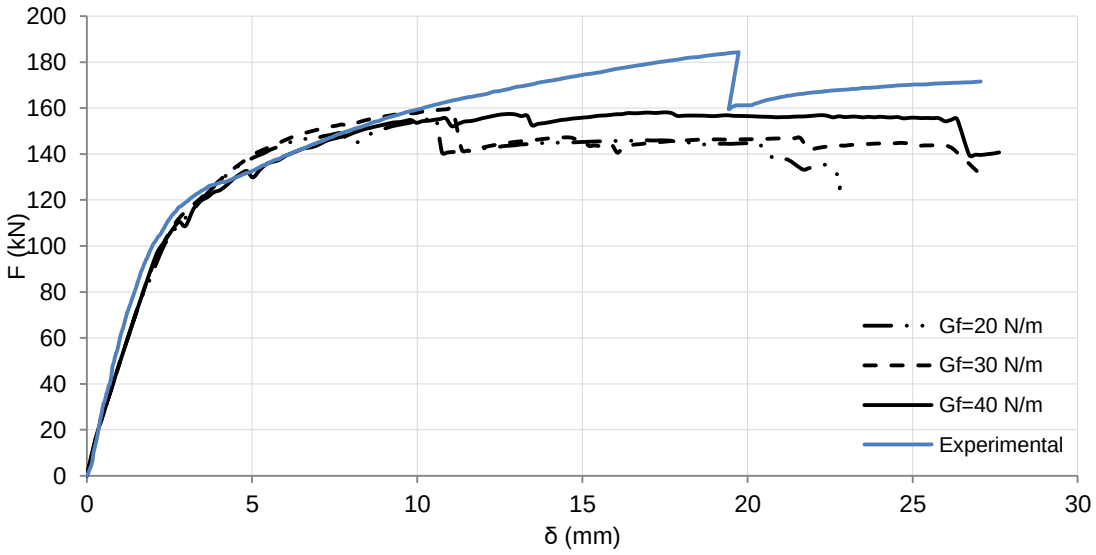

Figure 86. Load-displacement graph for different values of tensile fracture energy.

4.4.2 Influence of interface friction angle

Three different values of stiffness were adopted for the purpose of this study 0.55, 0.75 and 1. The results are presented in Figure 87, Figure 88, Figure 89 and Figure 90. The damage pattern of the model is significantly influenced by the value of the friction angle. For a relatively low value of φ=0.55 rad the piers are failing in shear before the spandrel panel, while for φ=1 the diagonal cracking in the spandrel is not obtained exactly in the middle of the panel. For the initial adopted value of φ=0.75 the cracking pattern has a satisfying correspondence to the experimental case.

The force-displacement graph is also influenced by the friction angle value in terms of ductility, although the maximum capacity remains in the same range as before.

These results are showing that the friction angle should be varied within the range of 0.55 and 1.00, with the initial value of 0.75 giving a satisfying damage pattern.

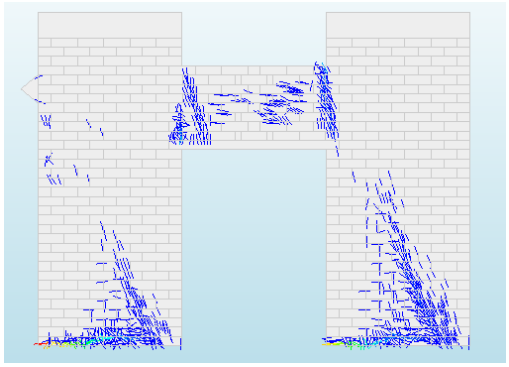

Figure 87. Damage pattern for φ=0.55, d=9.04 mm

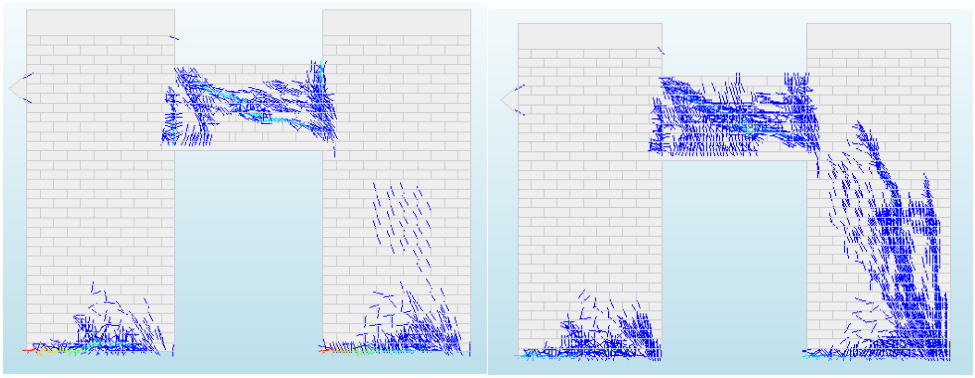

Figure 88. Damage pattern for φ=0.75 (a) d=10.92 mm (b) d=22.79 mm

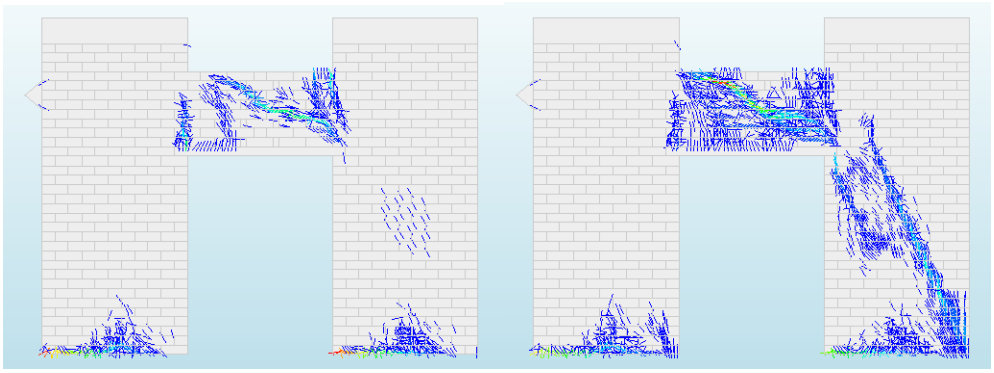

Figure 89. Damage pattern for φ=1.00 (a) d= 8.4 mm (b) d= 20.6 mm

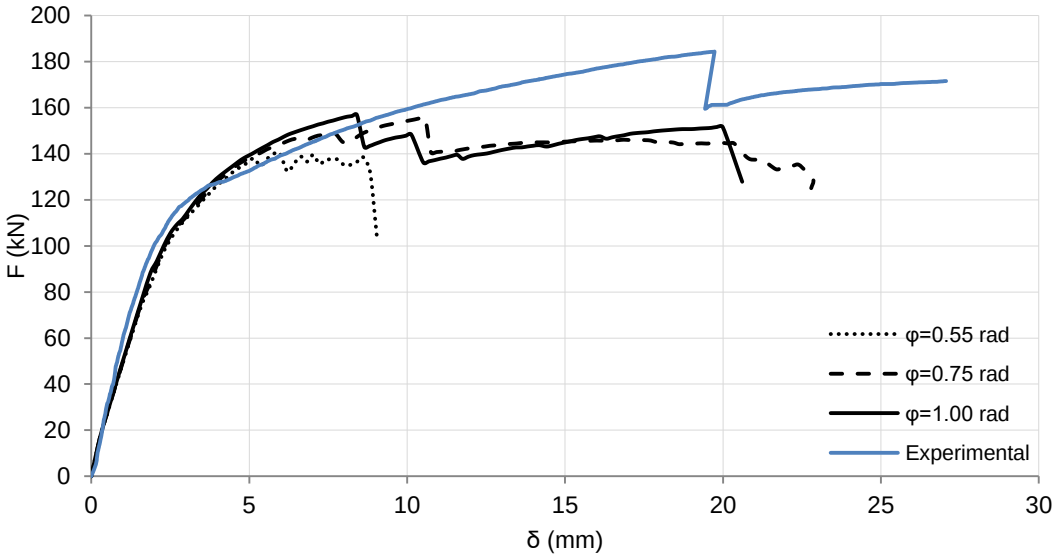

Figure 90. Load-displacement graph for different values of friction angle

4.4.3 Influence of interface cohesion

The influence of the interface cohesion was examined by three different analyses with cohesion values of 0.146, 0.345 and 0.5. The results are presented in Figure 91, Figure 92, Figure 93 and Figure 94.

As it is observed the influence of the cohesion value is negligible, in terms of both damage pattern and force-displacement graph. Therefore a value between the range of 0.146 and 0.5 should be adequate for the purpose of this approach.

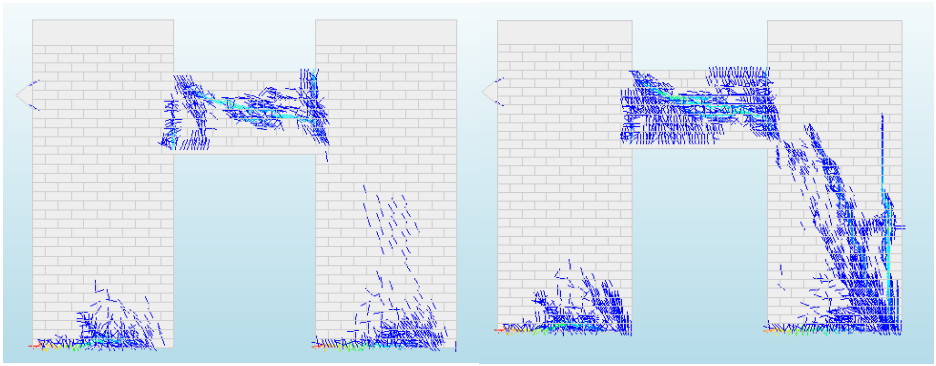

Figure 91. Damage contour for c=0.146 (a) d= 9.35 mm (b) d=23.18 mm

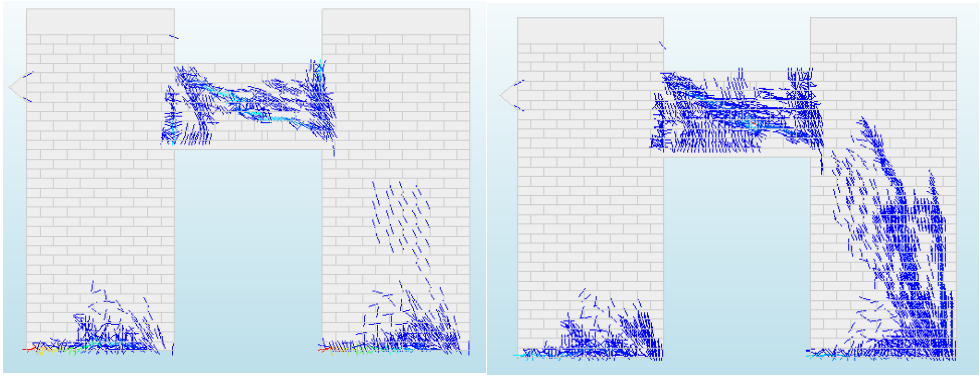

Figure 92. Damage contour for c=0.345 (a) d=10.92 mm (b) d=22.79 mm

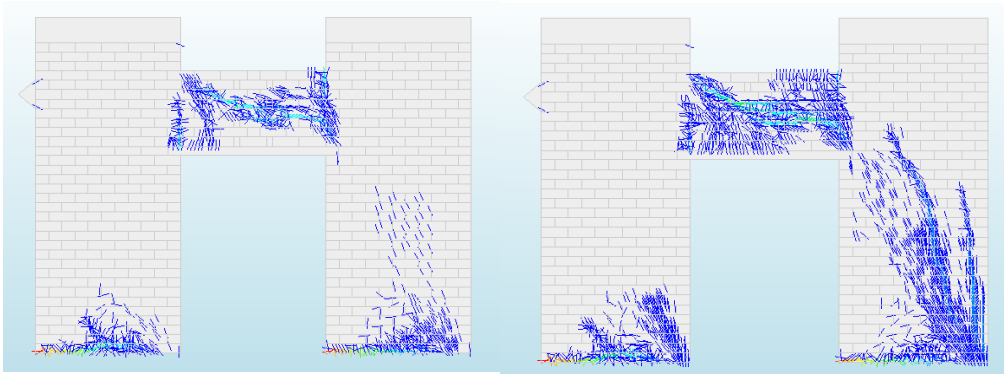

Figure 93. Damage contour for c=0.5 (a) d= 10.38 mm (b) d=30 mm

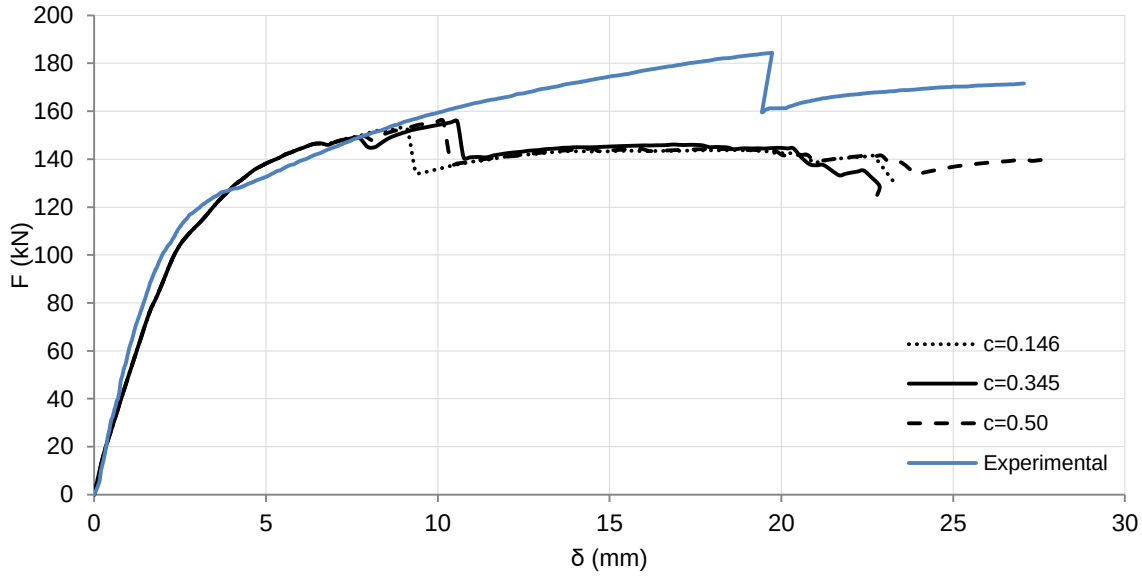

Figure 94 Force-displacement graph for different values of interface cohesion.

4.4.4 Influence of interface stiffness

The influence of the interface stiffness was examined by three different analyses. The different values of interface stiffness are presented in Table 17. The results are presented in Figure 95, Figure 96, Figure 97 and Figure 98.

It is observed that for much lower values of interface stiffness the crack pattern is significantly modified and the overall model capacity is significantly reduced. For the case of Analysis 2 and 3 similar behavior is observed with a small decrease of ductility and overall stiffness in case of Analysis 3 as well as a less diffused crack pattern.

Table 17. Analysis input for investigation of interface stiffness influence

Analysis	kn (N/m^3)	kt (N/m^3)
1	1.17E+12	1.36E+10
2	1.17E+13	1.36E+11
3	6.17E+13	1.36E+12

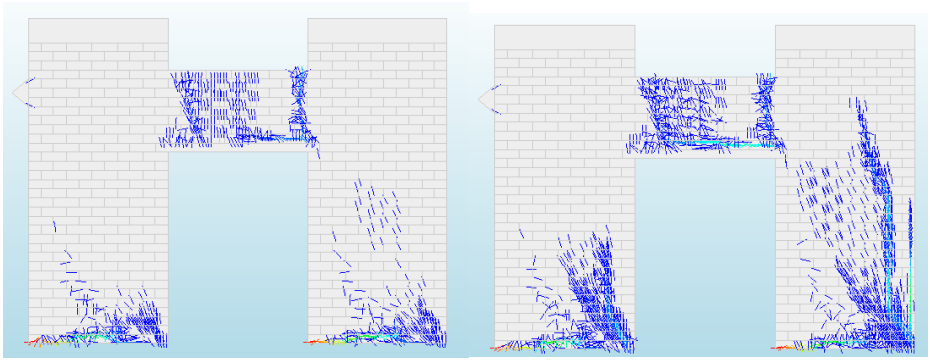

Figure 95. Damage contour for Analysis 1(a) d=17.1 mm (b) d=28 mm

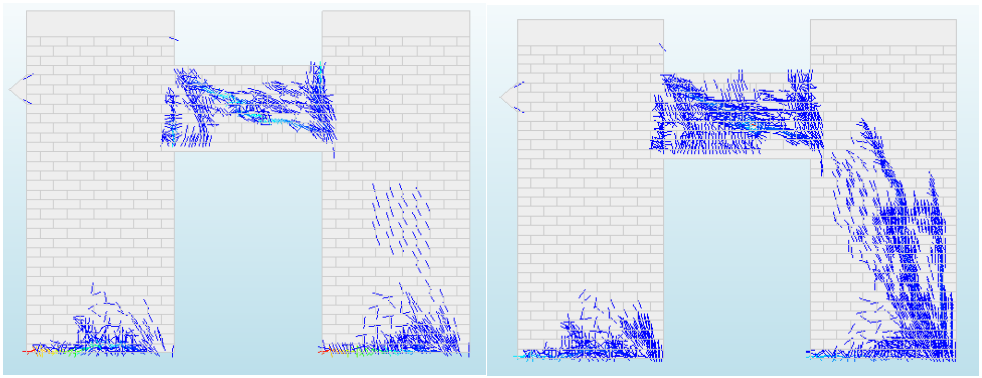

Figure 96. Damage contour for Analysis 2(a) d=10.92 mm (b) d=22.79 mm

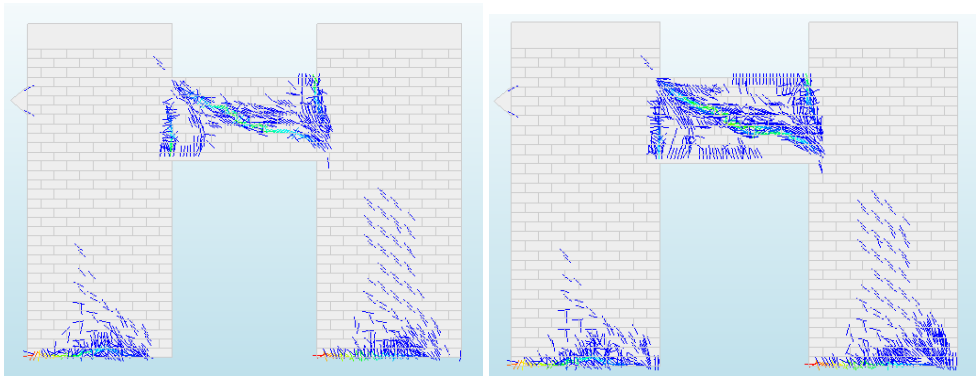

Figure 97. Damage contour for Analysis 3(a) d=7.87 mm (b) d=17.9 mm

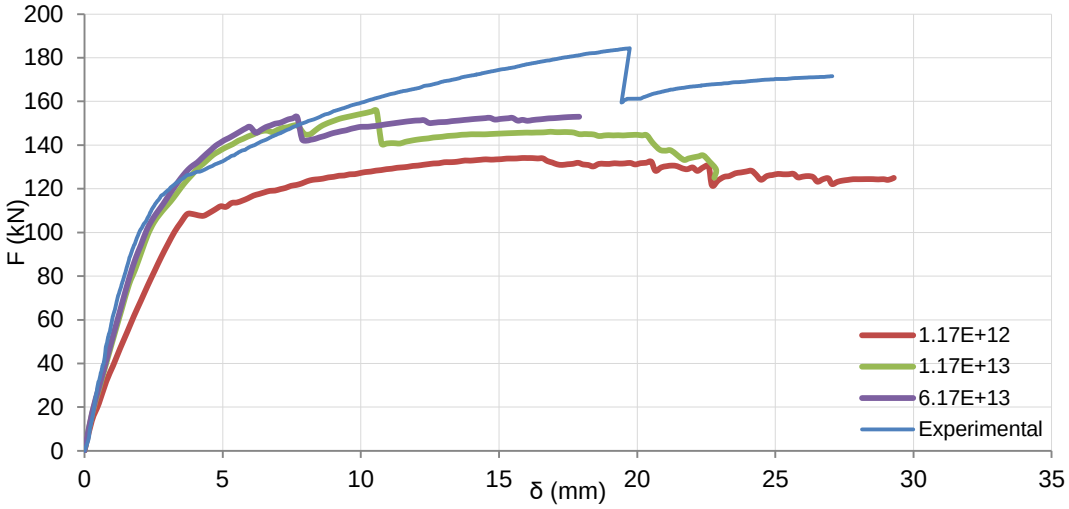

Figure 98. Force-displacement graph for different values of interface stiffness.

4.5 Comparison with macromodel

In order to evaluate the validity of this micromodelling approach, a comparison is attempted with the macromodel described in chapter 3. The mechanical properties of this model is presented in Table 18 and Table 19. Those values were selected taking into account the results of the parametric study described in section 4.4. This comparison is presented in Figure 99, Figure 100 and Figure 101.

Regarding the damage pattern both models are obtaining a satisfying representation of the damage observed in the experiment. The micromodel is though form a more diffused crack pattern than the macromodel.

In terms of capacity the micromodel is resulting to a more realistic representation in the beginning of the nonlinear region. Nevertheless the early shear failure of the spandrel panel (for d=12.18) is affecting the model's capacity, which is equal to 162.58 kN, 11.6% lower than the experimental one and 4.89% lower than the macromodel's.

Table 18. Mechanical prperties of tuff stone component

E	v	ρ	f_c	G_c	f_t	G_f
GPa	-	kg/m^3	MPa	N/m	MPa	N/m
1540	0.2	1172	4.13	20000	0.23	30

Table 19. Mechanical properties of unit-mortar interface

k_n	k_t	c	φ	ψ
N/m^3	N/m^3	N/m^2	rad	rad
4.17E+13	4.35E+11	0.5	0.9	0.01

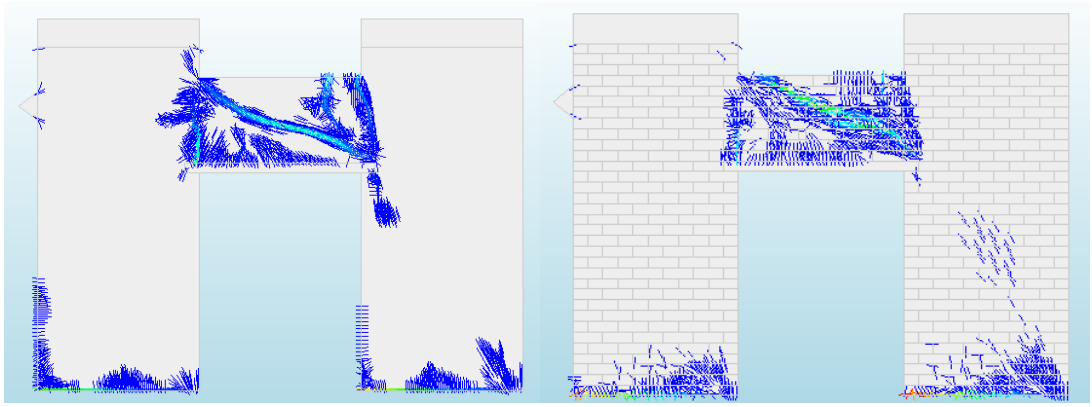

Figure 99 Damage pattern for (a) macromodelling and (b) micromodelling approach

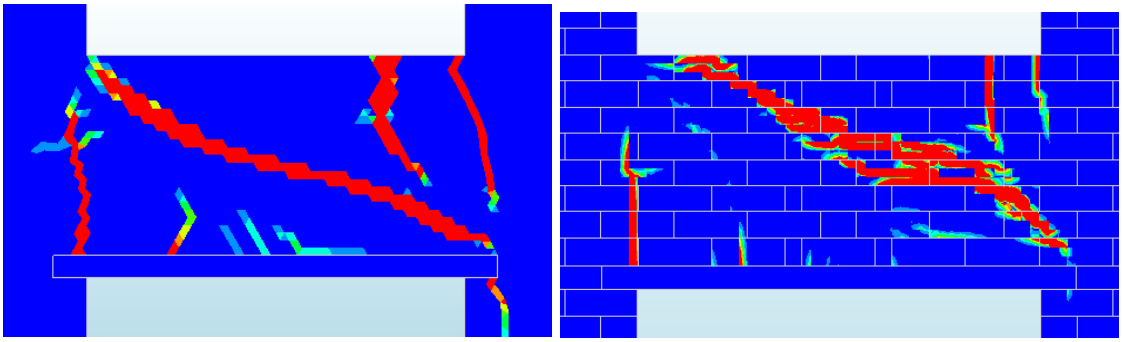

Figure 100. Principal strain contour for spandrel panel of (a) macromodelling and (b) micromodelling approach

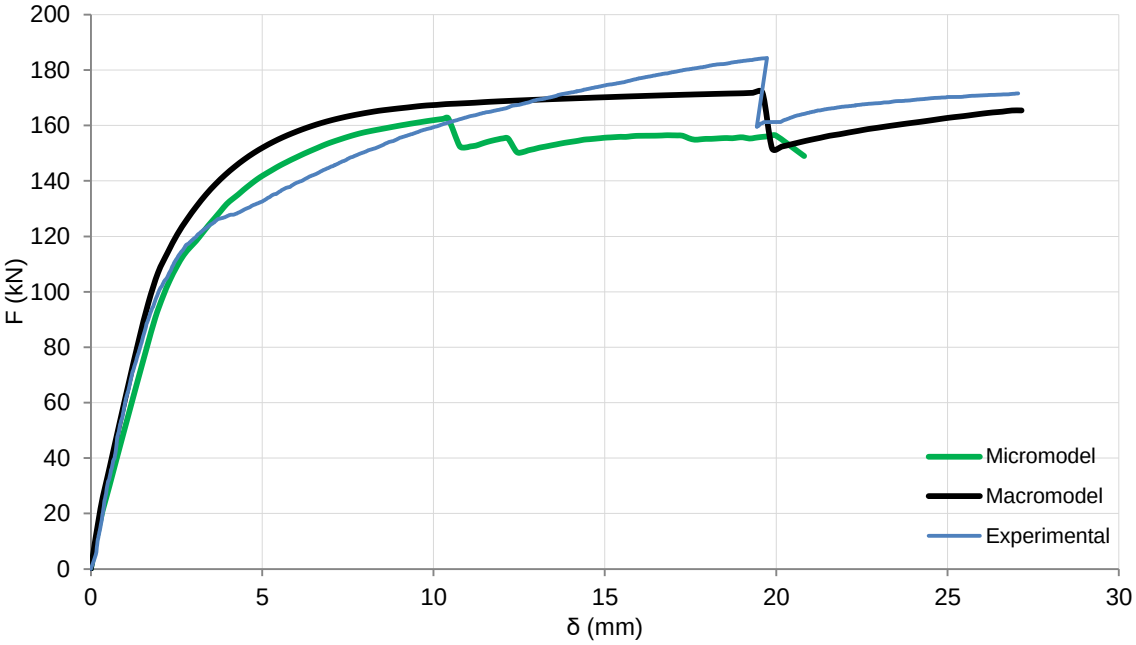

Figure 101. Force-dispalcement graph for the different modelling approaches.

4.6 Conclusions

This attempt of a micromodel development provided a series of valuable conclusions:

- The micromodelling approach is giving satisfying results regarding the damage pattern of portal frames. Nevertheless a diffused crack pattern is also obtained as in the macromodelling technique.
- The force-displacement diagram was not able to be defined properly, due to the shear failure of the masonry spandrel for a lower horizontal displacement than the experimental case. This drawback could not be overcome due to the limited number of parametric analysis, which did not allow to define properly the influence of all the material properties used for the model.
- The computational cost of the micromodelling approach as well as the need for definition of a large number of material properties is making its application extremely difficult and time demanding.
- Besides its drawbacks a calibrated micromodel can provide very accurate results for the behavior of masonry façades. Further investigation and research should be executed to overcome the difficulties of its application.

5. APPLICATION OF THE MACROMODEL TO A NEW TEST

Taking into account the conclusions of chapter 3 it was revealed that the macromodelling FE approach consisted of an efficient and reliable tool for the evaluation of the in-plane strength and behavior of masonry façades.

Due to its successful application on the benchmark problem of the Napoli University experiment, the numerical model was applied to the case of an ongoing experimental campaign taking place at the Technical University of Catalonia (UPC). The geometry characteristics, as well as the material properties, have been supplied to the student by UPC members.

The investigation in UPC is still in its design phase and changes in its geometry and setup conditions may still be done. Therefore, the application of the numerical model created for the current thesis study is useful to validate the current planned solution. Particularly, the model will help to estimate the expected damage pattern and check whether the maximum horizontal load capacity of the tested specimen is attainable for the facilities of the laboratory.

5.1 Characteristics of the new test

5.1.1 Geometry

The geometry of the specimen to be built and tested in UPC was designed in order to fit in the conditions of the laboratory, namely a maximum free height of 4.7 m and the fixed distribution of anchorage holes in the strong floor, placed every 0.8 m.

The masonry bond pattern was set as Flemish bond, given that it is quite common in buildings of Barcelona and it has not been studied yet by other researchers. Both vertical and horizontal mortar joints were set as to be 15 mm thick, in order to accommodate easily the irregularities found in the selected bricks.

The adopted geometry of the portal frame is shown in Figure 102.

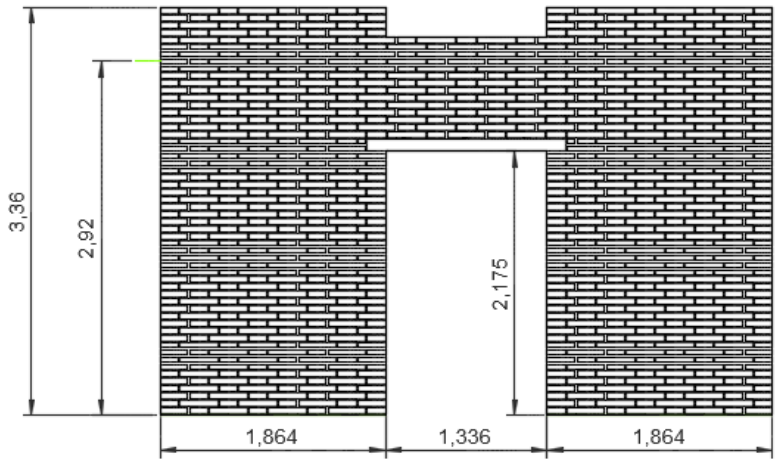

Figure 102. New adopted geometry for the research in UPC.

5.1.2 Test set-up

Based on the tests of Augenti et al. (2011) and Knox (2012), which consisted of full portal frame structures, the setup planned at UPC allows the application of a cyclic horizontal load, which simulates the seismic action, by means of an hydraulic actuator that reacts against a concrete wall. The weight of upper floors is simulated by the action of two jacks reacting against two steel frames. Figure 103 illustrates all these elements.

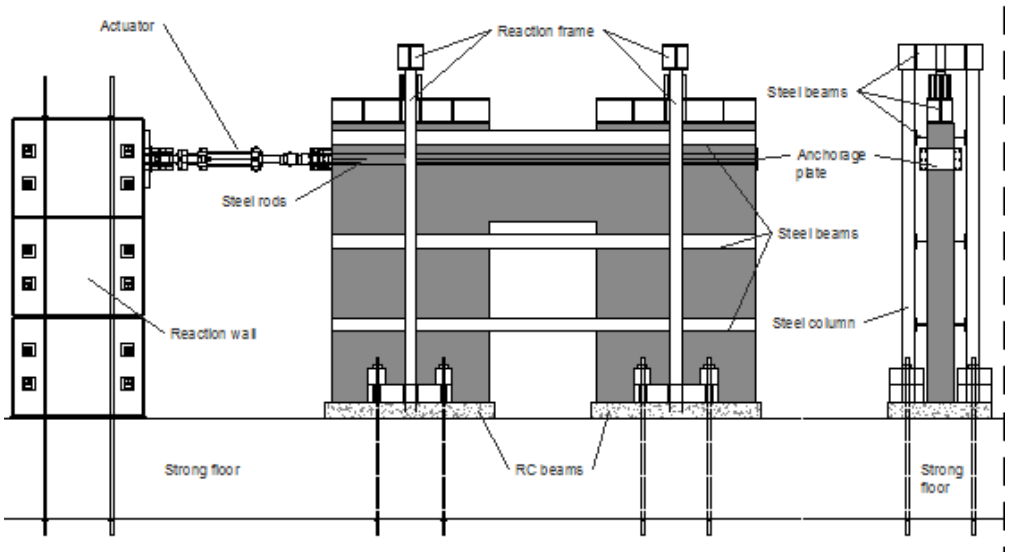

Figure 103. Setup of the test planned at UPC

Given the designed setup, the following information is of relevance for the numerical analysis:

The vertical load applied to each pier is of 123 kN, which leads to stress at the bottom of the piers of approximately 0.3 MPa; this is value is considered to be representative of a 3 floor building.

The point of application of the horizontal load is centered at a height of 2.92 m from the bottom of the masonry pier.

The hydraulic actuator is able to push 350 kN and to pull 240 kN. So that, this latter value is a limiting condition for the test. This is an objective for the analysis of this thesis: check if the maximum capacity of the specimen is lower than those 240 kN.

5.1.3 Material properties

One of the features of the ongoing investigation at UPC is trying to reproduce conditions found in real structures. In this sense, a special effort has been made in order to find materials having mechanical properties typical of historical constructions of the Mediterranean basin.

Handmade clay bricks have been selected from a local company that keeps the traditional production system. These bricks have nominal dimensions of 311 x 149 x 45 mm. Applying the standard EN 772-1, the normalized compressive strength is of about 20 MPa.

With regard to the mortar, a previous research was made in order to find a mortar with a compressive strength not higher than 2 MPa, according to the EN 459-2. A commercial premixed mortar, based on hydraulic lime, was selected and mixed with different amounts of limestone filler. At the end, the selected mix offers a compressive strength of 1.9 MPa.

Additional tests have been performed to characterize the mechanical properties of the composite material. A summary of these tests and properties is shown in Table 20.

Table 20. Summary of tests and material properties for the masonry used in UPC

<table>
<tr><td colspan="2">Test: Compressive strength perpendicular to bed joints</td><td rowspan="4">  </td></tr>
<tr><td colspan="2">Standard: EN 1052-1</td></tr>
<tr><td>fc (MPa)</td><td>6.51</td></tr>
<tr><td>E (MPa)</td><td>3419.7</td></tr>
<tr><td colspan="2">Test: Initial shear strength - Triplets</td><td rowspan="4">  </td></tr>
<tr><td colspan="2">Standard: EN 1052-3</td></tr>
<tr><td>c (MPa)</td><td>0.176</td></tr>
<tr><td>μ</td><td>0.643</td></tr>
<tr><td colspan="2">Test: Diagonal tensile strength</td><td rowspan="4">  </td></tr>
<tr><td colspan="2">Standard: RILEM LUM B6</td></tr>
<tr><td>ftd (MPa)*</td><td>0.211</td></tr>
<tr><td colspan="2">*Preliminary value, campaign still under completion</td></tr>
</table>

5.2 Numerical Analysis

In order to adjust the numerical model that was created for the purpose of the current study to the UPC experimental case, several changes have to be made.

The parameters that were kept the same were first of all the mesh type, size element as well as the numerical solution method (step size, iteration method, convergence criteria). More specifically the mesh size was set to 4 cm of triangular 3-node elements based on linear interpolation (T6MEM elements). Regarding the iteration method, displacement control was applied with a step size of 0.01 (maximum horizontal displacement of 0.03 m), with the application of regular Newton-Raphson method and convergence criterion equal to 0.01.

The material models that were used, was Total Stain Based Crack model (rotational) for the masonry component and linear elastic model for the timber lintel. The material properties of the timber lintel were kept the same as the previous application (section 3.4.3.1). More specifically:

Young's Modulus E=12 GPa

Poisson's ratio v=0.15

Density ρ=800 kg/m^3

The input parameters for the masonry component were based in the values that were obtained in the experiments described in section 5.1.3. The elastic parameters as well as the value of the compressive strength were kept constant (Table 20). Different values were given to the tensile strength in order to obtain a wide range of possible mechanisms for the model. As it was concluded from the parametric analysis in section 3.4.2, the tensile strength can modify significantly the damage mechanism as well as the deformability of the model. As far as the tensile fracture energy is concerned, due to the uncertainties that are involved to its calculation, it was considered to keep the same ratio between tensile strength and tensile fracture energy as the calibrated macromodell. That way a tensile "ductility" was introduced equal to

$$d_t = \frac{G_t}{f_t} = 0.1152\ mm \tag{45}$$

The same concept was applied also for the compressive fracture energy where its value was obtained from the Mode Code 90 equation, and then it was increased approximately 50% to avoid brittle damage of certain areas of the model.

The material properties of the new geometry model (besides f_t and G_f) are illustrated in Table 21.

Table 21. Mechanical properties input for masonry component.

E	v	ρ	f_c	G_c
GPa	-	kg/m^3	MPa	N/m
3419	0.27	1670	6.51	27653

Finally regarding the interface between timber and masonry, the new model adopted the same configuration as the previous one, with two different interfaces for the lintel and the lintel's anchorage length. The values of cohesion, friction and dilatancy angle were kept constant, while the normal and shear stiffness of both interfaces were given different values, since they were proved to be the most influential parameters due to the sensitivity analysis in section 3.4.3.2.

In the first phase a parametric analysis was carried out with different combinations of tensile strength and interface stiffness. The results of this phase are described below.

5.2.1 Parametric analysis

5.2.1.1 Influence of tensile strength

In this section the result of three analysis with different values of tensile strength is presented. More specifically the values of 0.126, 0.168 and 0.211 MPa were adopted. The value of 0.211 MPa was obtained by the diagonal compression tests that were described in section 3.2.2. Since the previous model was calibrated for tensile strength lower than the one obtained from diagonal compressive tests, two more different values of 0.126 and 0.168 MPa were chosen. The results are illustrated in Figure 104, Figure 105, Figure 106 and Figure 107. The tensile strength is affecting significantly the damage mechanism of the model. In all the models flexural cracks are forming in the base of the piers as well as the end corners of the spandrel. For higher horizontal displacements in all three models a horizontal crack is forming in the left pier, starting from the spandrel and ending to the actuator on the left side of the specimen. The value of the tensile strength is strongly affecting the damage mechanism of the spandrel. More specifically in the case of f_t=0.126 MPa the horizontal crack in the left pier is forming after the diagonal shear failure of the spandrel. In the case of f_t=0.168 MPa this horizontal crack is forming simultaneously with the diagonal crack in the spandrel. Nevertheless the right pier is failing first, not letting the shear crack to fully form. In case of f_t =0.211 MPa the horizontal crack is forming for even lower displacement and it is propagating until the right pier fail in shear, without the forming of any crack in the spandrel panel.

As far as the force-displacement graph is concerned, it is observed a negligible change in the force capacity. It should be also noted that the maximum force capacity didn't exceed the value of 250 kN, which is the maximum capacity of the actuator that is going to be used.

These analyses showed that the tensile strength is a factor influencing in a considerable way the damage mechanism of masonry façades. Therefore the definition of a value for the tensile strength of the masonry as a composite material is very important for the understanding of the spandrel's behavior due to in-plane seismic loads.

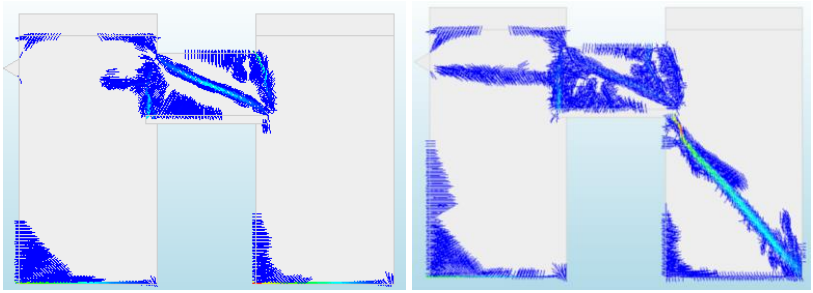

Figure 104. ft=0.126 MPa Damage contour for (a) d=5.7cm (b) d=23.1 mm.

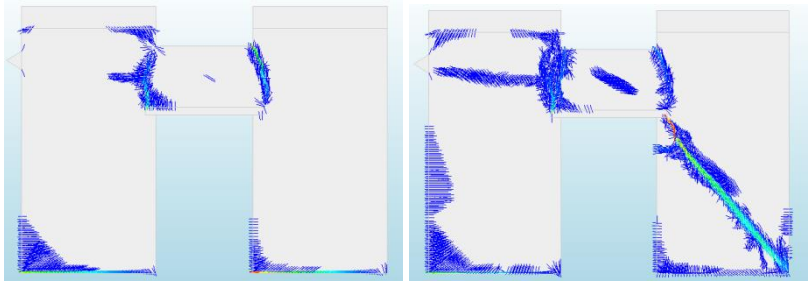

Figure 105 ft=0.168 MPa Damage contour for (a) d=5.7cm (b) d=24.9 mm.

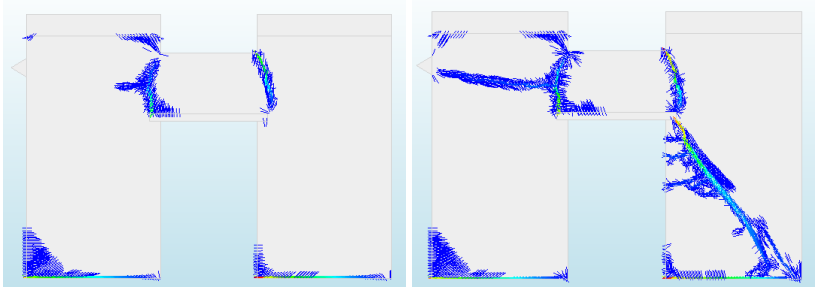

Figure 106 ft=0.211 MPa Damage contour for (a) d=2.8cm (b) d=27.3 mm.

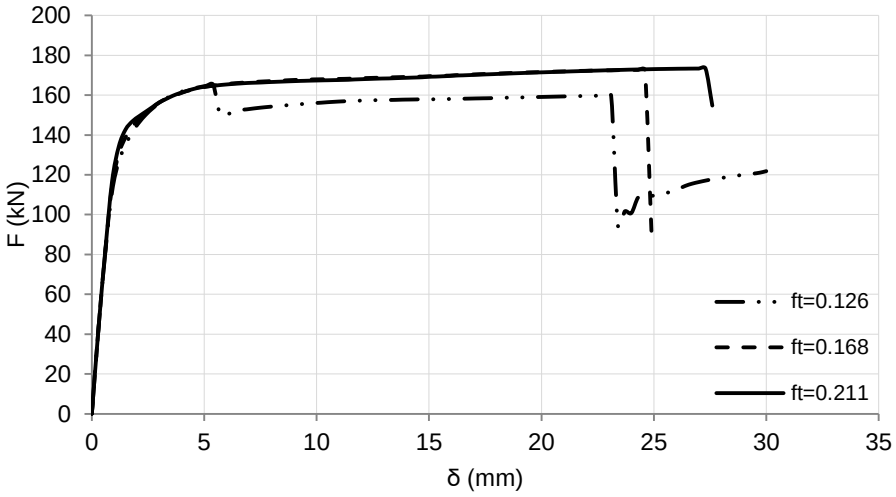

Figure 107 Force-displacement graphs for different values of tensile strength

5.2.1.2 Influence of interface stiffness

The sensitivity analysis that was done in section 3.4.2 showed that the stiffness of the interface between timber lintel and masonry is extremely influential for the overall model behavior. A combination of analysis with three different values for tensile strength as well as three different values for the interface stiffness was executed. The different combinations are presented in Table 22.

Table 22. Analysis combination

	ft=0.126	ft=0.168	ft=0.211
kn=4.28	A1	B1	C1
kn=6.28	A2	B2	C2
kn=8.28	A3	B3	C3

Case ft=0.126 MPa

The results are illustrated in Figure 108, Figure 109, Figure 110 and Figure 111. It is observed a negligible influence of the interface stiffness for the maximum strength capacity as well as the damage pattern. The only thing influenced by the value of the interface stiffness is the ductility of the model, which is increasing for lower values. Nevertheless the overall behavior did not changed significantly.

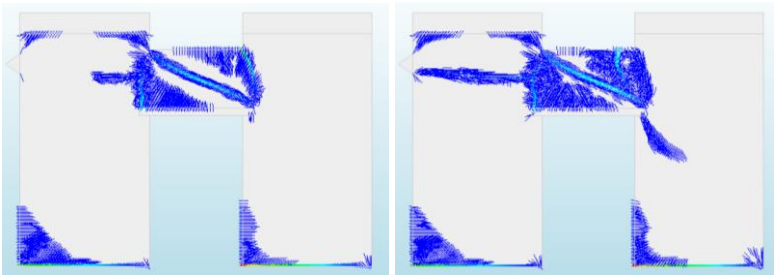

Figure 108. $k_{n,t}$=4.28e8 N/m^3 Damage contour for (a) d=6.6cm (b) d=30 mm

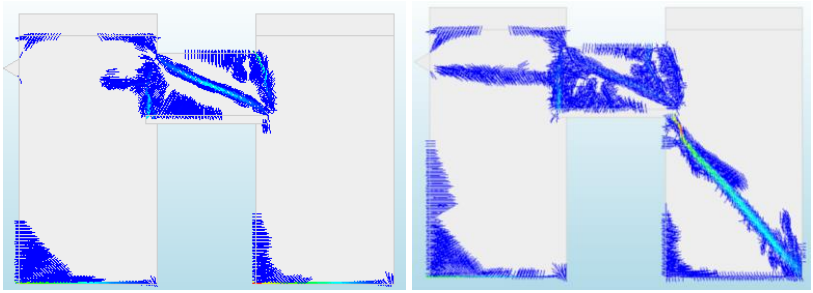

Figure 109 $k_{n,t}$=6.28e8 N/m^3 Damage contour for (a) d=5.7cm (b) d=23.1 mm

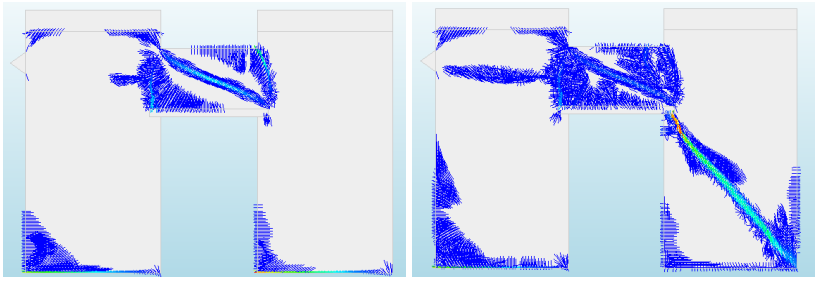

Figure 110 $k_{n,t}$=8.28e8 N/m^3 Damage contour for (a) d=5.4cm (b) d=30 mm

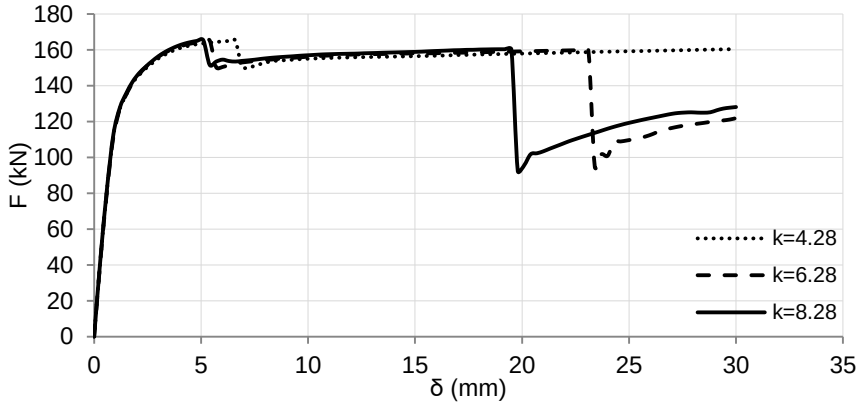

Figure 111. Force-displacement graphs for different values of interface stiffness

Case ft=0.168 MPa

The results are illustrated in Figure 112, Figure 113, Figure 114 and Figure 115. Similar to the previous case the model behavior did not get influenced by the variation of the interface stiffness. The only change occurred was the variation of the displacement for which the diagonal crack is formed in the spandrel as well as the overall ductility. In every case the horizontal case in the left pier started to form, absorbing energy through its propagation and therefore not letting the spandrel to fail in shear.

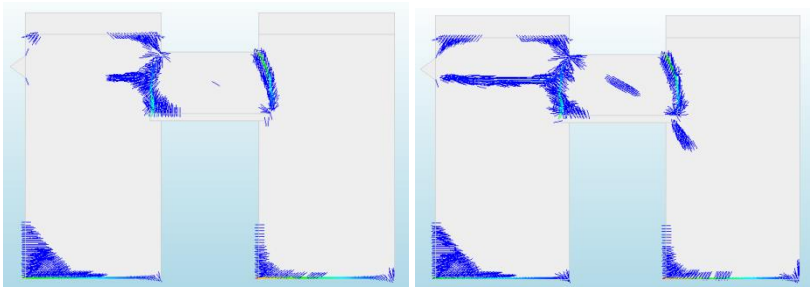

Figure 112 $k_{n,t}$=4.28e8 N/m^3 Damage contour for (a) d=6.9cm (b) d=30 mm

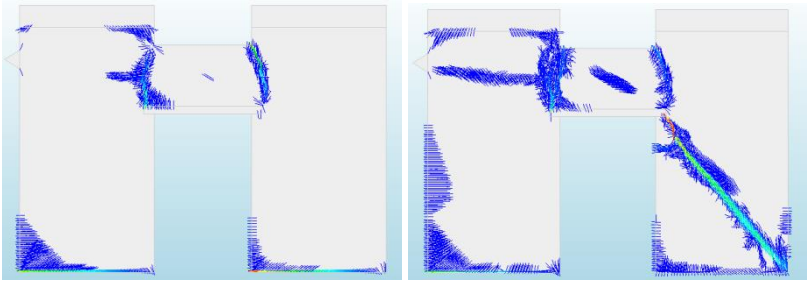

Figure 113 $k_{n,t}$=6.28e8 N/m^3 Damage contour for (a) d=5.7cm (b) d=24.9 mm

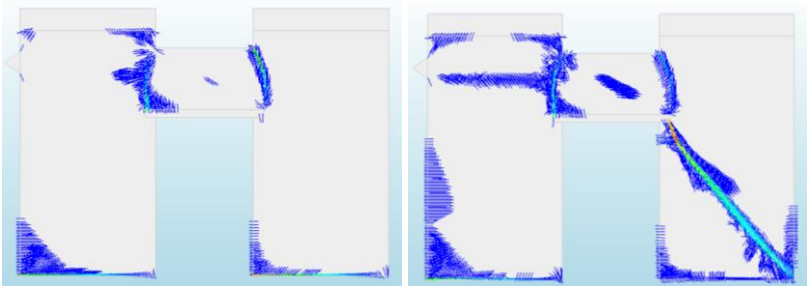

Figure 114 $k_{n,t}$=8.28e8 N/m^3 Damage contour for (a) d=5.1cm (b) d=19.5 mm

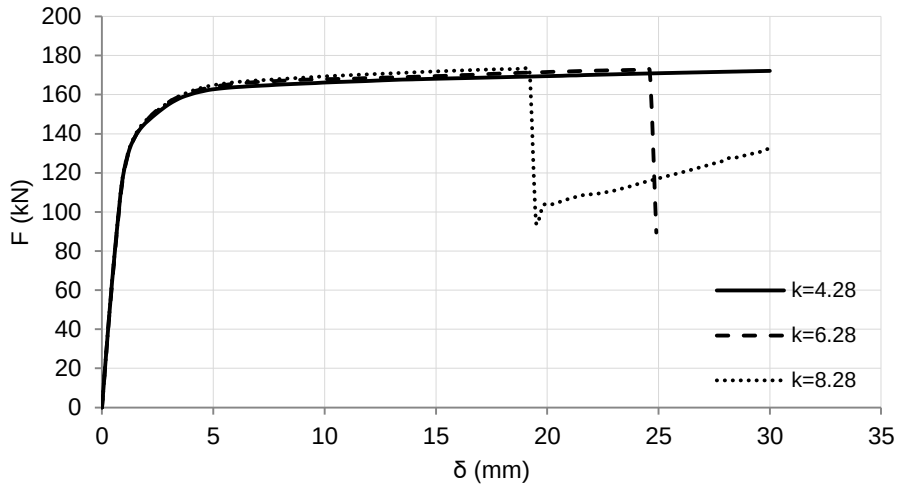

Figure 115 Force-displacement graphs for different values of interface stiffness

Case f_t=0.211 MPa

The results are illustrated in Figure 116, Figure 117, Figure 118 and Figure 119. Once again the model behavior did not get influenced by the variation of the interface stiffness. In every case the horizontal case in the left pier started to formed, absorbing energy through its propagation and therefore not letting the spandrel to fail in shear. The overall ductility also changed for difference values of stiffness.

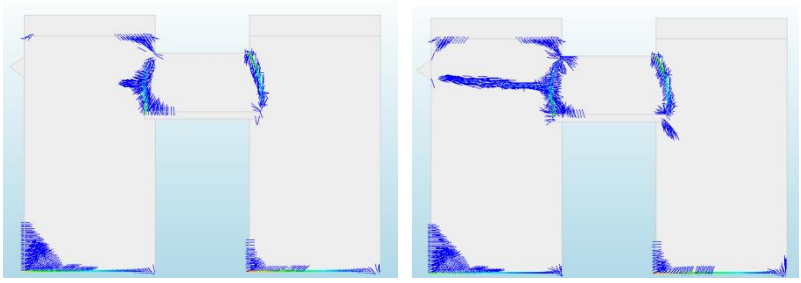

Figure 116 $k_{n,t}$=4.28e8 N/m^3 Damage contour for (a) d=5.1 cm (b) d=30 mm

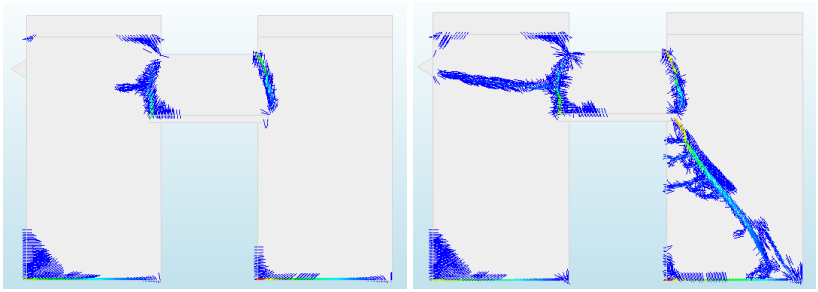

Figure 117 $k_{n,t}$=6.28e8 N/m^3 Damage contour for (a) d=5.1 cm (b) d=27.3 mm

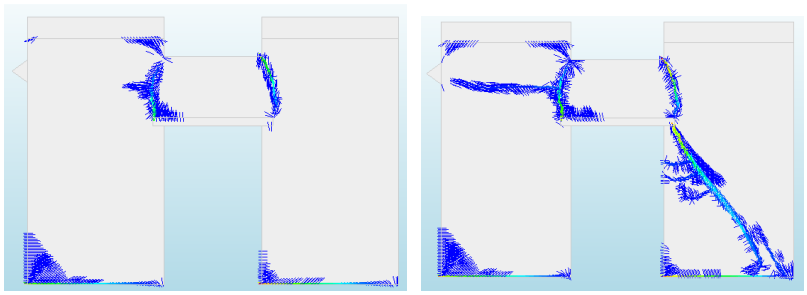

Figure 118 $k_{n,t}$=8.28e8 N/m^3 Damage contour for (a) d=5.1cm (b) d=21.3 mm

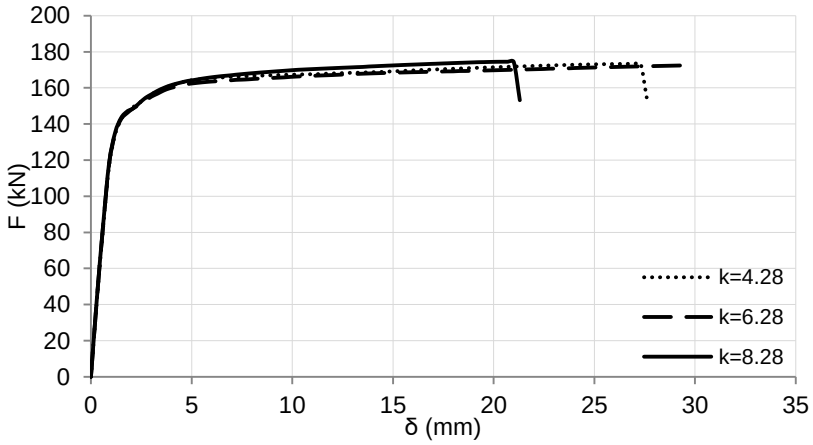

Figure 119. Force-displacement graphs for different values of interface stiffness

5.3 Additional verifications

5.3.1 Comparison with the experiment of University of Napoli

The parametric analysis described above presented an undesirable damage mechanism for the numerical model. The horizontal crack that was obtained in the left is a damage that is not observed in real structure. Also it absorbs a significant amount of energy and therefore the spandrel is not able to fail in shear. The shear failure of the spandrel is extremely important for the evaluation of the maximum strength of masonry spandrels, therefore a further investigation was executed in order to estimate whether this horizontal crack is based on real conditions and it is affected by the geometry, or the material properties, or it is based on a possible drawback of the model.

An initial investigation contained the comparison with the experimental campaign in the University of Napoli. For this purpose two different analyses were executed:

Analysis 1: UPC geometry-Napoli material properties

Analysis 2:Napoli geometry-UPC material properties

The masonry material properties for Analysis 2 were 0.168 MPa for the tensile strength and 6.21e8 N/m^3 for the interface stiffness. Those values were selected, because they resulted to a damage where both shear and horizontal crack were formed in the model.

The results of those analyses are illustrated in Figure 120 and Figure 121. In the case of Analysis 1 the spandrel failed in shear before the horizontal crack get formed in the left pier. This is justified by the lower values of tensile strength (0.1215 MPa) which allowed the spandrel to reach its maximum capacity before the propagation of the horizontal crack. In the case of Analysis 2 the results did not changed comparing to those where the UPC geometry was applied (Figure 121). This led to the conclusion that the damage mechanism is not affected significantly by minor variation of the model's geometry, but for variations of material properties.

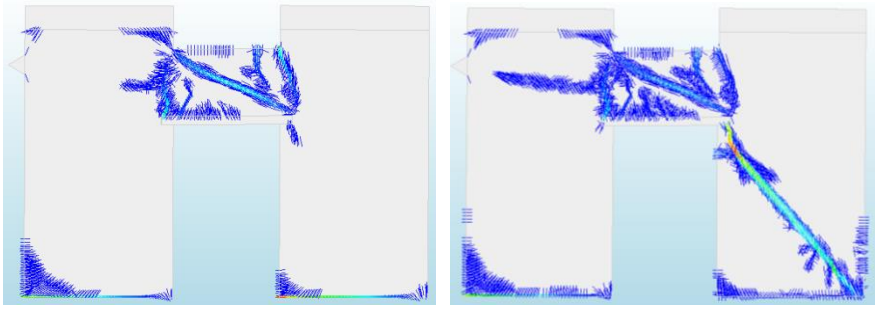

Figure 120 Analysis 1. Damage contour for (a) d=11.1 mm (b) d=23.4 mm

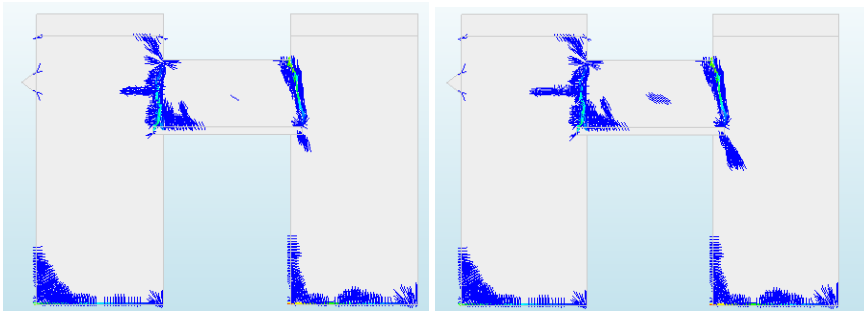

Figure 121 Analysis 2. Damage contour for (a) d=24.3 mm (b) d=30 mm

5.3.2 Influence of pier vertical load

The vertical loading of the piers is proved to influence significantly the behavior of masonry spandrels (section 2.1.2). An increase of the pier compressive load from 123 kN to 150 kN was executed in order to observe the differentiation of the model's behavior. The tensile strength was set to 0.168 MPa, while the interface stiffness to 6.21e8 N/m3. The results are illustrated in Figure 122 and Figure 123. In the adopted model the shear cracking in the spandrel start to form and propagate simultaneously with the horizontal crack in the left pier. Nevertheless the increasing vertical loading of the piers has as a result, the shear failure of the spandrel. Another difference is the increase of the model's ductility, since the right pier is not collapsing for the maximum displacement of 30 mm, while in the case of vertical loading equal to 123 kN, the right pier fails for d=24.9 mm. Another important difference is the increase of the load capacity from 172.63 kN to 194.02 kN. Although the maximum capacity is increasing, it is not exceeding the maximum capacity of 250 kN of the laboratory actuator. It should be pointed out that in the case of the Napoli experiment the numerical model estimated a maximum capacity 6.8% lower than the experimental one. Therefore adjusting the value obtained from this analysis a maximum capacity of 208.17 kN is obtained, which also in this case is not exceeding the safety limit of 250 kN.

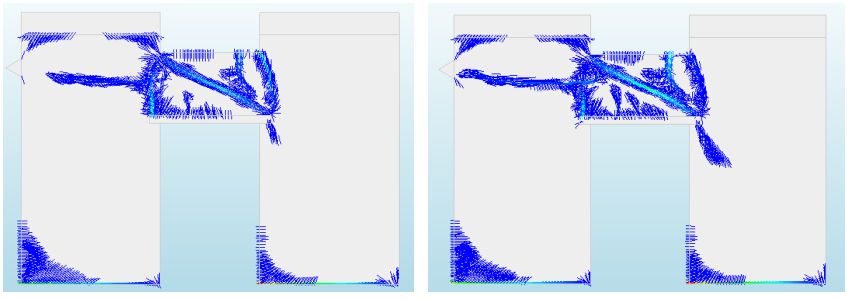

Figure 122 Damage pattern for pier compressive load of 150 kN (a) d=15.3 mm (b) d=30 mm

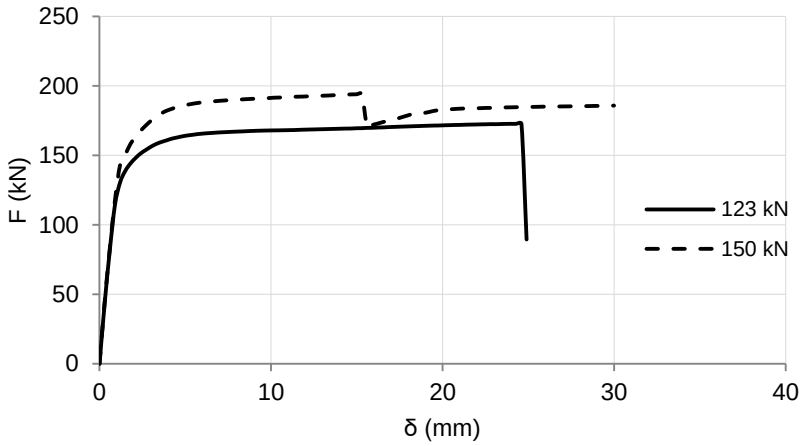

Figure 123. **Force-displacement graphs for different values of pier compressive load**

5.3.3 Influence of timber lintel length

Previous experimental campaigns (Graziotti 2014, Beyer 2012) have pointed out the importance of the lintel geometry and type to the behavior of masonry spandrels.

Two different analysis were executed with the same masonry material properties (f_t=0.168 MPa, $k_{n,t}$=6.21e8 N/m^3) and different anchorage length for the timber lintel:15 and 30 cm. The results are illustrated in Figure 124 and Figure 125. Comparing the damage pattern with the one obtained for timber llintel with anchorage length 15 cm (Figure 105), few changes can be observed. The flexural cracks in the spandrel panel are strongly influenced by the anchorage length in terms of generation point and direction. Regarding the model behavior the maximum strength capacity remains the same, while the deformability is strongly affected. In the case of higher anchorage length for the lintel, the right pier is failing in shear for much lower horizontal displacement (10.2 mm instead of 24.9 mm). Nevertheless the increase of the length of the lintel did not prevent the forming of the horizontal crack in the left pier, neither allowed the shear failure of the spandrel.

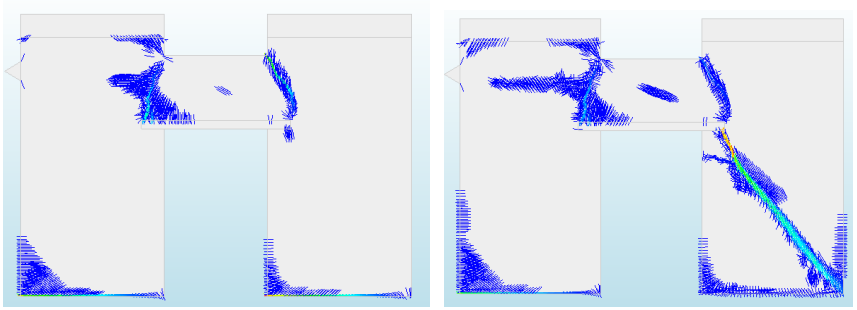

Figure 124 Lintel anchorage length 30 cm. Damage contour for (a) d=5.4 mm (b) d=10.2 mm

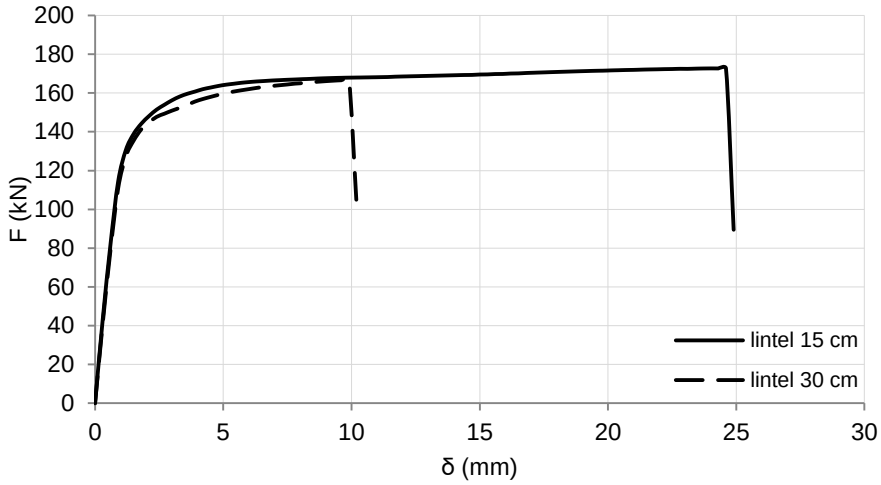

Figure 125. **Force-displacement graphs for different values of lintel anchorage length**

5.3.4 Effect of load application

The analyses that were described in the previous section revealed the negative impact of the generation of the horizontal crack in the left pier to the model's behavior. This crack was in every case initiated in the left area of the spandrel panel and was directing towards the load actuator. This observation led to the decision of further investigation of the load application and its influence on the numerical model. In order to understand whether the horizontal crack is formed due to inadequate application of the horizontal load, different configurations for the actuator were adopted.

Three different length values for the load application length were tried 24, 44 and 88 cm. The results are presented in Figure 126, Figure 127, Figure 128 and Figure 129. The results are showing a negligible influence of the load application length in both damage pattern and force-displacement relationship. The only minor change that could be considered is the direction of the horizontal crack in the left pier, which is always heading towards the lower edge of the triangular element representing the actuator.

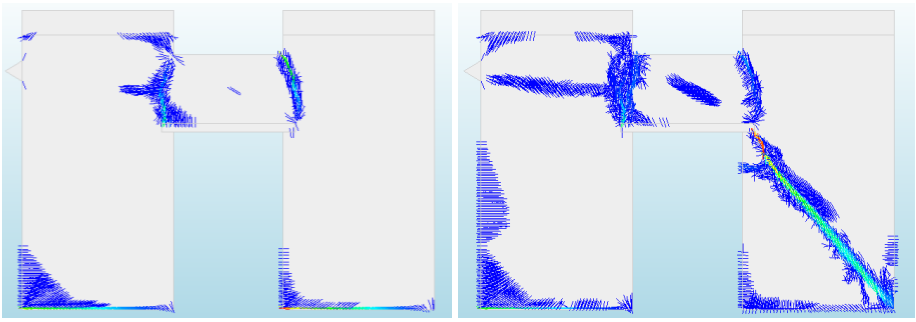

Figure 126. **Load application length 24 cm Damage contour for (a) d=5.7cm (b) d=24.9 mm**

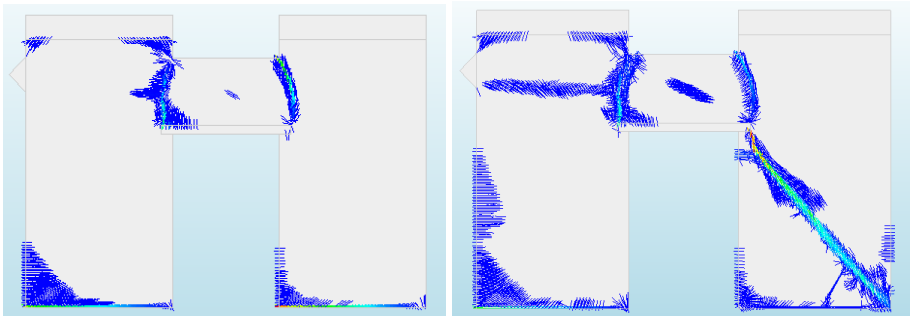

Figure 127 Load application length 44 cm. Damage contour for (a) d=6 mm (b) d=24.6 mm

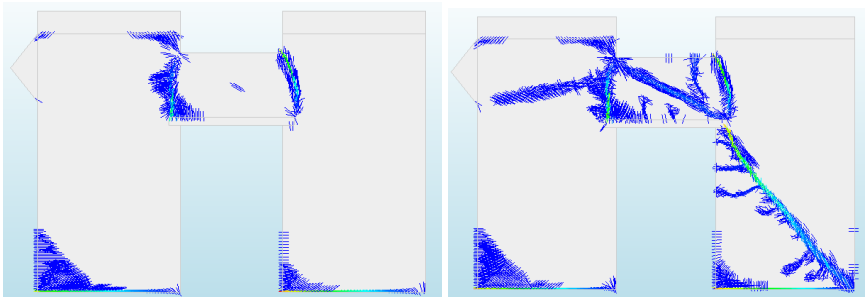

Figure 128. Load application length 88 cm. Damage contour for (a) d=6 mm (b) d=24.6 mm

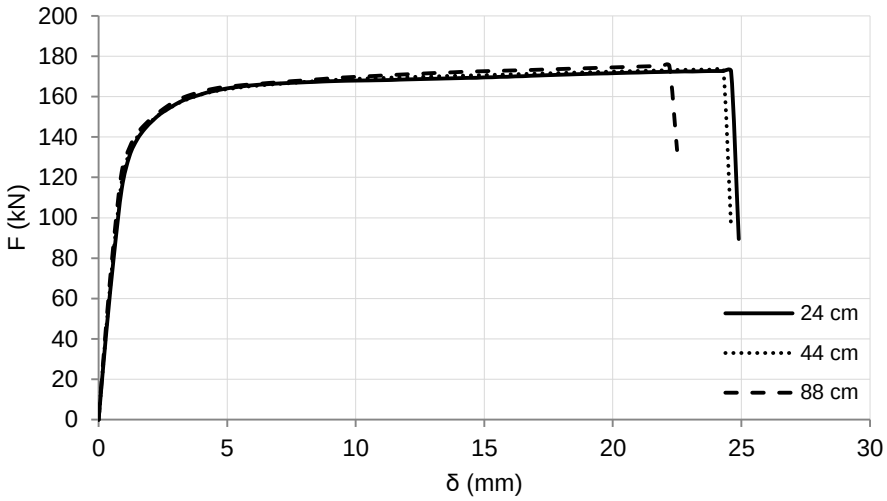

Figure 129. Force-displacement graphs for different values of load application length

5.4 Comparison with a different approach

In order to further validate the reliability of the model to the evaluation of the expected test results, a comparison with the application of the Saloustros et al. (2016) model to the COMET software. The material properties for both approaches were exactly the same with a value of 0.211 MPa for the tensile strength. This value was selected since is giving the most conservative results as it was proved in the previous sections of chapter 5. The comparison in terms of damage pattern is presented in Figure 130. It is observed that both models are giving a similar damage pattern, with the forming of flexural cracks in the end sections of the spandrel panel, as well as the horizontal crack on the left pier. This comparison is showing that the prediction of the expected behavior of the UPC experimental case is validated by other numerical approaches. The forming of the horizontal crack in the left pier is forming in both models, absorbing energy and therefore, not letting the spandrel panel to fail in shear.

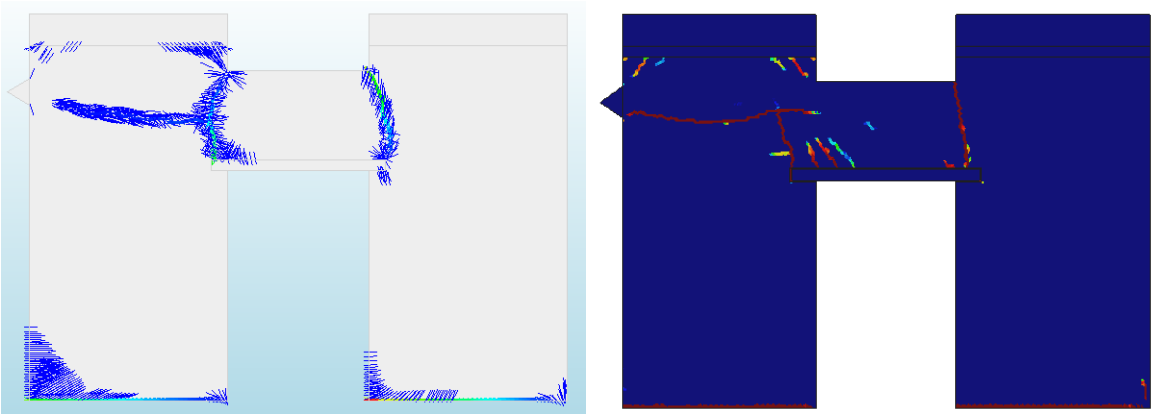

Figure 130. Damage contour for (a) adopted macromodel (b) Saloustros et al. (2016) model

5.5 Conclusions

The macromodel that was created for the purposes of this study proved to be a reliable tool for the assessment and the evaluation of the behavior of masonry facades subjected to in-plane loading. Its application to the ongoing experimental campaign of the Technical University of Catalonia gave a first idea about the expected load capacity and damage pattern. Although it manage to estimate a horizontal capacity of maximum 173 kN, less than the actuator maximum capacity of 250 kN, nevertheless it did not gave a reliable estimation of whether or not the spandrel is going to fail in shear. The shear failure of the spandrel proved to be connected with the propagation of the horizontal crack in the left pier. The crack pattern proved to be influenced by the geometry, the vertical loading and the tensile strength of the masonry. Since the tensile strength of the masonry as a composite material is not easy defined, the safest method for continuing this study would be the use of more analytical techniques or different geometry configurations in order to obtain a numerical model with shear failure of the spandrel. For those studies, the maximum tensile strength, resulted from the diagonal compression tests, is proposed to be used as an input, to get as conservative results as possible.

6. CONCLUSIONS

The present study managed to apply a variety of different methods for the evaluation of the strength of masonry spandrels. Valuable conclusions that were derived from this thesis are the following:

- The state of the art review regarding this topic was valuable to highlight the importance of spandrels in the structural performance of masonry buildings. Also the conclusions from the state of the art leaded to the appropriate selection of the modeling strategy that was followed.
- The macromodelling technique proved to be able to estimate the behavior of existing masonry facades. Some drawbacks of this method could be the obtaining of a diffused crack pattern as well as an underestimation of the maximum strength capacity of 6.8%. Nevertheless it provided a good approximation of the response of portal frames to in plane loads.
- The micromodelling technique that was applied proved to be accurate in terms of damage pattern but not in terms of load-displacement relation. The increased demand for input parameters and its higher computational cost made this approach much more difficult to handle.
- The comparison between the different methods applied showed that the macromodelling technique is the most suitable technique for investigating masonry spandrels and for that reason it was applied to the ongoing experimental campaign of UPC, with satisfying estimations.
- The modelling of the timber lintel as well as its connection with the spandrel is very influential for the nonlinear behavior of masonry spandrels. Therefore it should be executed with great caution.
- Some of the properties of the interface between timber lintel and masonry that the numerical model requires as an input (e.g. stiffness), are difficult to be estimated since it can be influenced by unpredictable factors as the construction process and its quality.

Due to the limitation of time and significant computational effort involved in running each analysis on this numerical model, several areas that need to be addressed by further research have been identified:

- An extensive parametric analysis should be executed in order to identify the different parameters required for the simplified micromodelling approach. Great caution should be given for the interface parameters, since they are a simplification of the joint mortar. Therefore defining a physical meaning for their properties would be a challenging task.

- Further investigation, experimental and numerical, should be performed about the interaction between timber lintel and masonry spandrel, which proved to be very influential for the total response of masonry portal frames.
- The reliability of the existing analytical expressions should be defined with their application on existing experimental campaigns.
- The application of an equivalent frame method for masonry spandrels, using the existing analytical equations as a failure criterion, and its comparison with a Finite Element model would be valuable for further research. With this method the reliability of analytical expressions proposed by codes and bibliography could be defined. Since this method is widely used in engineering practice it would be important to estimate how much the simulation of the spandrel component is affecting the in plane capacity of unreinforced masonry buildings.

7. REFERENCES

(ATC-43 Project), A. T. C. (1998). “FEMA 306, Evaluation of earthquacke damaged concrete and masonry wall buildings.” 1–270.

(CEN), E. C. of S. (1996). “Eurocode 6: Design of masonry structures Part 1-1: General rules for buildings -Reinforced and unreinforced masonry.”

(CEN), E. C. of S. (1998). “Eurocode 8: Design of structures for earthquake resistance-part 1: general rules, seismic actions and rules for buildings.”

Allen, C., Masia, M. J., Page, A. W., Griffith, M. C., and Derakhshan, H. (2016). “Experimental testing of unreinforced masonry walls with openings subject to cyclic in-plane shear.” *Brick and Block Masonry - Trends, Innovations and Challenges*, (68), 1401–1408.

Asprone, D., Cadoni, E., Prota, A., and Manfredi, G. (2009). “Dynamic behavior of a Mediterranean natural stone under tensile loading.” *International Journal of Rock Mechanics and Mining Sciences*, 46, 514–520.

ATC (Applied Technology Council). (1997). “NEHRP guidelines for the seismic rehabilitation of buildings. FEMA 273, Washington, DC.”

Augenti, N. (2000). “Il calcolo sismico degli edifici in muratura (in Italian).” *UTET*, Turin, Italy.

Augenti, N., and Parisi, F. (2010). “Constitutive Models for Tuff Masonry under Uniaxial Compression.” *Journal of Materials in Civil Engineering*, 22(11), 1102–1111.

Augenti, N., and Parisi, F. (2011). “Constitutive modelling of tuff masonry in direct shear.” *Construction and Building Materials*, Elsevier Ltd, 25(4), 1612–1620.

Augenti, N., Parisi, F., Prota, A., and Manfredi, G. (2011). “In-plane lateral response of a full-scale masonry subassemblage with and without an inorganic matrix-grid strengthening system.” *Journal of Composites for Construction*, 15(4), 578–590.

Belmouden, Y., and Lestuzzi, P. (2009). “An equivalent frame model for seismic analysis of masonry and reinforced concrete buildings.” *Construction and Building Materials*, Elsevier Ltd, 23(1), 40–53.

Benedetti, D., and Magenes, G. (2001). “Correlazione tra tipo di danno ed energia dissipata negli edifici in muratura.” *Ingegneria Sismica*, 53–62.

Beyer, K. (2012). “Peak and residual strengths of brick masonry spandrels.” *Engineering Structures*, Elsevier Ltd, 41, 533–547.

Beyer, K., and Dazio, A. (2012). “Quasi-static cyclic tests on masonry spandrels.” *Earthquake Spectra*, 28(3), 907–929.

Beyer, K., and Mangalathu, S. (2014). “Numerical Study on the Peak Strength of Masonry Spandrels

with Arches." *Journal of Earthquake Engineering*, 18(January 2014), 169–186.

Calderini, C., Cattari, S., and Lagomarsino, S. (2009). "In-plane strength of unreinforced masonry piers." *Earthquake Engineering and Structural Dynamics*, 38, 243–267.

Cattari, S., and Lagomarsino, S. (2008). "A Strength Criterion for the Flexural Behaviour of Spandrels in Un-reinforced Masonry Walls." *The 14 World Conference on Earthquake Engineering*, Beijing, China, 1–8.

CEB-FIP. (1993). "Model Code 1990." *Comité Euro-International du Béton*.

Cervera, M., Oliver, J., and Faria, R. (1995). "Seismic evaluation of concrete dams via continuum damage models." *Earthquake Engineering and Structural Dynamics*.

Cervera, M., Pelà, L., Clemente, R., and Roca, P. (2010). "A crack-tracking technique for localized damage in quasi-brittle materials." *Engineering Fracture Mechanics*, 77(13), 2431–2450.

Clemente, R. (2006). "Structural analysis of historical buildings by localized cracking models (in Spanish)." PhD dissertation Universitat Politècnica de Catalunya, Barcelona, Spain.

Clemente, R., Roca, P., and Cervera, M. (2006). "Damage model with crack localization-application to historical buildings." *Structural Analysis of Historical Constructions*, New Delhi, 1125–1135.

CUR. (1994). "Structural masonry: an experimental/numerical basis for practical design rules (in Dutch). Report 171, CUR, Gouda, The Netherlands."

D'Ayala, D. F., and Paganoni, S. (2010). "Assessment and analysis of damage in L'Aquila historic city centre after 6th April 2009." *Bulletin of Earthquake Engineering*, 9(1), 81–104.

DIANA FEA. (2016). *DIANA FEA- User 's Manual release 10.1*. (J. Manie, ed.), Delftechpark 19a, 2628 XJ Delft, The Netherlands.

Gattesco, N., Clemente, I., Macorini, L., and Noè, S. (2008). "Experimental investigation on the behavior of spandrels in ancient masonry buildings." *The 14 World Conference on Earthquake Engineering*.

Graziotti, F., Magenes, G., Penna, A., and Fontana, D. (2011). "Experimental cyclic behaviour of stone masonry spandrels." *15th World Conference on Earthquake Engineering*, Lisboa, 1–10.

Graziotti, F., Penna, A., and Magenes, G. (2014). "Influence of timber lintels on the cyclic behaviour of stone masonry spandrels." *9th International Masonry Conference 2014 in Guimarães*, Guimarães, 1–12.

Italian Ministry of Infrastructure and Transport. (2008). "NTC 2008 - Italian Building Code. D.M. 14/01/2008." 428.

Kappos, A. J., Penelis, G. G., and Dracopoulos, C. G. (2002). "Evaluation simplified models for lateral load analysis of unreinforced masonry buildings." *Journal of Structural Engineering, ASCE*, 1(1),

890–897.

Knox, C. (2012). “Assessment of Perforated Unreinforced Masonry Walls Responding In-Plane.” PhD Thesis. The University of Auckland.

Lofti, H., and Shing, P. (1994). “Interface model applied to fracture of masonry structures.” *Journal of Structural Engineering*, 120(1), 63–80.

Lourenço, P. B. (1994). “Analysis of Masonry Structures With Interface Elements. Theory and Applications.” *TNO Building and Construction Research - Computational Mechanicas*, (3), 34.

Lourenço, P. B. (1996). “Computational strategies for masonry structures.” PhD Thesis, Delft University of Technology.

Lourenço, P. B. (1997). *An anisotropic plasticity model for quasi-brittle composite shells*. *Computational Plasticity: Fundamentals and Applications*, (Pinteridge Press, ed.), London, UK.

Lourenço, P. B. (2002). “Computations on historic masonry structures.” *Progress in Structural Engineering and Materials*, 4(3), 301–319.

Lourenço, P. B. (2008). “Recent advances in masonry modelling: Micromodelling and Homogenisation.” *Multiscale Model. Solid Mech. Comput. Approaches 3*, 20, 251–294.

Lourenço, P. B., and Rots, J. (1997). “Multisurface Interface Model for Analysis of Masonry Structures Article.” *Journal of Engineering Mechanics*, 230–238(123), 1–23.

Magenes, G., and Calvi, G. M. (1997). “In-plane seismic response of brick masonry walls.” *Earthquake engineering and structural Dynamics*, 26(November), 1091–1112.

Magenes, G., and Fontana, D. (1998). “Simplified non-linear seismic analysis of masonry buildings.” *Fifth International Masonry Conference*, London, England.

NIKER Project. (2010). “D3.1: Inventory of earthquake-induced failure mechanisms related to construction types, structural elements, and materials.” 56.

NZSEE. (2006). *Assessment and improvement of the structural performance of buildings in earthquake. Recommendations of a NZSEE Study Group, New Zealand Society for Earthquake Engineering (Including Corrigendum N. 1, 2, 3 and 4)*. *Earthquake*.

Papa, E. (1997). “Unilateral damage model for masonry based on a homogenization procedure.” *Mechanics of Cohesive-frictional Materials*, 1, 349–366.

Parisi, F., Iovinella, I., Balsamo, A., Augenti, N., and Prota, A. (2013). “In-plane behaviour of tuff masonry strengthened with inorganic matrix-grid composites.” *Composites Part B: Engineering*, Elsevier Ltd, 45(1), 1657–1666.

Parisi, F., Lignola, G. P., Augenti, N., Prota, A., and Manfredi, G. (2011). “Nonlinear Behavior of a Masonry Subassemblage Before and After Strengthening with Inorganic Matrix-Grid

Composites.” *Journal of Composites for Construction*, 15(5), 821–832.

Pasticier, L., Amadio, C., and Fragiacomo, M. (2007). “Non-linear seismic analysis and vulnerability evaluation of a masonry building by means of the SAP2000V.10 code.” *Earthquake Engineering and Structural Dynamics*, 37, 467–485.

Pelà, L., Cervera, M., and Roca, P. (2011). “Continuum damage model for orthotropic materials: Application to masonry.” *Computetional Methods in Applied Mechanics and Engineering*, 200(9–12), 917–930.

Pelà, L., Cervera, M., and Roca, P. (2013). “An orthotropic damage model for the analysis of masonry structures.” *Construction and Building Materials*, 41, 957–967.

Roca, P., Cervera, M., Gariup, G., and Pela, L. (2010). “Structural Analysis of Masonry Historical Constructions . Classical and Advanced Approaches.” *Archives of Computational Methods in Engineering*, 17, 299–325.

Rots, J., and Lourenço, P. B. (1993). “Fracture simulations of masonry using non-linear interface elements.” *Proceedings of the 6th North American masonry conference*, Philadelphia, USA.

Sabatino, R., and Rizzano, G. (2010). “Non linear static analysis of masonry structures Simplified equivalent frames and accurate models.” *14th European Conference on Earthquake Engineering*, Ohrid.

Saloustros, S., Pelà, L., Cervera, M., and Roca, P. (2016). “Finite element modelling of internal and multiple localized cracks.” *Computational Mechanics*, Springer Berlin Heidelberg, 59(2), 299–316.

Salvatoni, P., and Ugolini, M. (2016). “Comportamento di elementi in muratura fino a collasso : prove sperimentali e modellazione numerica.” MSc Thesis, Politecnico di Milano.

Structures, E., Universit, R. S., Chieti, A., Universit, E. S., Chieti, A., Roca, P., Polit, U., Pela, L., Polit, U., Knowledge, N. I., and View, R. (2017). “Analysis of the performance in the linear field of Equivalent-Frame Models for Regular and Irregular Masonry Walls.” (May).

Sutcliffe, D. J., Yu, H. S., and Page, A. W. (2001). “Lower bound limit analysis of unreinforced masonry shear walls.” *Computers & Structures*, 79(14), 1295–1312.

Tomaževič, M. (1999). *Earthquake-Resistant Design of Masonry Buildings*.

Turnšek, V., and Čačovič, F. (1971). “Some experimental results on the strength of brick masonry walls.” *Proceedings of the 2nd International Brick Masonry Conference*.

Yi, T., Moon, F. L., Leon, R. T., and Kahn, L. F. (2006). “Analyses of a Two-Story Unreinforced Masonry Building.” *Journal of Structural Engineering*, 132(5), 653–662.

Zucchini, A., and Lourenço, P. B. (2002). “A micro-mechanical model for the homogenisation of masonry.” *International Journal of Solids and Structures*, 39(12), 3233–3255.